Development of Method for A-Scan Ultrasound Localization of Solid, Nonpalpable Breast Lesions

By
Karolina Palac and Rachel Rowey
Sc.B., Brown University, 2024

Thesis
Submitted in partial fulfillment of the requirements for the Degree of Master of Science in Biomedical Engineering at Brown University

Providence, Rhode Island
May 2024

AUTHORIZATION TO LEND AND REPRODUCE THE THESIS

As the sole authors of this thesis, we authorize Brown University to lend it to other institutions or individuals for the purpose of scholarly research.

Karolina Palac

Date: 5/1/25 _____

Karolina Palac

Date: 5/1/25 _____

Rachel Rowey

We further authorize Brown University to reproduce this thesis by photocopying or other means, in total or in part, at the request of other institutions or individuals for the purpose of scholarly research.

Karolina Palac

Date: 5/1/25 _____

Karolina Palac

Date: 5/1/25 _____

Rachel Rowey

This thesis by Karolina Palac and Rachel Rowey is accepted in its present form by the Center of Biomedical Engineering as satisfying the thesis requirement for the degree of Master of Science.

Dr. Vikas Srivastava, Advisor

Date_____

Recommended to the Graduate Council

Dr. Marissa Gray, Reader

Date_____

Dr. Joseph Crisco, Reader

Date_____

Approved by the Graduate Council

Dr. Marissa Gray, Biomedical Engineering Master's Program Director

Date_____

Acknowledgements

We would first and foremost like to thank our advisor and mentor, Dr. Vikas Srivastava, for his encouragement and guidance over the last four years and throughout this research. Our sincere appreciation goes out to our advisor, Dr. Marissa Gray, for her endless support and advice throughout the course of this project. We also thank Dr. Joseph Crisco for being a valuable member of our thesis committee. Special thanks to Francesca Denise Abulencia and Dr. Sijun Niu for laying the groundwork for this project, as well as the rest of the Srivastava Lab. Finally, our deepest gratitude goes out to our friends and family for their unwavering support.

Table of Contents

Acknowledgements ..... **iv**

List of Figures ..... **vii**

List of Tables ..... **ix**

Abstract **1**

I. Clinical Need **2**

Breast Cancer Background & Classification 2

Current Localization Methods 3

Current Imaging Techniques 7

Physical Principles of Ultrasound Wave Propagation 10

Need Statement 11

II. Project Objectives **13**

III. Design Process and Methods **14**

Model Development 14

Data Preprocessing 18

Developing the Method 19

Assessing the Method 20

IV. Results and Discussion **22**

Dip-Based Estimation 23

Peak-Based Estimation 27

Comparison of Approaches 31

Limitations 36

V. Conclusions **38**

VI. Anticipated Regulatory Pathway **40**

VII. Reimbursement **42**

VIII. Potential Market and Impact **45**

Market Landscape 45

Market Segmentation..... 47
IX. Future Directions..... 51
References..... 54
Appendix A: Parameters for Depth Calculation from Signal..... 60
Appendix B: Abaqus Code..... 62
Appendix C: Depth Estimation Code..... 75
Appendix D: Abaqus Model..... 81
Appendix E: Processed Signals..... 84
Appendix F: Method Comparison Data..... 97
Appendix G: Sample Calculations..... 100
Appendix H: Depth Estimation Error..... 102

List of Figures

Figure 1. Schematic of needle/wire localization method.....3
Figure 2. Diagrams and dimensions of implantable devices..... 5
Figure 3. Mammograms illustrating varying breast tissue densities.....8
Figure 4. MRI scan of the breasts showing high-resolution cross-sectional imaging..... 9
Figure 5. Ultrasound image where a circular breast lesion is visible..... 9
Figure 6. Visualization of breast-tumor assembly meshing.....16
Figure 7. Diagram of simulated ultrasound wave propagation.....17
Figure 8. Raw ultrasound signal collected for the 0 cm tumor offset case..... 18
Figure 9. Preprocessed and normalized ultrasound signal.....19
Figure 10. Schematic illustration of tumor depth calculations used for error analysis.....21
Figure 11. Detected peaks overlaid on the normalized and truncated ultrasound signal.....23
Figure 12. Dip-based absolute error as a function of offset from the center..... 32
Figure 13. Peak-based absolute error as a function of offset from the center.....33
Figure 14. Dip-based method percent error averages..... 34
Figure 15. Peak-based percent error averages..... 34
Figure 16. Reimbursement scheme for ultrasound-guided breast lumpectomy.....42
Figure 17. A market landscape for existing solutions.....47
Figure 18. Percentage of breast cancer cases by stage across varying demographics..... 48
Figure 19. Overall cancer market segmentation for target population identification..... 49
Figure D1. Example Abaqus Model images with tumors were kept at center of the breast.....81
Figure D2. Example Abaqus Model images with tumor diameter was kept constant at 1 cm..... 82
Figure D3. Abaqus sound wave simulation moving down..... 83
Figure D4. Abaqus sound wave simulation reflecting up through breast-tumor system.....84
Figure E1. Non-processed signal for 10 mm tumor at center..... 84
Figure E2. Example of processed signal for 10 mm tumor at center.....84
Figure E3. Dip identification for 10 mm tumor 0 offset..... 85
Figure E4. Peak identification for 10 mm tumor at center.....85
Figure E5. Dip identification for 7.5 mm tumor at center..... 86
Figure E6. Peak identification for 7.5 mm tumor at center.....86
Figure E7. Dip identification for 6 mm tumor at center..... 87
Figure E8. Peak identification for 6 mm tumor at center.....87

Figure E9. Dip identification for 5 mm tumor at center..... 87
Figure E10. Peak identification for 5 mm tumor at center.....88
Figure E11. Dip identification for 7.5 mm tumor -5 mm offset..... 89
Figure E12. Peak identification for 7.5 mm tumor -5 mm offset..... 89
Figure E13. Dip identification for 10 mm tumor +2.5 mm offset..... 90
Figure E14. Peak identification for 10 mm tumor +2.5 mm offset.....90
Figure E15. Dip identification for 5 mm tumor +5 mm offset..... 91
Figure E16. Peak identification for 5 mm tumor +5 mm offset.....91
Figure E17. Dip identification for 5 mm tumor -12.5 mm offset..... 91
Figure E18. Peak identification for 5 mm tumor -12.5 mm offset..... 92
Figure E19. Dip identification for 6 mm tumor +5 mm offset..... 92
Figure E20. Peak identification for 6 mm tumor +5 mm offset.....93
Figure E21. Processed signals overlaid for 10 mm tumor moving up.....93
Figure E22. Processed signals overlaid for 10 mm tumor moving up.....93
Figure E23. Processed signals overlaid for 10 mm tumor moving down.....94
Figure E24. Processed signals overlaid for 7.5 mm tumor moving up.....95
Figure E25. Processed signals overlaid for 7.5 mm tumor moving down.....95
Figure E26. Processed signals overlaid for 6 mm tumor moving up.....95
Figure E27. Processed signals overlaid for 6 mm tumor moving down.....96
Figure E28. Processed signals overlaid for 5 mm tumor moving up.....96
Figure E29. Processed signals overlaid for 5 mm tumor moving up.....97
Figure H1. Peak-based percent error as a function of offset.....102
Figure H2. Dip-based percent error as a function of offset..... 103
Figure H3.Dip-based method absolute error averages.....103
Figure H4. Peak-based absolute error average..... 103

List of Tables

Table 1. Benefits and drawbacks of each localization method..... 6
Table 2. Dip-based estimation results for 10 mm diameter tumor at various offsets..... 23
Table 3. Dip-based estimation results for 7.5 mm diameter tumor at various offsets..... 24
Table 4. Dip-based estimation results for 6 mm diameter tumor at various offsets..... 25
Table 5. Dip-based estimation results for 5 mm diameter tumor at various offsets..... 26
Table 6. Peak-based estimation results for 10 mm diameter tumor at various offsets.....28
Table 7. Peak-based estimation results for 7.5 mm diameter tumor at various offsets.....28
Table 8. Peak-based estimation results for 6 mm diameter tumor at various offsets.....29
Table 9: Peak-based estimation results for 5 mm diameter tumor at various offsets from center. 30
Table 10. Average error comparison for dip and peak-based methods.....35
Table 11. Table comparing regulatory pathways of proposed solution and predicate devices..... 41
Table 12. Relevant ICD-10-CM diagnosis codes and clinical descriptions.....43
Table A1. Parameters for 10 mm tumor signal analysis..... 60
Table A2. Parameters for 7.5 mm tumor signal analysis..... 60
Table A3. Parameters for 6 mm tumor signal analysis..... 61
Table A4. Parameters for 5 mm tumor signal analysis..... 61
Table F1. Average percent error of both dip and peak based estimation methods..... 98
Table F2. Average percent error of dip-based estimation methode..... 98
Table F3. Average percent error of peak-based estimation method.....99

Abstract

Breast cancer is one of the most prevalent forms of cancer in the U.S. and incidence rates continue to rise. With increased access to routine imaging and screening, the detection of nonpalpable breast lesions, which cannot be detected through physical examination, has become increasingly common. Accurate localization of non-palpable lesions is critical for ensuring complete surgical excision, preventing metastasis, and reducing the need for reoperation. There are several existing localization techniques including wire localization, radioactive seeds, magnetic seeds, and intraoperative ultrasounds. Although these methods are able to guide surgeons in excising abnormal tissue, they have several limitations. These include invasiveness, interference with surgical equipment, high costs, and, in the case of radioactive seeds, radiation exposure. Furthermore, many of these techniques offer limited real-time feedback and insufficient depth resolution, particularly for deep-seated or small lesions. These limitations highlight the need for a more effective, non-invasive, and precise localization strategy.

To address these challenges, we propose a novel method for improving the depth localization of nonpalpable breast lesions using A-scan ultrasound data. Specifically, we present a computational framework using finite element analysis (FEA) to model ultrasound wave propagation through breast tissue containing embedded tumors at varying depths and of varying sizes. This approach provides a non-invasive, patient-specific, and physics-informed strategy with the potential of enhancing and improving the ease of intraoperative procedures. Furthermore, in simulating how ultrasound signals change in response to tumor location, the approach demonstrates the feasibility of receiving and interpreting ultrasound data in real time to provide information on lesion presence, depth, and location.

I. Clinical Need

Breast Cancer Background & Classification

Currently, breast cancer is the second most prevalent form of cancer in women in the United States, making up about 1 in 3 new female cancers each year. The average risk of a woman developing breast cancer during her lifetime is about 13%, or a 1 in 8 chance, and this incidence rate has increased by 0.5% per year in recent years[1]. This highlights the importance of ongoing breast cancer research and novel treatments.

Histology & Classification. There are several different forms of breast cancers, originating in different areas of the breast and affecting various types of cells. A majority of breast cancers, referred to as carcinomas, originate in the epithelial cells that line the ducts, which are canals that carry breast milk to the nipple, and lobules, which are glands that make breast milk. A less common form of breast cancer, called sarcomas, arise in the connective tissue, such as myofibroblasts, or the blood, such as blood vessel cells. The most common type of breast cancer is ductal cancer, also referred to as adenocarcinoma.[2] Breast cancer can also be classified as in situ or invasive. In situ refers to a case in which the cancer is confined to the ducts or lobules and has not invaded surrounding tissues, while invasive refers to a case in which the cancer has spread.

Stages. In addition to type, cancers are also classified into stages upon diagnosis. Stage 0 is the earliest phase where the cancer is localized to the area in which it started. This stage is easily treatable and is generally considered precancerous. Next, Stage I is localized to a small area and has not yet spread to lymph nodes or other tissues. Stage II means that the cancer mass has grown, but remains localized. Stage III has more growth and has possibly spread to lymph nodes or other tissues. Finally, Stage IV is when the cancer has spread to other organs or areas of the body, also called metastatic cancer.[3]

To remove the identified cancerous breast masses, a biopsy can be performed where the abnormal tissue is localized and characterized, and then surgically removed through procedures like a lumpectomy. If caught before the cancer spreads and metastasizes, this pipeline is effective in entirely eliminating the cancerous threat. However, these procedures become more challenging when the breast mass is nonpalpable. Nonpalpable breast mass cannot be found during clinical, physical examinations, but can be identified by ultrasound, mammography, and MRI. Typically, nonpalpable breast masses are present during stage I and

II, when the mass is still relatively small. In 20-30% of patients with nonpalpable breast masses, breast nodules develop into cancer.[4] This highlights the need for effective methods for the successful localization and removal of nonpalpable breast lesions.

Current Localization Methods

The first localization method currently in use for nonpalpable breast lesions is wire, or needle, localization, where a needle is inserted into the breast precisely at the location of the tumor to mark its location. First, an imaging technique is used to visually locate the mass. The breast is sterilized with an antiseptic solution and a local anesthetic is sometimes injected to numb the skin before needle placement. A thin, hollow needle is inserted into the breast down to the lesion and another image is taken to ensure correct placement. This is repeated as many times as necessary. Then, the needle is taken out, leaving a thread-like wire behind marking the location, as seen in Figure 1. The needle is then taped in place to prevent any shifting in the hours before operation. At the time of operation, the wire guides the surgeon to the area of concern in the breast, allowing for accurate removal of tissue.[5] While cost-effective and simple to administer, wire localization requires same-day placement, leading to limited scheduling flexibility. It also involves an external component that can shift or fracture, causing patient discomfort and potential localization inaccuracies.

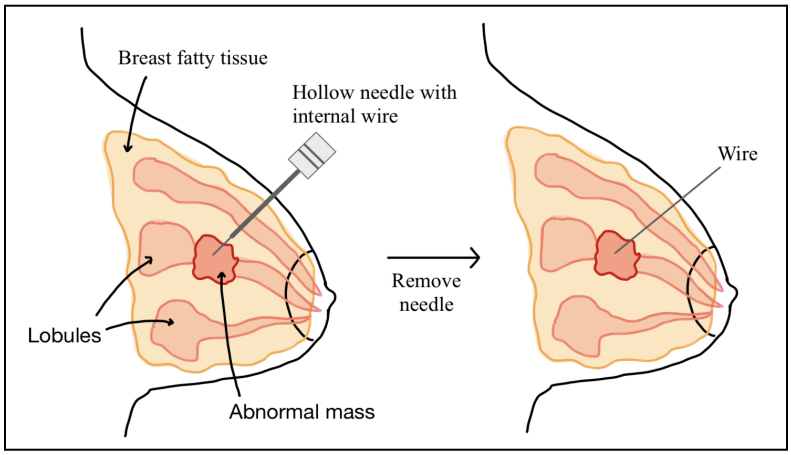

Figure 1*. Schematic of needle/wire localization method.*

Another localization technique is the SAVI SCOUT, a radar localization technology, as seen in Figure 2a. This technique uses a metallic reflector, which is about the size of a

grain of rice, that is placed in the breast up to 30 days before surgery.[6] During the procedure, the breast is positioned either in the mammography machine or under the ultrasound. The skin of the breast is sterilized and a numbing medication is injected into the site of concern. A radiologist then uses images on the ultrasound monitor or mammogram to guide a 16-gauge needle to the area. Once the placement is confirmed, the SAVI SCOUT reflector is placed through the needle. The needle is then removed from the breast tissue, leaving the reflector in place at the lesion. A detector unit that emits radar waves is used to ensure correct placement.[7] The reflector is a nonradioactive IR-activated electromagnetic wave reflector. It has two antennae, an IR light receptor, and a transistor switch, making it a total of 12 mm long. Therefore, during the actual operation, a sterile detector handpiece that emits IR light is used to locate the reflector. The surgery dissection is directed by continuous audible feedback from the console, until ultimately the reflector is removed along with the abnormal breast tissue.[8] Although the method does not require an external component, there are high associated setup and equipment costs, incompatibility with MRI, and limited supporting clinical data.

Another technique for non-palpable lesion localization is the radioactive seed, as seen in Figure 2b. The procedure for placing the radioactive seed is identical to that of the SAVI SCOUT. The placement of the needle is guided by mammogram or ultrasound and the seed is then placed through the needle.[9] At the time of operation, the radioactive seed is located and removed, along with the surrounding tissue, using an intraoperative gamma radiation detector, such as a gamma probe. Once removed, the seed is deposited in a lead box and sent to the radiology sector, where it can be stored for decay. Additionally, the radioactive seed is able to be placed up to 60 days prior to the removal surgery. The seed has a core that contains iodine-125 and a radiological marker, which can be gold, silver, ceramic, resin, etc. The seed also has a capsule of biocompatible material that surrounds the core, which is usually titanium or stainless steel. The seed is roughly 4.5 mm long and 0.8 mm wide.[10] However, this approach involves radiation exposure for both patients and healthcare staff, presenting safety concerns. It also has relatively high re-excision rates and is not ideal for patients who are unable to avoid close contact with others for extended periods while implanted.

The last current localization technology that utilizes an implantable device is the Mag Seed, or magnetic seed, as seen in Figure 2c. This seed is composed entirely of surgical grade

stainless steel and is 5 mm long by 1 mm wide in a cylindrical formulation. The seed can be placed up to 30 days before the biopsy procedure. Once again, the implantation procedure is almost identical to that of the SAVI SCOUT and radioactive seeds. Mammography or ultrasound is used to guide the placement of the needle, through which the Mag Seed is placed. On the day of operation, the surgeon uses a handheld magnetic probe to locate the Magseed and remove it along with the abnormal tissue.[11] Specifically, the probe emits magnetic waves and can sense changes in the magnetic moment caused by metal materials.[12] Despite providing live localization feedback, magnetic seed systems are expensive and incompatible with standard surgical instruments due to magnetic interference. Additionally, they are not MRI-compatible, limiting their utility for patients undergoing multimodal imaging.

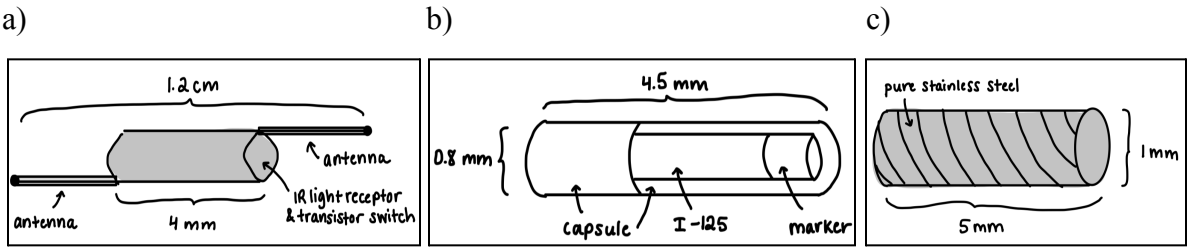

Figure 2. *Diagrams and dimensions of implantable devices, including a) SAVI SCOUT, b) radioactive seed, and c) Mag Seed.*

Finally, another approach to non palpable lesion localization is the intraoperative ultrasound (IOUS). Notably, this technique does not require any device or seed to be implanted before surgery. Instead, it solely uses live ultrasound imaging to guide the surgeon to the tumor. The location of the tumor is observed by the ultrasound before the operation begins and a sterile skin marker is used to mark the excision borders. The ultrasound is able to visualize the distance from the tumor to the muscular layer as well as the depth from the skin. The tissue is resected perpendicularly to the chest wall in a cylindrical manner. The ultrasound is used again to ensure that the excision included all margins and that no cancerous or suspicious tissue is left in the breast.[13] However, IOUS can be slow to implement due to required training and learning curves among surgical teams.

Table 1. *Benefits and drawbacks of each localization method.*

Method	Cost	Ease of Use	Patient Comfort	Re-excision Rate	Other
Wire Localization	-Costs $775 for patient without anesthesia [16] - Costs $1260 for patient with anesthesia[14] -Uses minimal, inexpensive materials such as nitinol and stainless steel (actual device costs $20)	- No learning curve for surgeon -Simple procedure -Well-established	- Has external component - Uncomfortable and may shift or fracture -Must be placed the day of surgery, limited scheduling -Procedure takes 20-30 mins	-Varies with each study, but overall 14-24% [15, 16]	-No depth limitations -Compatible with mammogram, ultrasound, and MRI guidance
Non-radioactive radar localization (SAVI SCOUT)	- Opening room setup fees are $3000 and procedure fees are $68 per hour - Actual device costs $450 to manufacture - Expensive	- Relatively simple procedure - No radiation exposure - No repositioning once deployed	- No external component - Place 30 days ahead of time, scheduling flexibility - Takes approximately 30 mins	13.7%[17]	- High nickel content (allergy concern) - Depth limitation: 60 mm detection range[18] - Not MRI compatible - Limited published data
Radioactive Seed	- Device costs $20-50 to manufacture - Patient costs range from $148-311 [20]	- Relatively simple procedure - Radiation exposure for surgeon and staff - No repositioning once deployed	- No external component, more comfortable - Can't hold young children or animals for long periods of time while implanted - Place 60 days ahead of time, scheduling flexibility - Procedure takes approximately 30 mins	23%[16]	- No depth limitations - Compatible with sentinel lymph node mapping - Has extra complication of radiation safety precautions - Incompatible with MRI - Compatible with ultrasound and mammogram
Magnetic Seed	- Device costs $400 to manufacture - On average, costs $297 for patients - Expensive	- Can't use the usual metal instruments - No radiation exposure - Live count indicates distance to seed	- No external component, comfortable - Place 30 days ahead of time, scheduling flexibility - Takes approximately 30 mins	12.4%[18]	- Stainless steel, minimal allergy concerns - No MRI compatible needle delivery system - Minimal published data - MRI bloom may be up to 4 cm - Depth limitation of 30 mm
IOUS	- Compared to other solutions, $0 since all require an ultrasound - Ultrasounds on average cost $163 for patients	- Slow implementation due to learning curves - Requires extra training	- Requires no surgical device placement before operation, one less surgery for patient - Noninvasive - No discomfort	11.1%[16]	- Doesn't require pre and post imaging, all in real-time - One appointment - No depth limitations

Current Imaging Techniques

Breast cancer screening is recommended for women 40-74 years old who are at average risk for breast cancer. The purpose is to check the breasts for cancer before any signs or symptoms so as to detect the cancer as early as possible and improve outcomes. The five-year survival rate for early stage breast cancer is 99% compared to 28% for late stage breast cancer.[19] Imaging plays a critical role in the early detection, diagnosis, and localization of breast tumors, particularly non-palpable lesions that cannot be felt during a physical exam. Common imaging methods for breast cancer screening include mammogram, magnetic resonance imaging (MRI), and ultrasound. Although these methods each have their own drawbacks, the utilization of imaging techniques is promising for the improvement of localization techniques as they could allow for real-time visualization, more precise targeting of non-palpable lesions, and reduced dependence on invasive or preoperative procedures.

Mammogram

Mammograms are X-ray images of the breast taken from various angles. This method is one of the best ways to detect cancer early and commonly finds non-palpable lesions, which are challenging to detect based on their small size and inability to be felt. During a mammogram, a radiologist examines the images to assess abnormalities, such as calcifications or masses, and determines whether further diagnostic procedures, such as a biopsy, are needed to confirm malignancy.[20] Mammograms typically work well for non-dense breast tissue, but have limitations in dense breast tissue. Both fibroglandular tissue and tumors appear white on X-ray images, making differentiation difficult.[20] This can lead to false negatives, where a tumor goes undetected, delaying diagnosis and treatment. Additionally, mammograms involve ionizing radiation exposure, which, while minimal, may not be suitable for pregnant patients or those requiring frequent imaging. In high-risk individuals, such as those with BRCA1/2 mutations, alternative or supplementary imaging methods like MRI or ultrasound are often recommended.

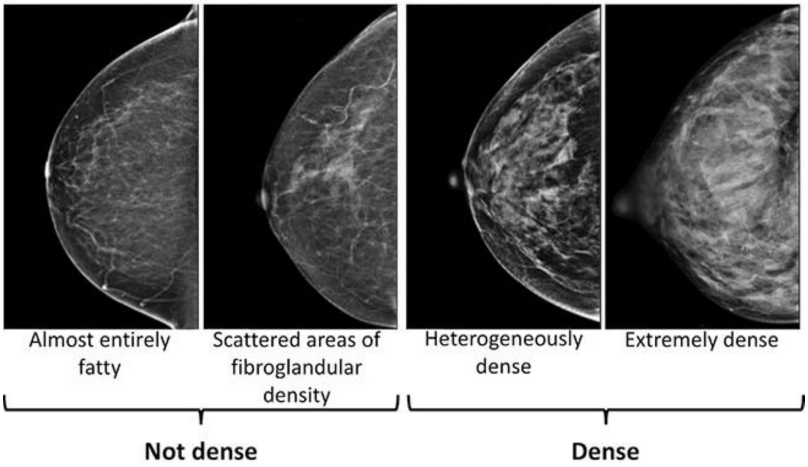

Figure 3. *Mammograms illustrating varying breast tissue densities, ranging from almost entirely fatty to extremely dense. Dense tissue can obscure tumors, which also appear white, increasing the risk of false negatives.*[20]

MRI

MRI for breast cancer screening is typically recommended for women at high risk of breast cancer, often in conjunction with mammograms. Unlike mammograms, MRI does not rely on ionizing radiation but instead uses strong magnetic fields and radio waves to generate detailed images of breast tissue. This method can detect some cancers that mammograms miss, particularly in dense breast tissue. However, MRIs also have a high rate of false positives, leading to unnecessary tests and biopsies being conducted, and also are unable to provide live visualization feedback.[21]

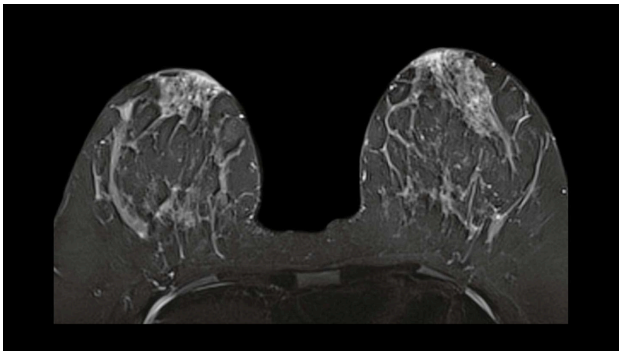

Figure 4*. MRI scan of the breasts showing high-resolution cross-sectional imaging used to detect abnormalities in dense tissue.*[22]

Ultrasounds

A breast cancer screening ultrasound, also known as a sonogram, uses high-frequency sound waves to create images of breast tissue. This technique is commonly used as a supplementary tool when mammograms are inconclusive, especially for patients with dense breast tissue. The most commonly used type of ultrasound for breast imaging is the B-mode, or brightness mode, ultrasound, which uses a transducer to send sound waves into the breast tissue and convert the reflected signals into a two-dimensional grayscale image.[23,24]

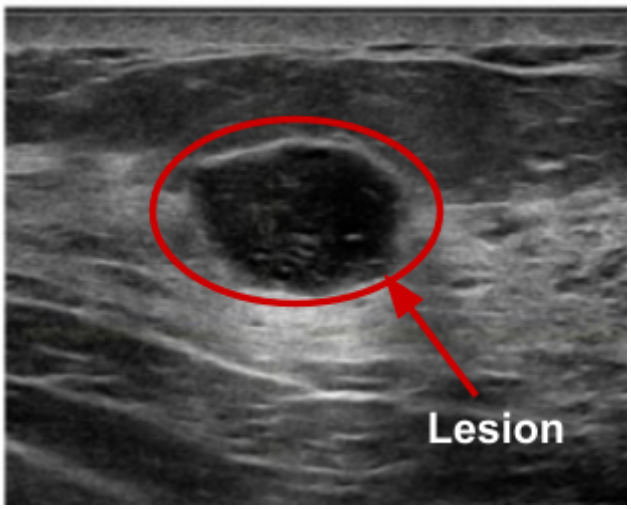

Figure 5*. Ultrasound image where a circular breast lesion is visible, taken in B-mode.*[25]

Ultrasounds are also valuable in intraoperative procedures, aiding in real-time localization of tumors and guiding surgical excisions. We sought to leverage this intraoperative application of ultrasound to further enhance current localization techniques. However, ultrasound images are often prone to speckle noise and artifacts, which can reduce image clarity and affect diagnostic accuracy. Additionally, access to large, high-quality ultrasound datasets is limited due to data scarcity and HIPAA regulations. To overcome these challenges, we aimed to utilize A-mode, or amplitude mode, ultrasound, which provides one-dimensional depth information by measuring the intensity of reflected sound waves at different tissue boundaries. A-mode ultrasound is commonly used in ophthalmology and structural fracture detection but has not been widely explored for breast tumor localization.[53] By employing A-mode ultrasound, we aim to develop a more precise and non-invasive depth estimation method that calculates tumor location based on the speed of sound through

different tissue types. This method could offer a simplified yet effective approach for localizing non-palpable breast lesions, improving accuracy, and reducing reliance on more invasive and costly localization techniques.

A-Mode Peaks

If two materials in a medium have different stiffness properties, the resulting change in wave propagation speed will cause the wave to deviate from its original path, known as refraction. This phenomena lays the foundation for the proposed depth estimation method, since tumors have stiffer material properties than surrounding breast tissue. The height, or amplitude, of each peak of an A-scan ultrasound signal is related to the strength of the reflected signal, meaning larger peaks correspond to larger acoustic mismatches.[26] The position of each peak along the x-axis, indicating depth, represents the time-of-flight, which, when multiplied by the speed of sound in the tissue, would provide the physical depth of the identified interface.[27]

The oscillating nature of the ultrasound signal is characterized by alternating positive and negative peaks, primarily due to acoustic reflections at tissue boundaries with differing acoustic impedances. As the ultrasound wave propagates through the breast tissue, it encounters various interfaces such as fat and tumor boundaries. At each of these interfaces, part of the wave is reflected and part is transmitted, depending on the relative impedance of the two media. The polarity of each reflected peak provides insight into the direction of the impedance mismatch: a positive peak occurs when the wave reflects from a lower-to-higher impedance boundary, while a negative peak appears when the wave reflects from a higher-to-lower impedance boundary. These alternating impedance transitions result in the up-and-down oscillations seen in the A-mode signal.[28]

Physical Principles of Ultrasound Wave Propagation

Ultrasound waves are longitudinal mechanical waves that travel through tissue via compression and rarefaction. Unlike transverse waves, which oscillate perpendicular to their direction of propagation, ultrasound waves move parallel to the direction of energy transfer. The propagation of these waves is governed by the elastic wave equation, which can be derived from the balance of linear momentum equation:

$$\frac{\delta \sigma_{ij}}{\delta x_j} + b_i = \rho u_i$$

where σ_{ij} is the stress tensor, b is the body force, and ρ is the material density.

The speed of ultrasound waves in a medium is determined by the material's density (ρ) and Bulk Modulus (K) and is given by the equation:

$$c = \sqrt{\frac{K}{\rho}}$$

For breast fatty tissue, the speed of sound is usually 1450 +/- 27 m/s.[29] In contrast, for benign and malignant solid breast tumors, the speed of sounds are typically higher around 1513 +/- 27 m/s and 1548 +/- 27 m/s, respectively.[30]

In an isotropic elastic medium, ultrasound propagates in two main wave modes. The speed of longitudinal (α) waves, which move in the same direction as propagation, is given by the equation below. The speed of shear (β) waves, which move perpendicular to the direction of propagation, is also below:

$$\alpha = \sqrt{\frac{\lambda + 2\mu}{\rho}}$$ where λ and μ are Lame constants

$$\beta = \sqrt{\frac{\mu}{\rho}}$$

The amplitude wave of an ultrasound signal can also be modeled as a pressure wave, which makes its modeling via finite element analysis possible. Details on loading conditions for the simulation can be found in the methods section.

Need Statement

Accurate localization of nonpalpable breast lesions is a critical step in ensuring successful surgical excision, yet the current technologies highlighted above fall short in multiple domains. Wire localization, though cost-effective and widely used, requires same-day placement and introduces patient discomfort due to its invasive nature and external component, which can shift or fracture. Radioactive seed localization involves radiation exposure for both patients and healthcare workers, limiting its safety and acceptability. Magnetic and radar-based systems, such as Magseed and SAVI SCOUT, carry high

equipment costs and are incompatible with MRI, further constraining their applicability. Thus, all implantable techniques require additional preoperative procedures and carry scheduling complexities. Additionally, IOUS offers a non-invasive alternative with lower re-excision rates, yet its real-time application demands a high level of training and suffers from steep learning curves. It also primarily utilizes B-mode imaging, which is susceptible to lack of reliable depth resolution, particularly for small or deep tumors. Across all existing techniques, there is a recurring lack of real-time, depth-specific feedback that is both easy to interpret and integrates seamlessly into the surgical workflow.

Therefore, this current landscape underscores a pressing need for a non-invasive, low-cost, and user-friendly localization method that enhances surgical accuracy and reduces reoperation rates. A promising direction lies in using A-scan ultrasound data for depth estimation, which offers improved one-dimensional precision and can be implemented without additional hardware or preoperative steps. By leveraging finite element analysis to simulate tissue-specific wave propagation and developing a computational framework to interpret signal reflections, this approach aims to address the technical and clinical shortcomings of existing localization methods, while streamlining intraoperative workflow.

II. Project Objectives

Considering the limitations of current localization strategies for non-palpable breast tumors, including invasiveness, equipment interference, cost, patient discomfort, and limited real-time adaptability, our project presents an alternative localization method utilizing A-scan ultrasound signal data. The proposed solution leverages finite element analysis to simulate an ultrasound signal passing through various breast-tumor models with differing tumor locations and sizes. The resulting time-domain simulation signals are subsequently analyzed using peak- and dip-based depth estimation methods in order to efficiently and accurately localize the embedded tumor. This approach bypasses additional pre-surgical procedures, therefore streamlining hospital workflow, improving patient comfort, and reducing the need for re-operation.

Aim I. To simulate the interaction of an A-scan ultrasound wave with breast tissue models containing an embedded tumor of various locations and sizes using finite element analysis in Abaqus.

Aim II. To develop a Python-based computational method for estimating tumor depth from the surface of the breast tissue based on time-domain ultrasound signal analysis.

Aim III. To evaluate the accuracy of the localization method by calculating percent error between the predicted and known tumor depths across multiple simulated scenarios.

III. Design Process and Methods

Model Development

Geometry and Assembly

A simplified 2D breast model was constructed in Abaqus/CAE to simulate ultrasound propagation and tumor detection.[30] The breast was defined as a deformable solid hemisphere with a radius of 40 mm. A secondary circular tumor with a specified diameter was positioned within the phantom using the Assembly Module. A diameter of 10 mm was chosen as the upper limit for non-palpable lesions. Other tumor diameters tested were 7.5, 6, and 5 mm.

Tumor positions were varied across simulations to assess the effect of location on ultrasound response. The positions were strategically placed at depths of 0, 2.5, 5, 7.5, 10, and 12.5 mm offset from the center of the breast moving both upwards and downwards. Both the breast and tumor geometries were generated using the Sketch Module, and partitioning operations were applied to distinguish between the two materials.

Due to the axisymmetric constraint of the 2D model, the tumor was intentionally kept on the central vertical axis. Translating the tumor horizontally in such a model would violate the axisymmetric assumption by introducing a mirrored duplicate of the tumor on the opposite side of the axis. Such duplication would significantly distort the signal interpretation and invalidate the intended single-tumor analysis. Therefore, in order to move the tumor horizontally, a fully 3D model would be required. However, transitioning to a 3D geometry would significantly increase computational costs, as the meshing would generate orders of magnitude more elements, significantly increasing simulation time and memory requirements. So the axisymmetric 2D design was chosen to balance geometric relevance with computational efficiency, while still capturing the physics of tumor-breast ultrasound wave propagation.

Material Properties

Distinct material properties were assigned to the breast tissue and tumor regions. The tissue was modeled as nearly incompressible to reflect soft biological behavior. The tumor was modeled as a stiffer, denser region to reflect common clinical characteristics of malignant lesions. Specific parameters were as follows:

Material Property	Breast Tissue	Tumor
Density (kg/m^3)	1000	1040
Elastic Modulus (Pa)	2.0x10^4	2.0x10^6
Poisson's Ratio	0.4999985	0.49985

The Poisson's ratio was computed dynamically from the elastic modulus and density using the following relation derived from the speed of sound:

$$v = \frac{1}{2}\left(-\frac{E}{3\rho c^2} + 1\right)$$

where E is Young's Modulus, ρ is the tumor density, and c is speed of sound, fixed at 1480 m/s.

Mesh Generation

The breast-tumor assembly was then meshed using structured quadrilateral elements with a refined mesh size calculated based on ultrasound wavelength considerations to ensure high simulation accuracy. A mesh size was selected to ensure there were at least 10 elements per wavelength, maintaining numerical accuracy in resolving the wave dynamics. The element size was determined based on the wavelength (λ) of the ultrasound wave in the breast tissue and speed of sound given by:

$$\lambda = \frac{c}{f} = \frac{c}{1\times10^6\ 1/s}$$

To accurately capture wave propagation, a minimum of 10 elements per wavelength is required, leading to an element size selection of $\frac{\lambda}{10}$. The meshing can be seen in the Abaqus/CAE model image below.

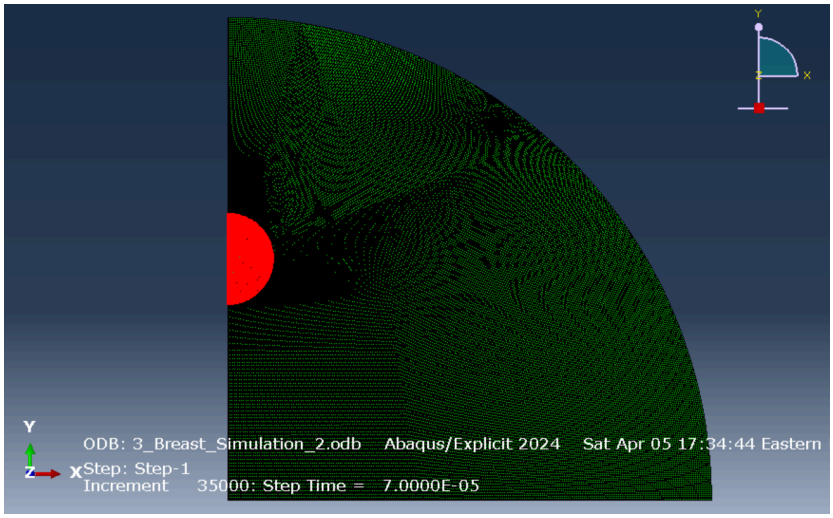

Figure 6. *Visualization of breast-tumor assembly meshing (green) with highlighted embedded tumor (red).*

Boundary Conditions

The bottom of the breast phantom was constrained with an Encastre (U1 = U2 = U3 = 0) boundary condition to simulate a rigid interface. The plane along the Y-axis (XZ-plane, where Y = 0) was constrained using U2 = 0, ensuring proper symmetric behavior. A Dynamic Explicit Step was also created to simulate ultrasound wave propagation with the following parameters:

Time Period: 70 μs (7.0e-5 s)

Time Increment: 2 ns (2.0e-9 s)

Nonlinear Geometry: Enabled (to account for large deformations)

Ultrasound Probe Surface and Pressure Load Application

The ultrasound transducer was simulated as a 12 mm circular region on the top surface of the breast phantom, as seen in Figure 7. A uniform pressure load was applied to the probe surface with the following parameters:

Load Type: Pressure

Distribution: Uniform

Amplitude Function: $P(t) = cos(2\pi ft)[1 - cos(2\pi ft/m)]$

where f = 1MHz (wave frequency) and m = 2 (pulse modulation factor). These boundary conditions and load applications ensured realistic simulation of ultrasound wave interactions with the breast model.

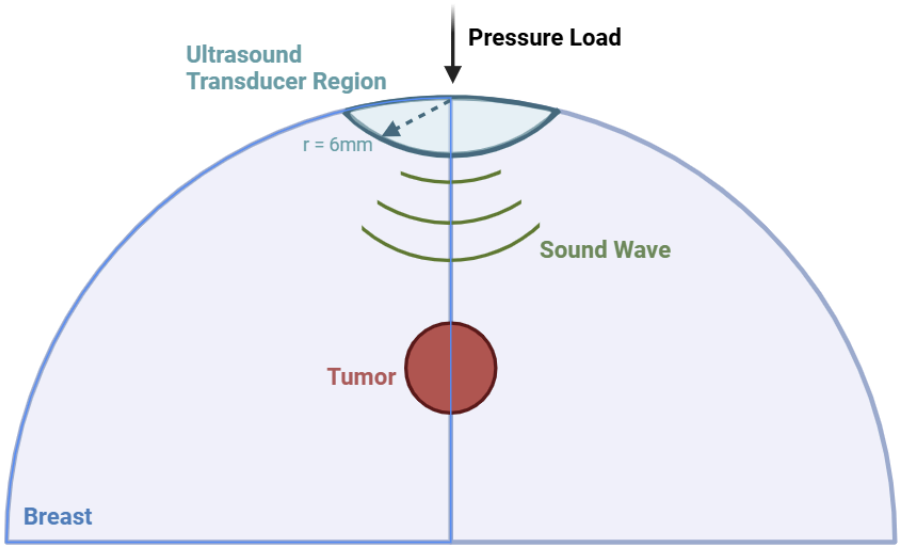

Figure 7. *Diagram of simulated ultrasound transducer region, sound wave propagation, and applied pressure load.*

Experimental Conditions

This study tests a range of experimental conditions to evaluate how tumor location and size influence ultrasound response in the simulated breast model and if the method would be able to accurately detect tumor depth under various experimental conditions.

To assess the sensitivity of ultrasound signal features to tumor location, we placed the tumor at various depths along the central vertical axis of the breast model. These depths were selected to represent clinically relevant positions of nonpalpable lesions and to ensure that tumor depths were distributed along the entirety of the breast model.

$$Depths\ (mm)\ =\ \{0,\ \pm\ 2.5,\ \pm\ 5.0,\ \pm\ 7.5,\ \pm\ 10.0,\ \pm\ 12.5\}$$

Tumor sizes were also varied to test the method's sensitivity to smaller tumors representative of nonpalpable lesions. Nonpalpable lesions are typically 10 mm in diameter or smaller so the following tumor diameters were selected:

$$Diameters\ (mm)\ =\ \{5,\ 6,\ 7.5,\ 10\}$$

The tumor depths were selected in 2.5 cm increments, so the inclusion of a 6 mm tumor was intentional to avoid overly regular spacing in the expected depth values. Without it, the combination of uniform offsets and diameters would have resulted in depth estimates that fell into predictable increments of 0.0025 m, potentially masking subtle differences in algorithm performance.

Data Preprocessing

The simulation data was preprocessed using Python's pandas library. Initially, the dataset was imported from a csv file. Subsequently, the signal from the simulation was visualized to examine the amplitude variation over the sampling points, as seen in Figure 8. This provided an initial assessment of the signal characteristics. The signal was truncated based on a predefined total time of 3 x 10^{-6} seconds and a time increment of 2 x 10^{-9} seconds, resulting in a specific sampling range. The purpose of this truncation was to remove the initial ultrasound impulse that is present in every signal and to remove the signal tail, when the ultrasound wave has passed through the medium and the transducer is no longer collecting data. The truncated data, ranging from the calculated sampling number to 27,000, was then prepared for scaling. Min-Max scaling was applied to normalize the data, ensuring that all feature values fell within the same range, thus facilitating improved performance in downstream analyses and consistent application of thresholds. The resulting, preprocessed signal visualization can be seen in Figure 9.

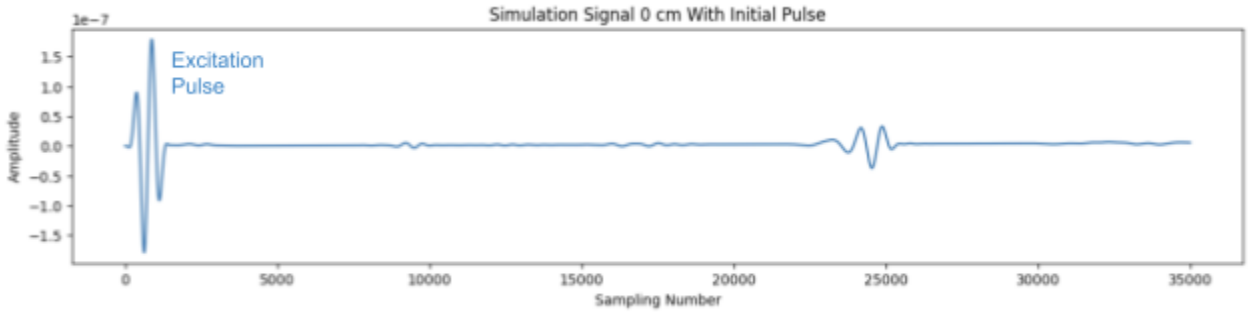

Figure 8. *Raw ultrasound signal collected for the 0 cm tumor offset case, including the initial pulse. The dominant reflection early in the signal represents the excitation pulse from the probe, while subsequent features correspond to tissue interfaces and tumor boundaries.*

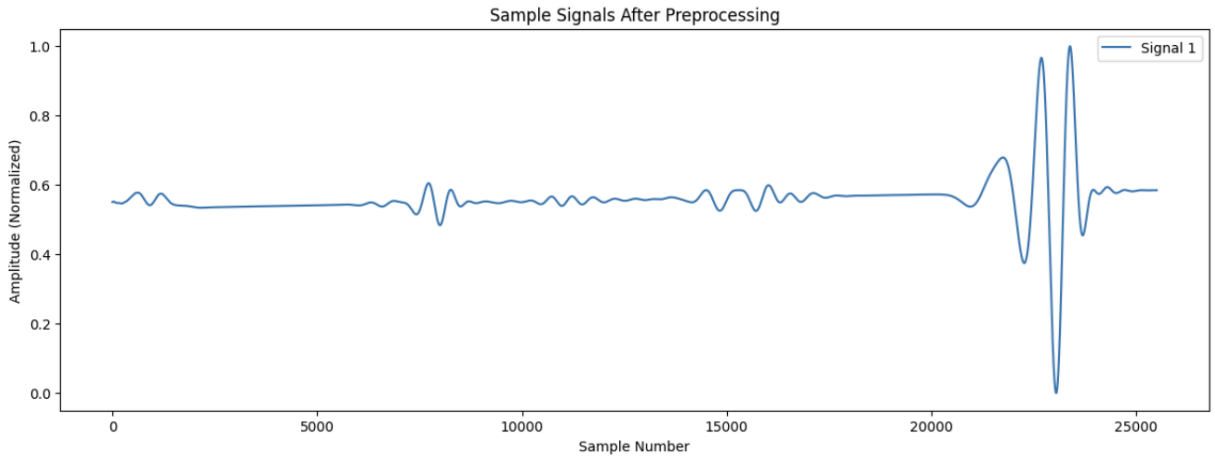

Figure 9. *Preprocessed and normalized ultrasound signal after truncating the first 3 μs to remove the initial pulse and the final 27 μs to eliminate back-wall reflections. The scaled signal reveals tumor-related features more clearly and prepares the data for peak detection.*

Developing the Method

To extract the tumor depth from the simulated ultrasound signals, a peak detection-based method was developed. This method assumes that the earliest strong reflection in the signal corresponds to the ultrasound wave reflecting off the surface of the tumor. Given that the ultrasound wave must travel to the tumor and back, the depth was calculated using the following formula:

$$d = \frac{c \cdot t}{2}$$

where c is the speed of sound of the breast tissue and t is the round trip time based on the first reflection peak. The time was calculated by multiplying the detected sample index by the known time increment of 2 ns per sample and adding the 3 μs truncation offset.

To ensure strong performance across varying tumor depths and tissue properties, two versions of the method were implemented, one that detects peaks, positive reflections, and another that detects dips, negative reflections. In the signals, the dips and peaks often appeared closely together in clusters. Therefore, we wanted to investigate if detecting one significant feature of interest, a dip or a peak, would result in different or better performance than the other. The dip-based method simply inverts the signal and applies the same peak-finding logic.

Both methods use SciPy's find_peaks function with adjustable thresholds for minimum amplitude and minimum distance between detected features. The default thresholds were set to a

height of 0.5 and a minimum distance of 10000 samples for peaks and -0.5 and 1000 for dips, chosen to balance sensitivity to meaningful reflections while minimizing the detection of noise. However, in certain scenarios, particularly for tumors located farther away from the probe or in cases with high noise, these parameters required slight adjustment to ensure accurate detection. These modifications and their effects on depth estimation accuracy are discussed further in the Results and Discussion section.

By comparing depth estimates obtained from both approaches across multiple tumor positions, it was possible to identify which method yielded more consistent and accurate results under different conditions. This dual-method comparison also allowed for more comprehensive evaluation of the signal characteristics and validated the method's adaptability to real-world scenarios, where the signal environment may not be idealized.

Optional plotting functionality was also included to visualize the detected peaks overlaid on the signal waveform, providing a helpful diagnostic tool to verify the method's performance. This method balances simplicity and computational efficiency, making it well-suited for rapid evaluation of multiple simulations. Examples of signal peaks and their corresponding calculations can be found in Appendix E.

Assessing the Method

To assess the accuracy of the proposed localization method, the known tumor depth of each simulation scenario was compared to the estimated depth derived from the A-mode ultrasound signal response. The known depth was calculated based on the height of the breast hemisphere, the offset of the tumor from the center, and the radius of the tumor:

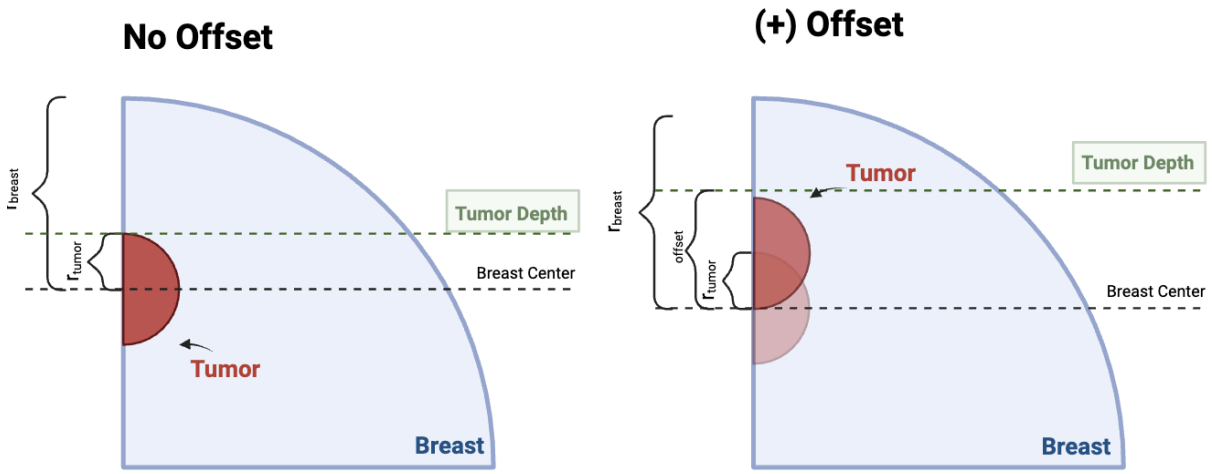

Figure 10. *Schematic illustration of tumor depth calculations used for error analysis. The "No Offset" diagram shows a tumor positioned at the breast center, while the "(+) Offset" diagram demonstrates a tumor shifted upward from center.*

$$True\ Depth\ = \frac{r_{breast}}{2} \pm offset\ - r_{tumor}$$

To assess localization accuracy, the absolute error between the estimated and true tumor depths was computed for each simulation as:

$$Absolute\ error\ = |Estimated\ Depth\ -\ True\ Depth|$$

Percent error was also computed for each simulation as:

$$\%\ error\ = \frac{|Estimated\ Depth - True\ Depth|}{True\ Depth}$$

IV. Results and Discussion

To evaluate the performance of the depth estimation method, tumor depths were calculated using two different approaches: one based on detecting dips and one based on detecting peaks in the ultrasound signal. Both methods were applied across eleven simulations per tumor, in which the tumor was positioned at varying vertical offsets above and below the center of a 40 mm tall breast phantom. Figure 11 below is an example of identifying dips and peaks in the same signal from a centered 10 mm tumor. The calculated depths were compared against known ground truth values derived from the simulation geometry, and error was computed for each scenario.

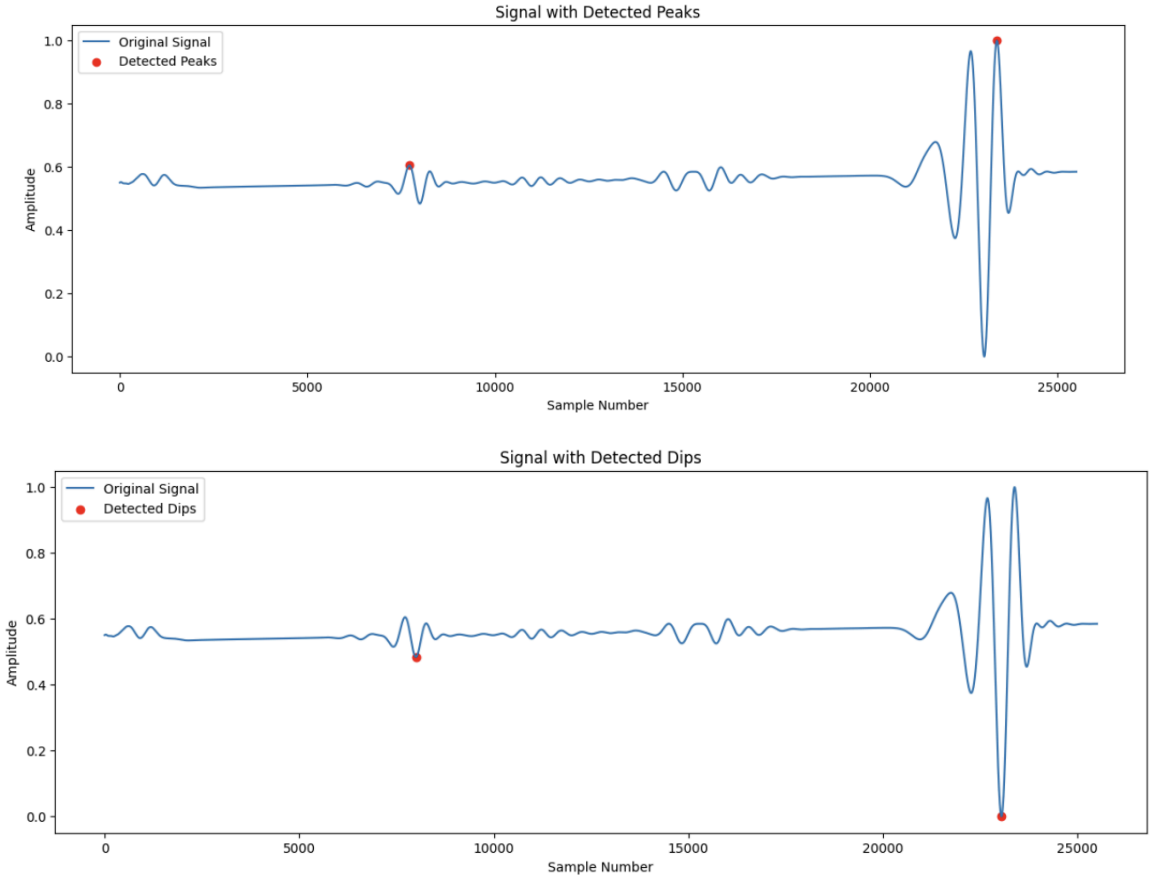

Figure 11. *Detected peaks overlaid on the normalized and truncated ultrasound signal for the 10 mm tumor, 0 mm offset case. The first significant peak corresponds to the reflection from the tumor surface and is used to calculate the tumor depth based on time and known tissue speed of sound.*

Dip-Based Estimation

The dip-based method demonstrated generally high accuracy in estimating tumor depth, especially for tumors positioned near the center of the breast. Table 2 shows the results for the dip-based estimation for the case of the 10 mm tumor at various offsets from the center. At 0 mm and 5 mm upward offsets from the center in this case, the percent error was as low as 5.65% and 0.66%, respectively. The accuracy gradually decreased at more extreme offsets. At a 12.5 mm upward offset, which is the tumor placement closest to the breast surface, the method yielded a 23.12% error, likely due to reduced amplitude of the early reflection and proximity to the truncation boundary.

Table 2. *Dip-based estimation results for 10 mm diameter tumor at various offsets from center.*

Offset (mm)	Expected Depth (mm)	Calculated Depth (mm)	Absolute Error (mm)	% Error
+12.5	2.50	3.078	0.578	23.12
+10.0	5.00	5.146	0.146	2.92
+7.50	7.50	7.215	0.285	3.81
+5.00	10.0	10.066	0.066	0.66
+2.50	12.5	12.044	0.456	3.65
0.00	15.0	14.152	0.848	5.65
-2.50	17.5	16.152	1.348	7.71
-5.00	20.0	18.191	1.809	9.04
-7.50	22.5	21.583	0.917	4.08
-10.0	25.0	21.471	3.529	14.12
-12.5	27.5	21.179	6.321	22.99

For tumors located below the center, and therefore deeper within the tissue, the dip-based method also performed reasonably well for moderate depths, with errors of 7.71% and 9.04% at 2.5 mm and 5 mm offsets, respectively. However, accuracy decreased at deeper locations, where percent error rose to 14.12% at the 10 mm downward offset and 22.99% at the 12.5 mm

downward offset. These observations suggest that deeper tumor signals may be attenuated or masked by an accumulation of interfering reflections and noise.

In general, detecting dips for offsets with the 10 mm tumor required uniform parameters, demonstrating the dip-based method's consistency across a wide range of tumor positions. As shown in Appendix A (Table A1), a dip height threshold of –0.5 and a minimum distance of 10,000 samples were sufficient for accurate detection in most simulations. However, for deeper tumors located below the center, manual adjustment of detection parameters was occasionally required for identification of the dip of interest. While the height threshold and minimum distance remained numerically the same, manual intervention was needed to select the correct dip, which was often the second significant feature instead of the first. This adjustment was necessary to avoid capturing early noise-induced dips that would have led to underestimation of the tumor depth.

Table 3. *Dip-based estimation results for 7.5 mm diameter tumor at various offsets from center.*

Offset (mm)	Expected Depth (mm)	Calculated Depth (mm)	Absolute Error (mm)	% Error
+12.5	3.75	4.112	0.362	9.6533
+10.0	6.25	6.146	0.104	1.664
+7.50	8.75	8.675	0.075	0.8571
+5.00	11.25	11.135	0.115	1.0222
+2.50	13.75	13.166	0.584	4.2473
0.00	16.25	15.129	1.121	6.8985
-2.50	18.75	17.233	1.517	8.0907
-5.00	21.25	18.191	3.059	14.3953
-7.50	23.75	21.361	2.389	10.0589
-10.0	26.25	21.583	4.667	17.7790
-12.5	28.75	21.179	7.571	26.3339

Table 3 presents the dip-based depth estimation results for a tumor with a 7.5 mm diameter placed at various vertical offsets from the center of a 4 cm tall breast phantom. The algorithm performed most accurately when the tumor was placed closer to the center of the breast at smaller offset magnitudes. For example, at a +5 mm offset, the percent error was only 1.02%, and at +7.5 mm, it was even lower at 0.86%. However, at the farthest upward offset (+12.5 mm), the percent error rose to 9.65%.

As the tumor position moved downward from the center (negative offsets), performance gradually deteriorated. Moderate offsets like –2.5 mm and –7.5 mm still yielded reasonably accurate estimates, with errors of 8.09% and 10.06%, respectively, However, at –10 mm, the error reached 17.78%, and at the deepest offset (–12.5 mm), error reached 26.33%. This trend suggests that, at greater depths, the signal-to-noise ratio may decrease, making relevant reflections more likely to be masked by attenuation or interference from boundary echoes, complicating the identification of the correct dip.

Table 4. *Dip-based estimation results for 6 mm diameter tumor at various offsets from center.*

Offset (mm)	Expected Depth (mm)	Calculated Depth (mm)	Absolute Error (mm)	% Error
+12.5	4.50	4.746	0.246	5.4667
+10.0	7.00	7.820	0.820	11.7143
+7.50	9.50	9.666	0.166	1.7474
+5.00	12.0	11.819	0.181	1.5083
+2.50	14.5	13.727	0.773	5.3310
0.00	17.0	15.785	1.215	7.1471
-2.50	19.5	17.826	1.674	8.5846
-5.00	22.0	20.644	1.356	6.5685
-7.50	24.5	24.579	0.079	0.3224
-10.0	27.0	21.116	5.884	21.7926
-12.5	29.5	20.777	8.723	29.5695

Table 4 summarizes the accuracy of the dip-based depth estimation algorithm for a tumor with a 6 mm diameter, placed at various vertical offsets from the center of the breast phantom. The algorithm performed well across the positive offsets, achieving sub-2% error at offsets of +5.0 mm (1.51%) and +7.5 mm (1.75%). However, for more shallow tumors at +10.0 mm and +12.5 mm, the error increased to 11.71% and 5.47%, respectively, possibly due to the proximity to the initial pulse.

For tumors placed below the center at downard offsets, performance varied. Moderate depths such as –2.5 mm to –5.0 mm produced reasonably low errors ranging from 6.57% to 8.58%, and a very low error of 0.32% was observed at –7.5 mm. However, the performance again decreased substantially at the deepest positions, specifically –10.0 mm and -12.5 mm, which yielded errors of 21.79% and 29.57%, likely due to the noise and attenuation complications discussed previously.

Table 5. *Dip-based estimation results for 5 mm diameter tumor at various offsets from center.*

Offset (mm)	Expected Depth (mm)	Calculated Depth (mm)	Absolute Error (mm)	% Error
+12.5	5.00	5.138	0.138	2.7600
+10.0	7.50	8.147	0.647	8.6267
+7.50	10.0	10.126	0.126	1.2600
+5.00	12.5	12.136	0.364	2.9120
+2.50	15.0	14.149	0.851	5.6733
0.00	17.5	16.210	1.290	7.3714
-2.50	20.0	15.362	4.638	23.1900
-5.00	22.5	22.781	0.281	1.2489
-7.50	25.0	23.420	1.580	6.3200
-10.0	27.5	33.038	5.538	20.1382
-12.5	30.0	31.636	1.636	5.4533

Table 5 shows the dip-based depth estimation results for a 5 mm diameter tumor, with surface depths calculated from the known tumor center and radius. The method continued to

perform particularly well for tumors offset slightly above center. At +7.5 mm and +12.5 mm, the percent errors were just 1.26% and 2.76%, respectively. However, performance declined at certain locations, such as the +10 mm position with an error of 8.63% and the -10 mm position with an error of 20.14%. Interestingly, the offset at −2.5 mm showed a substantial overestimation, with a 23.19% error, likely due to the presence of early noise-driven dips that could have been misidentified as tumor reflections.

Despite these outliers, the algorithm maintained errors below 6.5% for 9 out of the 12 positions, suggesting generally accurate performance. Nevertheless, these results suggest that dip detection can struggle with precision at the larger offset magnitudes, particularly when the tumor reflection is weak or when noise produces misleading features.

Peak-Based Estimation

The second version of the method used peaks, or positive reflections, instead of dips, to estimate tumor depth in various simulated configurations, also showing promising results.

Table 6. *Peak-based estimation results for 10 mm diameter tumor at various offsets from center.*

Offset (mm)	Expected Depth (mm)	Calculated Depth (mm)	Absolute Error (mm)	% Error
+12.5	2.50	3.461	0.961	38.4400
+10.0	5.00	5.529	0.146	10.5800
+7.50	7.50	7.627	0.127	1.6900
+5.00	10.0	9.651	0.349	3.4900
+2.50	12.5	11.650	0.850	6.8000
0.00	15.0	13.738	1.262	8.4100
-2.50	17.5	17.786	0.286	1.6300
-5.00	20.0	19.842	0.158	0.7900
-7.50	22.5	21.583	0.917	4.0800
-10.0	25.0	21.997	3.003	12.0120
-12.5	27.5	20.093	7.407	26.9300

Table 6 shows the results of the peak-based estimation for a 10 mm tumor at various offsets from the center. Notably, at 5 mm and 7.5 mm downward offsets, the method achieved very low percent errors of 0.79% and 4.08%, respectively, slightly outperforming the dip-based approach for these signals. In the upward direction, the peak-based method performed well at intermediate offsets, with 1.69% error at 7.5 mm and 3.49% at 5 mm. However, it was significantly less consistent at the extremes, where the error rose to 10.58% and 38.44% at the 10 mm and 12.5 mm upward offsets, respectively, highlighting a vulnerability in detecting shallow tumors where the positive reflection is weak or ambiguous.

Table 7. *Peak-based estimation results for 7.5 mm diameter tumor at various offsets from center.*

Offset (mm)	Expected Depth (mm)	Calculated Depth (mm)	Absolute Error (mm)	% Error
+12.5	3.75	4.473	0.723	19.2800
+10.0	6.25	6.563	0.313	5.0080
+7.50	8.75	8.675	0.075	0.8571
+5.00	11.25	10.721	0.529	4.7022
+2.50	13.75	12.731	1.019	7.4109
0.00	16.25	14.723	1.527	9.3969
-2.50	18.75	16.825	1.925	10.2667
-5.00	21.25	17.786	3.464	16.3012
-7.50	23.75	21.791	1.959	8.2484
-10.0	26.25	19.842	6.408	24.2114
-12.5	28.75	20.093	8.657	30.1113

Table 7 presents the results of tumor depth estimation using the peak-based approach for a 7.5 mm diameter tumor at various offsets from the center of the breast phantom. At intermediate tumor positions, the peak-based method performed relatively well. For example, at +7.5 mm from center, the calculated depth had a percent error of just 0.86%, indicating accurate

identification of the tumor surface. Similarly, the offsets at +5.0 mm and +10.0 mm yielded errors of 4.70% and 5.01%, respectively.

However, as the tumor moved deeper into the phantom, the error grew substantially. At −2.5 mm, the error exceeded 10%, and at −10 mm and −12.5 mm, it rose sharply to 27.14% and 17.79%, respectively. The least accurate performance was observed at the most extreme depths, with the peak detection significantly underestimating deeper tumor surface location and overestimating more shallow tumor surface locations.

Table 8. *Peak-based estimation results for 6 mm diameter tumor at various offsets from center.*

Offset (mm)	Expected Depth (mm)	Calculated Depth (mm)	Absolute Error (mm)	% Error
+12.5	4.50	5.111	0.611	13.5778
+10.0	7.00	7.265	0.265	3.7857
+7.50	9.50	9.266	0.234	2.4632
+5.00	12.0	11.397	0.603	5.0250
+2.50	14.5	13.324	1.176	8.1103
0.00	17.0	15.366	1.634	9.6118
-2.50	19.5	18.212	1.288	6.6051
-5.00	22.0	19.415	2.585	11.7500
-7.50	24.5	23.599	0.901	3.6776
-10.0	27.0	20.684	6.316	23.3926
-12.5	29.5	21.131	8.369	28.3695

Table 8 shows the peak-based estimation results for a 6 mm diameter tumor at various vertical offsets from the center of the breast. The algorithm performed best for mid-range depths above the center, particularly at offsets of +7.5 mm and +10.0 mm, where percent errors were just 2.46% and 3.79%, respectively. Accuracy declined slightly at +5.0 mm and +2.5 mm with errors of 5.03% and 8.11%, though still within a tolerable range of below 10%.

At the most shallow position of +12.5 mm, the error increased sharply to 13.58%, again highlighting the challenges of early signal distortion near the probe. Similarly, at the deepest offsets of -10 mm and -12.5 mm, the accuracy diminished with errors of 23.39% and 28.37%. This is consistent with the pattern seen for deeper tumors in other tumor sizes as well, where error increases due to accumulating interference and noise.

Table 9: *Peak-based estimation results for 5 mm diameter tumor at various offsets from center.*

Offset	Expected Depth (m)	Calculated Depth (m)	Absolute Error	% Error
+12.5	5.00	5.500	0.500	10.000
+10.0	7.50	7.720	0.220	2.9333
+7.50	10.0	9.710	0.290	2.9000
+5.00	12.5	11.719	0.7812	6.2492
+2.50	15.0	13.738	1.262	8.4147
0.00	17.5	15.781	1.719	9.8229
-2.50	20.0	14.979	5.021	25.1050
-5.00	22.5	23.247	0.747	3.3200
-7.50	25.0	22.950	2.050	8.2000
-10.0	27.5	30.469	2.969	10.7964
-12.5	30.0	32.185	2.185	7.28330

Table 9 presents the results of peak-based estimation for a 5 mm diameter tumor placed at various offsets from the center of the breast phantom. The algorithm achieved its best accuracy at +7.5 mm and +10 mm, with percent errors of 2.9% and 2.93%, respectively. The offset at +5 mm yielded a moderately low error of 6.25%, while more superficial depths, such as the +2.5 mm and +12.5 mm offsets, showed higher errors of 8.41% and 10.0%, respectively. These results align with previous observations suggesting that tumors near the probe are more likely to exhibit ambiguous or low-amplitude early reflections, reducing accuracy.

Notably, the error increased slightly at some of the deeper offsets. The case at -2.5 mm had the highest error overall, at 25.1%. Other lower-positioned tumors, such as the -10.0 mm and -12.5 mm, produced errors of 10.80% and 7.28%, reflecting the method's reduced reliability at greater depths, where peak amplitude diminishes and overlapping signals become more problematic.

Comparison of Approaches

To evaluate the effectiveness of our tumor localization strategy, we implemented and tested two complementary signal-processing approaches, one that detects peaks and another that detects dips in A-mode ultrasound signals. Each method was applied across the full set of simulation scenarios, encompassing varying tumor sizes and positions. This comparison allowed us to assess how different signal features influence the accuracy of depth estimation and to identify which approach offers greater consistency under variable signal conditions. The findings also provide insight into how signal characteristics and parameter tuning may affect overall performance and robustness in clinical-like environments.

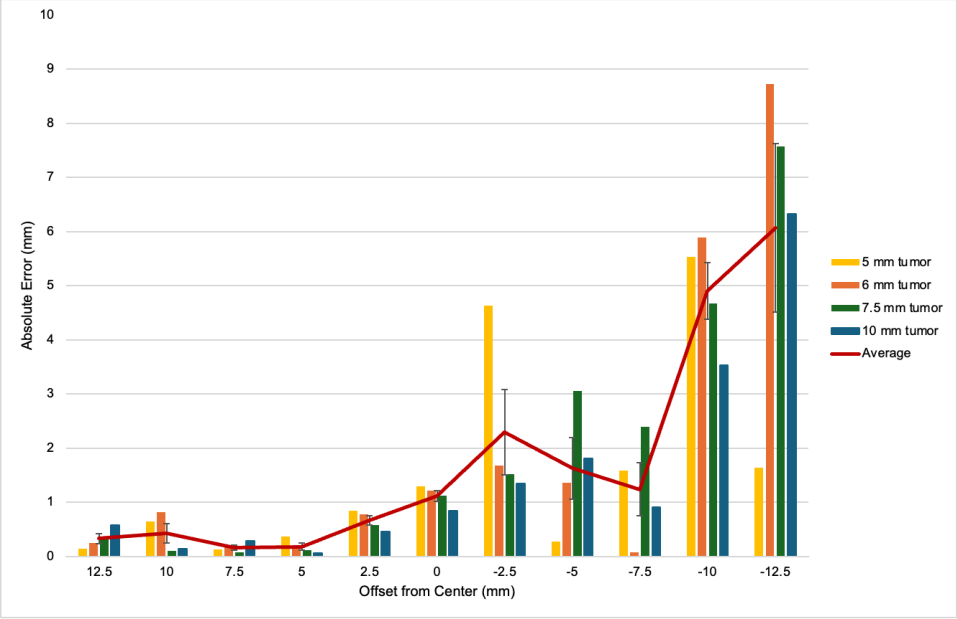

Figure 12. *Absolute error as a function of offset from the center for each tumor diameter based on the results from the dip-based method. Average percent error for each case shown. Error bars represent the standard error of the mean (n=4).*

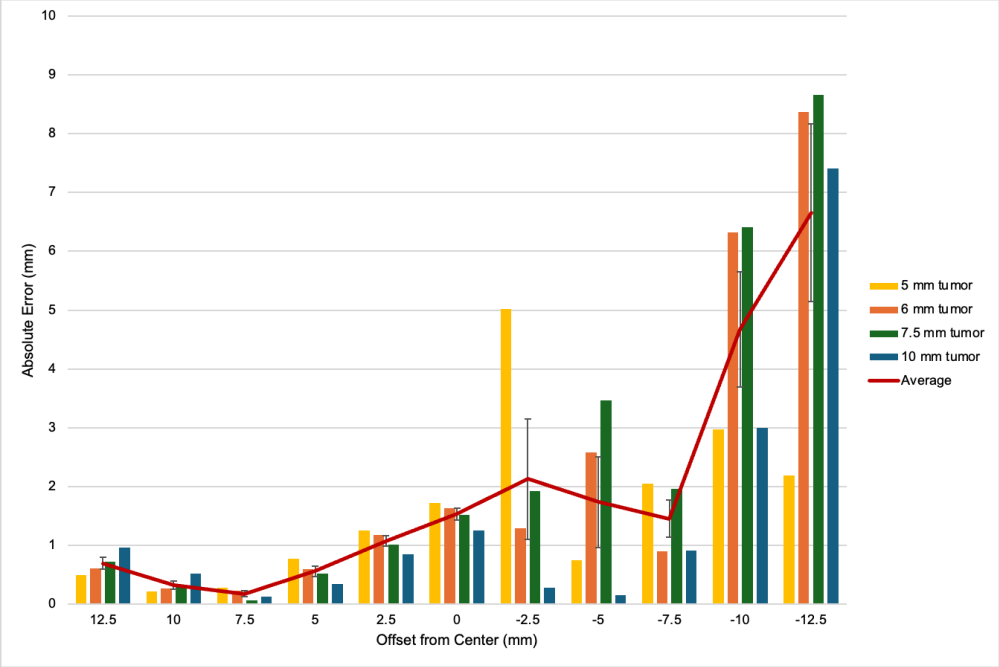

Figure 13. *Absolute error as a function of offset from the center for each tumor diameter based on the results from the peak-based method. Average percent error for each case shown. Error bars represent the standard error of the mean (n=4).*

Figures 12 and 13 above compare the absolute error in tumor localization as a function of offset from the tumor center using the dip-based and peak-based analytical methods, respectively. Each series reflects the errors for one of the four tumor sizes, 5 mm, 6 mm, 7.5 mm, and 10 mm, while the red line represents the average percent error across all diameters, with error bars denoting the standard error of the mean (n=4). It is notable that there is no correlation between tumor size and depth estimation accuracy across offsets.

For both depth-estimation methods, the absolute error shows a positive correlation with increasing depth. The absolute error generated from the estimations is therefore lowest in breast-tumor model configurations where the tumor is embedded closest to the upper surface of the breast tissue. In general, the absolute error is kept under about 2 mm for a majority of the offsets, and then steeply increases for the last two offsets, where the tumor is most deeply embedded. This reduced accuracy can be attributed to wave attenuation as it travels through the medium, making it more difficult to distinguish between the reflection of interest and accumulated noise or interference.

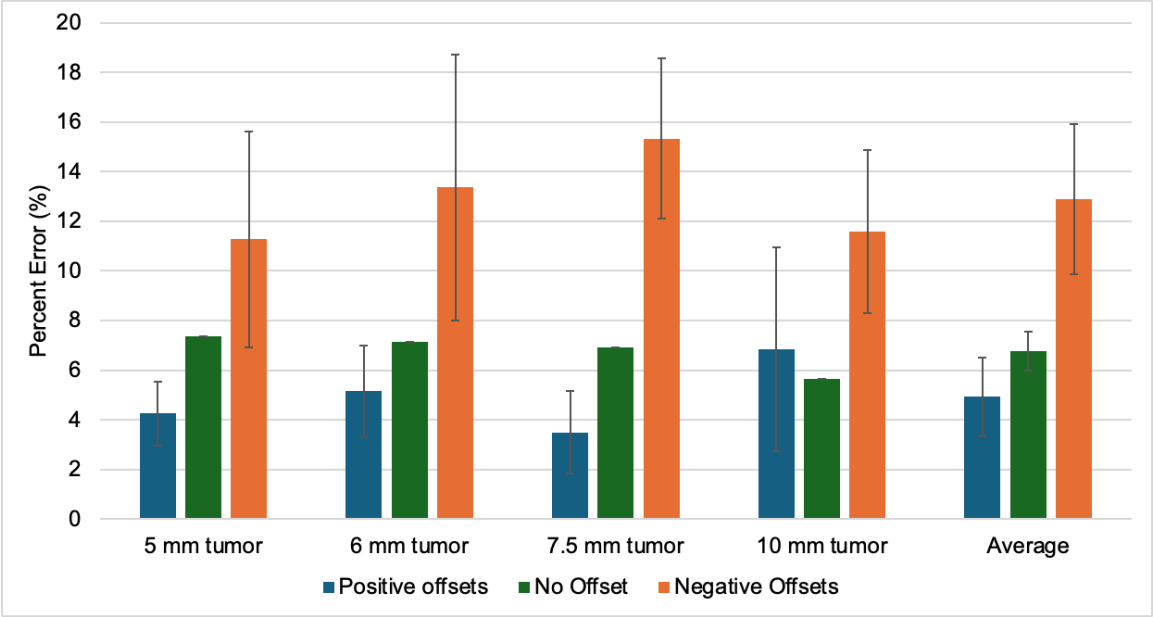

Figure 14. *Dip-based method percent error averages for positive (blue), negative (orange), and no (green) offsets across tumor sizes. Error bars represent the standard error of the mean (n=5).*

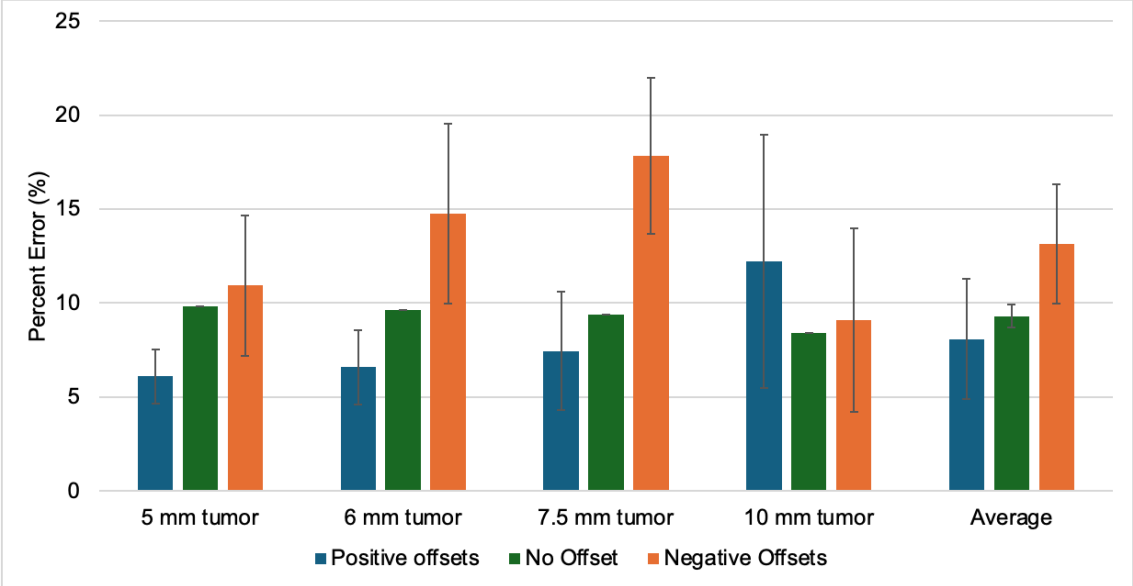

Figure 15. *Peak-based percent error averages for positive (blue), negative (orange), and no (green) offsets across tumor sizes. Error bars represent the standard error of the mean (n=5).*

As seen in Figures 14 and 15 above, for both of the depth-estimation methods, the negative offsets consistently yield the highest percent errors, while the positive offsets and

no-offset cases yield lower errors. For the dip-based method, the positive, neutral, and negative offset averages are 4.93%, 6.77%, and 12.89%, respectively. For the peak-based method, the positive, neutral, and negative offset averages are 8.09%, 9.31%, and 13.15%, respectively. This pattern suggests an asymmetry in performance, where both methods are more sensitive to negative shifts in tumor position than positive shifts.

***Table 10**. Average error comparison for dip and peak-based methods, grouped by tumor offset direction relative to the breast center.*

	Dip Average % Error	Peak Average % Error
Positive Offset	4.93018	8.08587
Baseline	6.76675	9.3104
Negative Offset	12.88929	13.154025
Total	8.71491	10.50089

When comparing the overall performance of the dip based and peak-based, the dip-based approach consistently demonstrated lower average percent error across all tumor positions. Table 10 presents a comparison of the average percent error between the dip-based and peak-based tumor localization methods, grouped by tumor offset direction. The error at negative offsets is higher than for the baseline and positive offsets, consistent with the trend observed across individual simulation results where tumors positioned deeper resulted in less accurate depth estimations. However, the difference in performance between the dip-based and peak-based methods at these negative offsets is smaller compared to the other scenarios. This suggests that at greater depths, both methods are similarly affected by signal degradation, reducing the advantage of one approach over the other.

Interestingly, the results show that the dip-based method consistently outperformed the peak-based method. This could be because the dips often had a sharper and deeper amplitude, making them easier to distinguish from background noise or smaller early reflections. Additionally, the dip-based method used a smaller distance threshold than the peak-based approach, which may have made it more sensitive to relevant features in the signal. In general, these findings suggest that when the signal environment is unknown and not idealized, which is

often the case in clinical settings, detecting dips may be the better default strategy or at least a more reliable starting point. Future work could also explore adjusting the distance threshold for the peak-based method to improve sensitivity. Ultimately, more testing under a wider variety of clinical conditions will be necessary to determine the most robust and generalizable approach.

Limitations

A key limitation of the current implementation is the reliance on fixed threshold values for peak and dip detection. While the default height and distance thresholds were used in most cases, some simulations required manual tuning to achieve optimal results. In simulations where the tumor was below the center of the breast, deeper in the tissue, the signal exhibited increased noise and early reflections, likely caused by acoustic scattering and interference. As a result, the method often detected an earlier peak or dip that did not correspond to the actual tumor reflection. In such cases, the correct tumor reflection was not the first but rather the second significant feature in the signal. To compensate for this, the index of the second peak had to be manually selected, undermining the fully automated nature of the proposed method and introducing subjectivity into the depth estimation process. Specific conditions for each depth estimation can be found in Appendix I.

Additionally, in some signals, particularly those with subtle reflections, the default parameters failed to capture any reliable peaks or dips. These cases required manual lowering of the height threshold and adjusting the inter-peak distance to ensure that at least three distinguishable features, peaks or dips, could be detected. This step was necessary to validate the presence of a reflection pattern and avoid misleading results. However, this further exposes the method's dependence on manual parameterization that may not generalize well across different tumor depths and sizes. The current approach assumes that the first strong feature represents the tumor surface, which does not always hold true in complex signal environments, especially at greater depths where attenuation and interference can occur.

In addition to these signal-processing limitations, several modeling assumptions may influence the generalizability of the results. The simulation was conducted on an idealized, homogeneous breast phantom with a single spherical tumor embedded along the central axis. Real human tissue is significantly more complex, exhibiting spatially varying acoustic properties, heterogeneous tissue layers, and nonlinear wave propagation effects that were not

accounted for in this study. The tumor was also assumed to have a smooth boundary and a fixed speed of sound, which may not hold true in clinical scenarios involving irregular lesions.

The final limitation arises from the mesh and trimming process in the Abaqus breast simulations, particularly when the tumor edge was positioned too closely to the boundary of the meshed region. In these cases, the proximity of the tumor to the edge of the trimmed geometry may have interfered with proper mesh generation or led to numerical instabilities, resulting in failed simulations or irregular pressure distributions. This was especially noticeable in cases such as the 10 mm tumor at a +12.5 mm offset and the 5 mm tumor at a -2.5 mm offset, both of which produced abnormal results and unusually large percent errors. These edge-related artifacts likely introduced additional error into the localization methods and underscore the importance of ensuring sufficient distance between the tumor and the mesh boundary in future modeling efforts.

V. Conclusions

This study presents a computational method for estimating the depth of breast tumors using A-mode ultrasound signals, highlighting two detection strategies: one based on signal dips and another based on peaks. The method relies on fundamental principles of ultrasound physics, specifically the time-of-flight of reflected acoustic waves, to estimate tumor surface depth. Two signal features were evaluated as potential indicators of tumor presence: the first significant negative reflection, or dip, and the first significant positive reflection, or peak. Both detection strategies were tested across 44 simulation cases covering four tumor sizes of 5 mm to 10 mm diameters and eleven vertical offsets per tumor, distributed above and below the center of a 4 cm tall breast phantom.

In comparing the two methodologies, the dip-based approach consistently demonstrated a slightly lower average percent error across nearly all offset directions and tumor sizes. At positive offsets, where tumors were located closer to the probe, the dip method achieved an average percent error of 4.93%, compared to 8.09% for the peak-based method. At negative offsets, both methods experienced greater difficulty due to signal attenuation and noise interference, but the dip method still slightly outperformed the peak-based method, with an error of 12.89% compared to 13.15%.

Importantly, the method's overall feasibility was demonstrated by its ability to achieve low error rates across a wide range of tumor positions and sizes. The dip-based detection strategy, in particular, proved to be consistent with minimal parameter tuning in most simulations. A fixed height threshold of –0.5 and minimum peak/dip spacing of 10,000 samples was sufficient for accurate depth localization in the majority of cases. However, the need for manual adjustment in some cases reflects a key limitation of the current methodology. In certain signals, particularly those involving deeper tumors or subtle reflections, the algorithm often identified early noise as the tumor surface, requiring manual selection of the second strongest dip or peak. In other cases, parameters like the height threshold had to be manually lowered to reveal significant features in low-contrast signals. These adjustments introduce subjectivity into the analysis and highlight the method's dependence on static thresholding, which may not generalize across all clinical scenarios.

Overall, this work demonstrates that a simple speed of sound based ultrasound processing method can achieve reliable tumor depth estimation across varied tumor sizes and positions. The

presented method is computationally inexpensive, requires no training data, and is based on an interpretable, physics-driven framework, making it well-suited for real-time intraoperative use. From a clinical standpoint, accurate depth estimation of nonpalpable tumors is critical for improving surgical precision and reducing reoperation rates in breast-conserving surgical procedures. Current localization techniques are often invasive, require additional procedures, and disrupt operating room workflow. In contrast, the proposed method could be integrated directly into standard intraoperative ultrasound systems, providing immediate feedback to the surgeon on tumor depth without the need for preoperative procedures and additional localization devices. The method's accuracy, interpretability, and efficiency make it a promising candidate for further development and potential real-time clinical implementation.

VI. Anticipated Regulatory Pathway

In terms of bringing a medical device to market, it is important to consider regulatory pathways, which ensure the safety and efficacy of a medical device before it reaches clinical use. The two primary regulatory pathways for medical devices in the U.S. are 510(k) clearance and Premarket Approval (PMA).[31] Firstly, there are three classes of medical devices classified by the FDA based on their risk level: Class I (low risk), Class II (moderate risk), and Class III (high risk requiring the most regulatory oversight). The 510(k) pathway is typically used for Class II devices and requires demonstrating substantial equivalence to a legally marketed predicate device. This means that the new device must have a similar intended use and technological characteristics as an existing FDA-approved device. Through this pathway, manufacturers can streamline approval without conducting extensive clinical trials, reducing time to market. The PMA pathway is required for Class III devices, which pose a higher risk to patients. This pathway requires comprehensive clinical testing to establish the device's safety and effectiveness, resulting in longer approval times.

Based on the information from predicate devices, the anticipated regulatory pathway for our device is 510(k) clearance, aligning with other AI-integrated imaging and radiological software solutions. Predicate devices such as AI Integrated Ultrasound, cmAngio, and CogNet QmTRIAGE have successfully gained 510(k) approval as radiological computer-assisted lesion prioritization software.[32, 33] Since the proposed solution uses A-mode ultrasound for nonpalpable lesion localization and follows a similar software-based approach, the 510(k) pathway is the most appropriate route for regulatory approval. Our device would also fall under the Class II classification because it is a moderate-risk medical device that requires regulatory controls but does not pose the high-risk level associated with Class III devices. It is designed as a radiological computer-assisted lesion localization software that aids in identifying nonpalpable breast lesions using A-mode ultrasound. Since it does not involve direct therapeutic intervention, implantable components, or life-sustaining functions, it does not meet the criteria for Class III classification.

Table 11. *Table comparing regulatory pathways of proposed solution and predicate devices.*[34]

Device	**Our solution**	**SOMO.V ABUS**	**QVCAD SYSTEM**	**cmAngio**	**CogNet QmTRIAGE**
Pathway	510(k)	PMA	PMA	510(k)	510(k)
Classification	II	III	III	II	II
Device Classification Name	radiological computer-assisted prioritization software for lesions	Automated breast ultrasound system	Analyzer, medical image	Automated radiological image processing software	radiological computer-assisted prioritization software for lesions
Type	Software	Software + physical	Software	Software	Software
Data Source	A-mode ultrasound	B-mode ultrasound	B-mode ultrasound	Mammogram	Mammogram
Application	Nonpalpable lesion localization	Breast cancer screening	Aid to reader during screening procedures by somo.v ABUS	AI-enabled software for detection of breast arterial calcification	AI to flag concerning images for further review

VII. Reimbursement

As medical devices are developed and translated into the market, it is also essential to analyze reimbursement strategies. Reimbursement for novel technologies in outpatient surgery requires consideration of the healthcare payment landscape, relevant coding pathways, and CMS processes for coverage decisions. To ensure proper payment and reimbursement for this ultrasound guidance system, three main factors must be accounted for: diagnosis and procedure coding, coverage pathways, and payment structures. Figure 16 highlights the reimbursement scheme of this specific technology.

Provider	Setting	Payment	Procedure Code	Diagnosis Code
Hospitals	Inpatient	MS-DRG + MPFS	ICD-10-PCS	ICD-10-CM
Hospitals	Outpatient	APC	CPT/HCPCS Level I	
Ambulatory Surgical Centers	Outpatient	ASC Fee Schedule		
Physicians	Outpatient (facility/office)	MPFS		
Various providers of products, services, and supplies	Outpatient	DME Fee Schedule	HCPCS Level II	

Figure 16. *Reimbursement scheme for ultrasound-guided breast lumpectomy.*

Regarding coding, both diagnostic and procedural codes must be determined. First, relevant diagnostic codes for this application focus specifically on patient cases with non-palpable breast lesions during lumpectomy, while also covering a range of breast cancer subtypes. The ICD-10-CM diagnosis codes that pertain to this application range from D05.01 to D05.21 and the specific descriptions corresponding to each code can be found in Table 12 below. Proper identification and linkage of these codes to procedure claims will ensure that payers understand the clinical significance of ultrasound-guided surgery.

Table 12. *Relevant ICD-10-CM diagnosis codes and clinical descriptions.*

ICD-10-CM Code	Description
D05.01	Lobular carcinoma in situ, non-palpable
D05.02	Ductal carcinoma in situ of breast, non-palpable
D05.10	Subareolar ductal carcinoma in situ, non-palpable
D05.11	Non-encapsulated papillary carcinoma in situ, non-palpable
D05.12	Encapsulated papillary carcinoma in situ, non-palpable
D05.20	Non-encapsulated intraductal carcinoma, non-palpable
D05.21	Encapsulated intraductal carcinoma, non-palpable

Next, the procedural codes correlating with diagnostic ultrasounds fall between CPT, or current procedural technology, codes 76506-56999. Currently, the procedure aligns most closely with the CPT 76998: Ultrasonic guidance for intraoperative procedures, imaging supervision, and interpretation. However, as this product is developed and potentially integrated with AI, new CPT coding may be warranted. For example, in 2022 CMS approved CPT 0691T, which applied to the use of AI for automated analysis of existing CT studies for vertebral fractures.[35]

The next major consideration of reimbursement is coverage pathways. There are two primary coverage frameworks: National Coverage Determination (NCD) and Local Coverage Determination (LCD). NCD applies nationally to all Medicare beneficiaries, which makes it ideal for new technologies that are seeking consistent, predictable reimbursement and a more widespread market access. Meanwhile LCDs allow for regional flexibility but can lead to inconsistent access. Thus, applying for an NCD would make more sense given the novelty of an AI-integrated ultrasound guidance system, a process involving extensive clinical data and economic analysis.

The final component is the payment structure, which is Ambulatory Payment Classifications (APC) for outpatient hospital procedures. APCs Medicare's system for paying

outpatient procedures and are bundled payment models, bundling services like imaging, surgery, and anesthesia into a single payment. Breast ultrasound procedures typically fall within APC groups 550-570 depending on case specifics.

It is also notable that integrating AI into this ultrasound guidance system may introduce additional costs, but the technology is designed to work with existing ultrasound hardware, making it more financially feasible for various medical institutions. For context, the cost of a breast ultrasound lies between $5,000-10,000 and the corresponding hospital services typically ranges from $116-607. The ultrasound used for this research is the Olympus A-scan ultrasound, which costs approximately $6,200. The Butterfly AI-integrated ultrasound, which is similar to this technology, has a probe priced at $3,899 and an annual software subscription fee of $3,500.[36]

In summary, to ensure appropriate reimbursement for the ultrasound-guided tumor localization system, the developers must address diagnosis and procedure coding, secure appropriate coverage pathways, ideally through a NCD, and align with relevant payment structures like APCs for outpatient procedures. Proper coding using ICD-10-CM and CPT codes, combined with economic feasibility and the integration of AI, supports the system's clinical value and market adoption.

VIII. Potential Market and Impact

Having demonstrated the feasibility of the proposed depth estimation algorithm under controlled simulation conditions, it is also important to consider how such a method could be translated into a real-world clinical setting. To evaluate its potential adoption, we must examine the broader healthcare landscape, particularly the oncology market where this technology would be most applicable.

It is predicted that the global healthcare market will reach USD 665.37 billion by 2028.[37] Interestingly, the U.S. spends more on health care than any other country, spending 16.9% of its Gross Domestic Product compared to the average of 8.8% in other countries.[38] To narrow the scope even further, the healthcare market specializing in oncology makes up 6% of the US market, with median per capita spending for cancer care being $584 in 2020.[33] The median per capita spending across 21 other countries was only $296. This stark contrast underscores the substantial priority placed on oncology within the US healthcare system. The oncology market is made up of several segments involving the treatment and diagnosis of various cancers. Within these segments are focuses on pharmaceuticals, drug discovery, and device design. Due to the complexity of this market, it is crucial to analyze the nature of these different segments to better address the needs of our target patients, providers, and users and to understand how our proposed product would perform in the market landscape.

The most common method for non-palpable lesion localization, wire localization, is cost effective and easily administered, but requires same day surgery and can easily dislodge. There have been several alternative devices that have entered the market, but depth limitations, high costs, and imaging incompatibilities limit the widespread use of these devices and disrupt the workflow in the operating room. In order to more comprehensively address this problem, an understanding of the market environment, target population, and potential value is crucial.

Market Landscape

Size and growth

For a more comprehensive analysis of the market landscape of breast cancer technologies, it is important to understand the narrower sphere in context of the broader cancer biotechnology market. The biotech oncology sphere as of October 2023 is made up of 5,007 companies, 17,034 deals, and 8,700 markets, meaning it is a very sizable market.[41] In terms of the

market's growth, the oncology biotech market size is predicted to increase from 220.30 Billion in 2023 to 470.61 Billion in 2032 with a compound annual growth rate (CAGR) of 8.8%.[42] In comparison, the breast cancer biotech sphere as of October 2023 is made up of 337 companies, 829 deals, 730 investors, making it a considerably smaller submarket but still one of significance.[42] In fact, the breast cancer market was valued at USD 19.8 billion in 2021 and is expected to increase to USD 49.2 billion by 2032 with a CAGR of 9.8% .[43] It is also anticipated to be the fastest-growing cancer market due to breast cancer being the most diagnosed type of cancer in 2020, making up 11.7% of new cancer cases in that year.

The trends that dominate both markets include drug discovery and pharmaceutical investments. Interestingly, a major catalyst in these markets and the healthcare industry in general is Artificial Intelligence (AI), with an expected CAGR of 37.5% from 2023 to 2030.[44] Although our solution does not directly utilize AI, it relies on automation of processes and computer science, making the AI sector an interesting parallel to our proposed solution. Furthermore, AI would be an important addition to aid in the full automation of our localization method, particularly in areas such as signal classification, parameterization, and real-time decision support.

Gaps

Figure 17 details the current devices used in non-palpable lesion localization, taking into account the cost and efficacy of each device. Efficacy was decided based on patient satisfaction, ease of use, and surgical outcomes as detailed in Banys-Paluchowski et al.[45] As mentioned, the most common method used is wire localization, which is a low cost solution but fairly inefficient due to the requirement of same day operation and patient discomfort. The other devices attempt to improve the accuracy and ease of localization and therefore are more effective, but are higher in cost.

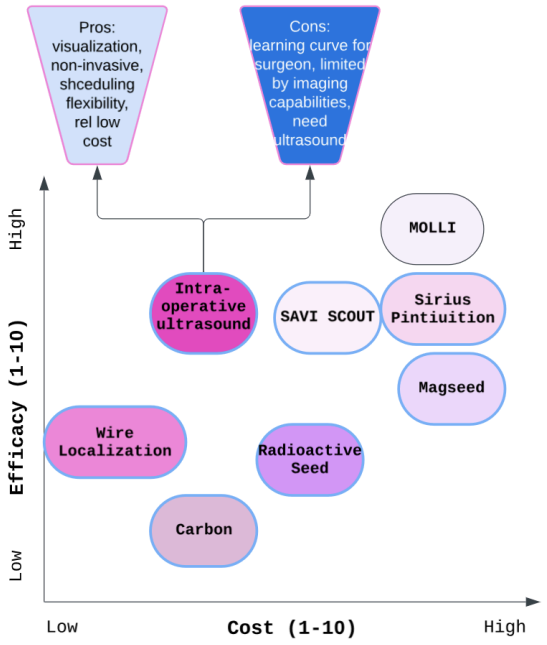

Figure 17. *A market landscape for existing solutions. Efficacy was determined by success rate and by evaluation by Dr. Fieber in clinical presentation.*

Intraoperative ultrasound (IOUS) is a treatment option that has relatively high efficacy and low cost. As detailed in Figure 17, IOUS allows for direct visualization of surgery, is noninvasive, and is compatible with sonography for localization of lesions in the operating room. IOUS is also optimal for patient comfort as it does not require additional procedures to implant devices and allows for scheduling flexibility. However, this method requires the surgeon to be experienced with breast ultrasound causing a learning curve. Overall, the market analysis of the existing methods highlights the need for more efficient, effective, and user-friendly localization tools that can enhance intraoperative decision-making without increasing procedural complexity or relying heavily on operator expertise.

Market Segmentation

Target Population

Next, it is important to consider which population our treatment would specifically target based on the usefulness and applicability of the proposed treatment. This was done by looking at the prevalence of each stage in breast cancer patients from varying demographics. It is important

to look at data across races to get a comprehensive understanding of the population of interest and to account and potentially address any variabilities. As seen in Figure 18, the most prevalent stage is localized.[46]

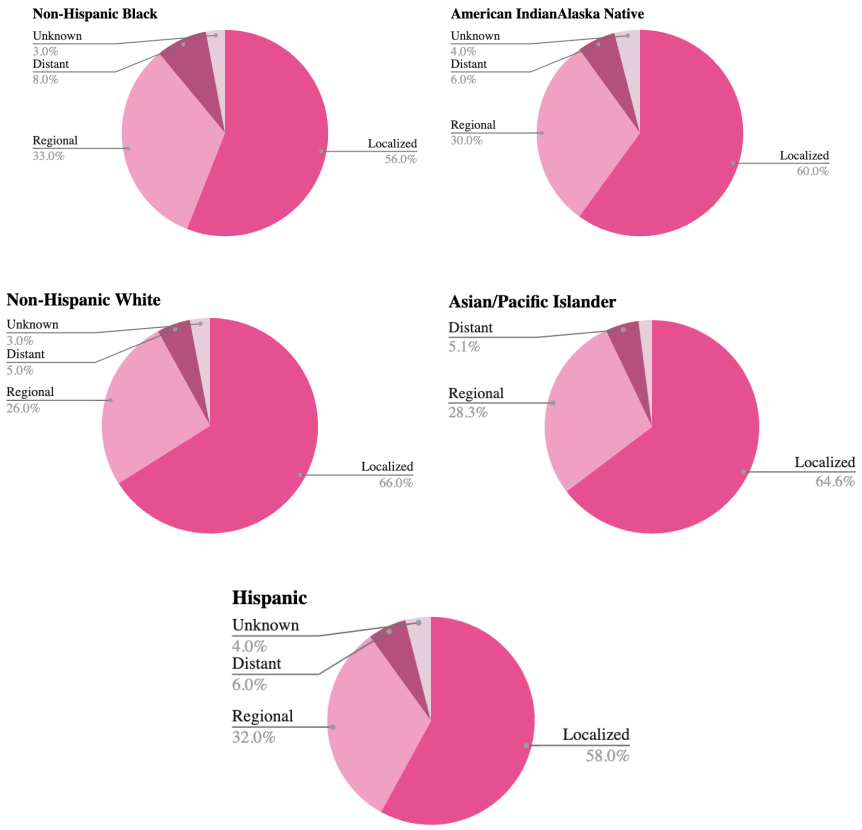

Figure 18. *Percentage of breast cancer cases by stage across varying demographics.*[47]

The next step was to look at the prevalence of non-palpable lesions and those population characteristics. Figure 18 demonstrates the narrowing of our target population to focus particularly on in situ and localized cases of breast cancer, with specific characteristics of the population being old age, post-menopause, family history of breast cancer, and small mass length.[48] This means that our target population aligns with the most prevalent and earliest stages of breast cancer as defined in Figure 18 and therefore ensures that our population is of significant size within the entire cancer and breast cancer population. Furthermore, it means that our target market should be expanded to include patients with localized breast cancers. It is also important to note that more than a third of breast cancer tumors are non-palpable at diagnosis.[38] This further

confirms the need for better localization methods as there is a high demand for this type of treatment due to the significant population and prevalence of the health problem.

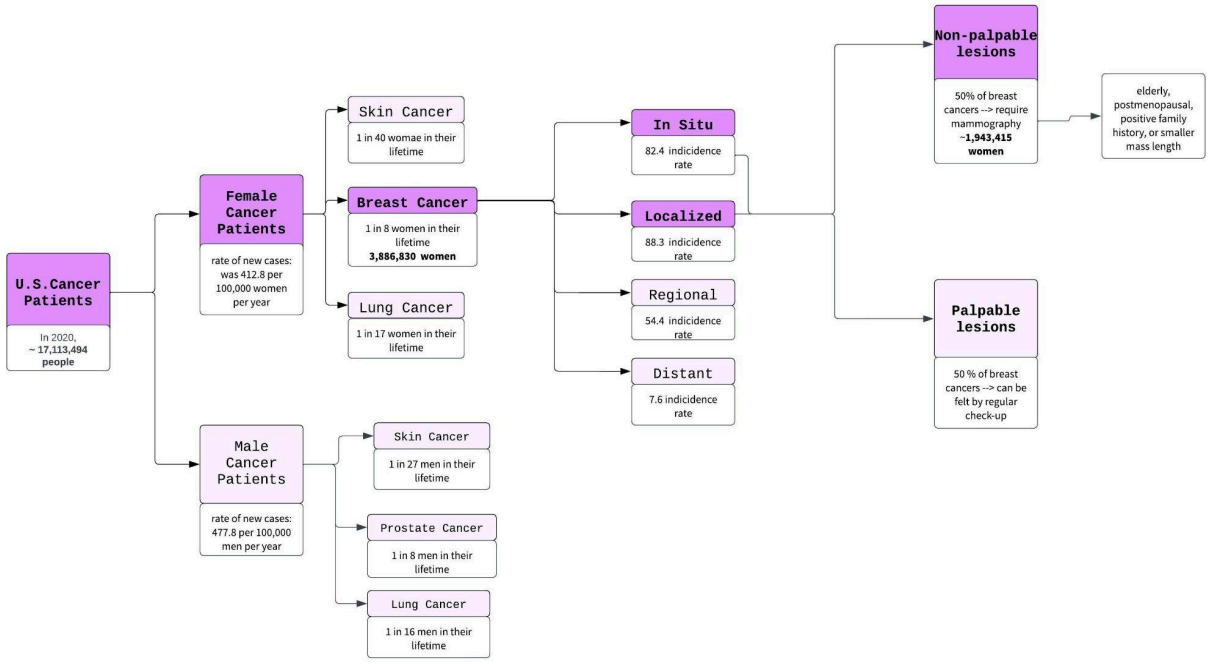

Figure 19. *Overall cancer market segmentation for target population identification. Specific focus on population most affect by non-palpable lesions within breast cancer.* [47, 48, 49]

Willingness to Pay

Next, willingness to pay of patients, customers, and investors is an important consideration as it directly impacts revenue projections and overall financial viability of the product. In this section, preferences, cost outcomes, and purchasing power are explored to understand how they will influence the viability of the product. For a patient, willingness to pay will likely be dictated by insurance coverage for the particular treatment. However, insurance coverage depends on a patient's particular plan as cancer treatment coverage varies from company to company. Assuming that the treatment is fully covered, the benefits of a particular treatment will then be considered. Benefits include non-invasiveness, comfort, and overall outcomes. Our product will hope to remain non-invasive, improve patient comfort, and improve surgical outcomes of IOUS procedures. Therefore, depending on the improved surgical outcomes and guarantee of patient comfort, the product would be a very promising option. This, however, will still be dependent on the reasonability of the price for a particular patient.

For customers, meaning hospitals, willingness to pay will be largely influenced by the actual price of the product and the resources it requires. IOUS systems rely on ultrasound technology. This would require the hospitals to invest in an ultrasound machine, which costs between $20,000 and $75,000 and typically last 5-7 years.[50] This means that the ultrasound costs between $2,857.14 and $15,000 each year but most hospitals are already likely to require this kind of technology for general day-to-day use. The software component of the product will likely add to these costs. Interestingly, the cost of an excisional biopsy is $925 while the cost of a lumpectomy is $4,302 to $9,722.[51,52] The re-operation rate of the IOUS method is 5-7%, with more than 100,000 U.S. women undergoing some form of mastectomy each year. Therefore, improvements in reoperation rate would greatly improve the customers' willingness to pay and would be a great focus for the proposed product.

For investors, willingness to play will be largely influenced by the promise and potential of the product. This would be demonstrated by the preliminary performance, proper FDA approval, and showcased commercial viability of the product. These metrics will be better quantified with prototyping and performance analysis of the product.

IX. Future Directions

While this study demonstrates the feasibility of A-mode ultrasound for tumor depth estimation in simulated models, several critical areas of development remain to advance this into a clinically applicable solution.

3D Modeling and Off-Axis Tumor Localization

The current axisymmetric Abaqus model restricts tumor placement to the central vertical axis of the breast tissue, limiting its real-world, clinical applicability. A transition to full three-dimensional finite element models will allow tumors to be located at any position within the breast volume, covering a significantly broader range of clinical cases. A transition from 2D to 3D will also enable quadrant-based localization, which is the current system used by breast radiologists and surgeons as discussed previously, and more precise surgical planning. This expansion would allow the system to not only determine tumor depth but also identify the specific region in which the tumor is located, thus improving intraoperative guidance.

Tumor Size and Morphology

In addition to expanding the range of spatial locations within the breast tissue that the model will cover, tumor size and morphology should also be varied to cover maximum clinical situations. Currently, the model accounts for tumors in the range of 5mm to 10mm. Nonpalpable breast lesions have a diameter around or less than 1cm. Thus, more simulations are required for smaller tumors in the range of 1mm-5mm to ensure that the model maintains its accuracy and low percent error as diameter decreases.

Additionally, this model idealizes the tumors as a sphere with smooth edges. However, real tumors can assume a plethora of morphologies. Benign, non-cancerous tumors are more similar to the current model and often have a round or oval shape with smooth, well-defined edges. However, malignant tumors, which are more important to identify and remove earlier, often have irregular, jagged edges with indistinct margins. Thus, simulating more complex tumor morphologies and adapting the depth calculation method based on the results is essential for clinical implementation of this system.

AI-Integration

Currently, tumor depth is calculated using manually tuned thresholds and peak detection algorithms. In order to scale this method and reduce subjectivity from the user, future development should focus on incorporating an AI algorithm to automate signal processing. The machine learning algorithm would be trained on labeled A-scan datasets with known tumor locations and properties. Once trained, it would be able to identify signal peaks of interest, adapt to noise, and distinguish true tumor reflections from surrounding tissue artifacts without manual tuning. This would allow for real-time analysis during surgical procedures and make the system more accessible to users without individual signal processing expertise.

Experimental Validation with Breast Phantoms

To move beyond simulation, validation of the ultrasound system in a physical environment is essential. The next phase of development will involve testing the system on tissue-mimicking breast phantoms that replicate the acoustic properties of breast tissue and tumors. Initial steps toward experimental validation have already been taken with the creation of agarose-based breast phantoms containing embedded tumors. Specifically, a hemispherical breast phantom, with a 40 mm radius, was created with an embedded spherical tumor, with a 10 mm diameter, placed at a depth of 20 mm. The breast phantom was created at a ratio of 1:100 agarose:DI-water to achieve a tissue density similar to that of real breast tissue, while the tumor was created at a higher density using a ratio of 2:100 agarose:DI-water. A-scan ultrasound signals were collected and analyzed, with tumor depth estimated manually within 2.6% error. These results provide proof-of-concept for transitioning from simulation to bench testing with the developed depth-calculation method. Future work will involve synthesizing a wider range of phantom geometries and material properties for generalizability. These models will allow for the systematic evaluation of localization accuracy across various tumor sizes and positions, providing real-world feedback on both the signal acquisition and processing components. This type of validation is essential for refining the algorithm in complex tumor cases and facilitating clinical translation.

Integration with Existing Ultrasound Hardware

Finally, the system will be adapted for use with existing A-scan ultrasound devices to optimize costs and implementation into current hospital workflow. This will involve interfacing the depth estimation algorithm with live ultrasound data inputs and creating a surgeon-facing output that presents actionable depth measurements. Integrating with existing hardware that is present in most ultrasound-equipped hospitals, rather than developing a new hardware device, supports the widespread adoption of this technology and improves cost-effectiveness. It also creates the potential for intraoperative use in diverse clinical settings, including outpatient clinics and low-resource areas.

References

[1]*Key Statistics for Breast Cancer*. American Cancer Society. (n.d.). https://www.cancer.org/cancer/types/breast-cancer/about/how-common-is-breast-cancer.html

[2]*What is Breast Cancer?* (2023). American Cancer Society. https://www.cancer.org/cancer/types/breast-cancer/about/what-is-breast-cancer.html

[3]*What is cancer? symptoms, signs, types & causes*. Cleveland Clinic. (n.d.-b). https://my.clevelandclinic.org/health/diseases/12194-cancer

[4]Wen, H., Xu, T., Huang, Q., Zhang, C., Zhang, Q., & Chen, H. (2020). *Nonpalpable breast masses: One-year ultrasound follow-up and morbidity outcomes in Shanghai.* Medicine, 99(50), e23556. https://doi.org/10.1097/MD.0000000000023556

[5]*Breast Cancer: Breast Needle Localization.* (2020, November 18). MyHealth.Alberta.ca https://myhealth.alberta.ca/Alberta/Pages/Breast-needle-localization.aspx

[6]*SAVI SCOUT: Cutting-Edge Technology for Breast-Conserving Surgery.* (n.d.) Penn Medicine Abramson Cancer Center. https://www.pennmedicine.org/cancer/types-of-cancer/breast-cancer/breast-cancer-treatment/lumpectomy/savi-scout

[7]New York - Presbytarian. (2022, June 7). *Needle localization*. Columbia Department of Radiology. https://www.columbiaradiology.org/patients/services/mammography-and-breast-imaging/needle-localization

[8]Mango, V., Ha, R., & Gamberawalla, A. (2016, June 15). *Evaluation of the SAVI SCOUT Surgical Guidance System for Localization and Excision of Nonpalpable Breast Lesions: A Feasibility Study*. American Journal of Roentgenology. https://www.ajronline.org/doi/10.2214/AJR.15.15962

[9]*Radioactive Seed Localization Before Breast Surgery*. (2021, January 9). Memorial Sloan Kettering Cancer Center. https://www.mskcc.org/cancer-care/patient-education/breast-seed-localization

[10]Ferreira, H. H. J., Daruich de Souza, C., & Rostelato, M. E. C. M. (2022). Radioactive Seed Localization for Conservative Surgery of Nonpalpable Breast Cancer: Recommendations for Technology Implantation Program. *International journal of surgery protocols*, 26(1), 94–106. https://doi.org/10.29337/ijsp.182

[11]*Biopsy for Breast Cancer Diagnosis: Magseed and Needle (Wire) Localization*. (n.d.). UCFS Health. https://www.ucsfhealth.org/education/biopsy-for-breast-cancer-diagnosis-magseed-wire-localization-biopsy

[12]*Magseed - Precise Breast Cancer Localization*. (n.d.). Endomagnetics Ltd. https://www.endomag.com/products/magseed/

[13]Hu X, Li S, Jiang Y, et al. Intraoperative ultrasound-guided lumpectomy versus wire-guided excision for nonpalpable breast cancer. Journal of International Medical Research. 2020;48(1). Doi:10.1177/0300060519896707

[14]Norton, L. W., Zeligman, B. E., & Pearlman, N. W. (1988). Accuracy and cost of needle localization breast biopsy. Archives of surgery (Chicago, Ill. : 1960), 123(8), 947–950. https://doi.org/10.1001/archsurg.1988.01400320033005

[15]Garzotto, F., Comoretto, R., & Michieletto, S. (2021, April 22). *Preoperative non-palpable breast lesion localization, innovative techniques and clinical outcomes in Surgical Practice: A systematic review and meta-analysis*. ScienceDirect. https://www.sciencedirect.com/science/article/pii/S0960977621003660

[16]Murphy, J. O., Moo, T. A., King, T. A., Van Zee, K. J., Villegas, K. A., Stempel, M., Eaton, A., St Germain, J. M., Morris, E., & Morrow, M. (2013). Radioactive seed localization compared to wire localization in breast-conserving surgery: initial 6-month experience. *Annals of surgical oncology*, 20(13), 4121–4127. https://doi.org/10.1245/s10434-013-3166-4

[17]Tingen, J. S., McKinley, B. P., Rinkliff, J. M., Cornett, W. R., & Lucas, C. (2020). Savi Scout Radar Localization Versus Wire Localization for Breast Biopsy Regarding Positive Margin, Complication, and Reoperation Rates. *The American surgeon*, 86(8), 1029–1031. https://doi.org/10.1177/0003134820939903

[18]*Scout® radar localization*. Merit Medical. (2023, June 21). https://www.merit.com/merit-oncology/localization/breast-soft-tissue-localization/scout-radar-localization/

[19]Breast cancer outcomes. Winship Cancer Institute of Emory University. (n.d.). https://winshipcancer.emory.edu/cancer-types-and-treatments/breast-cancer/outcomes.php#:~:text=One%20of%20the%20first%20questions,for%20early%2Dstage%20breast%20cancers.

[20]Mammogram procedure. Johns Hopkins Medicine. (2024, September 9). https://www.hopkinsmedicine.org/health/treatment-tests-and-therapies/mammogram-procedu

[21]What is a breast mri?: Breast cancer screening. What Is a Breast MRI? | Breast Cancer Screening | American Cancer Society. (n.d.). https://www.cancer.org/cancer/types/breast-cancer/screening-tests-and-early-detection/breast-mri-scans.html

[22]Breast mri. Breast MRI - Siemens Healthineers. (n.d.). https://www.siemens-healthineers.com/magnetic-resonance-imaging/clinical-specialities/breast-mri

[23]Breast Ultrasound. Johns Hopkins Medicine. (2024a, July 25). https://www.hopkinsmedicine.org/health/treatment-tests-and-therapies/breast-ultrasound

[24]What is a breast ultrasound?: Breast cancer screening. What Is a Breast Ultrasound? | Breast Cancer Screening | American Cancer Society. (n.d.). https://www.cancer.org/cancer/types/breast-cancer/screening-tests-and-early-detection/breast-ultrasound.html

[25]Nicosia, L., Pesapane, F., Bozzini, A. C., Latronico, A., Rotili, A., Ferrari, F., Signorelli, G., Raimondi, S., Vignati, S., Gaeta, A., Bellerba, F., Origgi, D., De Marco, P., Castiglione Minischetti, G., Sangalli, C., Montesano, M., Palma, S., & Cassano, E. (2023b, February 2). Prediction of the malignancy of a breast lesion detected on breast ultrasound: Radiomics applied to clinical practice. MDPI. https://www.mdpi.com/2072-6694/15/3/964

[26]*Ultrasound physics and technical facts for the beginner*. ACEP Symbol. (n.d.). https://www.acep.org/sonoguide/basic/ultrasound-physics-and-technical-facts-for-the-beginner#:~:text=These%20occur%20as%20sound%20waves,ultrasound%20waves)%20and%20vice%20versa

[27]Basic physical principles of ultrasound. (n.d.). https://dccam.com.au/lcmc2018/pdf/6._Basic_Principles_of_Ultrasound.pdf

[28]Themes, U. (2016, August 11). Principles of Ultrasound. Radiology Key. https://radiologykey.com/principles-of-ultrasound/

[29]Li, C., Duric, N., Littrup, P., & Huang, L. (2009). In vivo breast sound-speed imaging with ultrasound tomography. *Ultrasound in Medicine & Biology*, *35*(10), 1615–1628. https://doi.org/10.1016/j.ultrasmedbio.2009.05.011

[30]Abulencia, F. D. (2021). A Method for Detection and Characterization of Breast Tumors using Ultrasound with CNN (thesis).

[31]Center for Devices and Radiological Health. (n.d.). Premarket notification 510(K). U.S. Food and Drug Administration. https://www.fda.gov/medical-devices/premarket-submissions-selecting-and-preparing-correct-submission/premarket-notification-510k

[32]CmAngio®. CureMetrix. (2023, October 13). https://curemetrix.com/cmangio/

[33]Alicia V. Nieva-Woodgate, A. N. (2022, December 14). U.S. FDA clears MedCognetics' AI Enabled Breast Cancer Screening Software. Global Press Release & Newswire Distribution Services. https://www.businesswire.com/news/home/20221214005432/en/U.S.-FDA-Clears-MedCognetics%E2%80%99-AI-Enabled-Breast-Cancer-Screening-Software

[34]Commissioner, O. of the. (n.d.). U.S. Food and Drug Administration. https://www.fda.gov/

[35]Ridley, E. L. (2021, July 23). New CPT code for Radiology AI brings hope, but patience is needed. AuntMinnie. https://www.auntminnie.com/imaging-informatics/artificial-intelligence/article/15628838/new-cpt-code-for-radiology-ai-brings-hope-but-patience-is-needed

[36]Bringing the power of ultrasound into your assessment, diagnosis and treatment. Butterfly. (n.d.). https://www.butterflynetwork.com/

[37]Intelligence, I. (2023, January 1). *US healthcare industry 2023: Sectors, Trends & Statistics*. Insider Intelligence. https://www.insiderintelligence.com/insights/healthcare-industry/

[38]*U.S. health care from a global perspective, 2019: Higher spending, worse outcomes?*. U.S. Health Care from a Global Perspective, 2019 | Commonwealth Fund. (2020, January 30). https://www.commonwealthfund.org/publications/issue-briefs/2020/jan/us-health-care-global-perspective-2019

[39]Chow, R. D., Bradley, E. H., & Gross, C. P. (2022). Comparison of cancer-related spending and mortality rates in the US vs 21 high-income countries. *JAMA Health Forum*, *3*(5). https://doi.org/10.1001/jamahealthforum.2022.1229

[40]PitchBook. (n.d.). Cancer Biotechnology Industry Profile. PitchBook. Retrieved October 16, 2023 from https://www.pitchbook.com

[41]*Oncology market (by Cancer Diagnostics & Treatment: Cancer Diagnostics and cancer treatment; by indication: Lungs cancer, colorectal cancer, breast cancer, liver cancer, bladder cancer, Head & Neck Cancer, prostate cancer, and others) - global industry analysis, size, share, growth, trends, regional outlook, and forecast 2023 – 2032*. Precedence Research. (n.d.). https://www.precedenceresearch.com/oncology-market#:~:text=The%20cancer%20diagnostic%20segment%20has,total%20market%20share%20in%202021.

[42]PitchBook. (n.d.). Breast Cancer Biotechnology Industry Profile. PitchBook. Retrieved October 16, 2023 from https://www.pitchbook.com

[43]*Breast cancer market (by therapy: Targeted therapy, hormonal therapy, surgery and radiation therapy, biologic therapy; by cancer type: Hormone receptor, HER2+; by distribution channel: Hospital Pharmacies, retail pharmacies, online pharmacies, others) - global industry analysis, size, share, growth, trends, regional outlook, and forecast 2023-2032*. Precedence Research. (n.d.-a). https://www.precedenceresearch.com/breast-cancer-market

[44]*Artificial Intelligence in healthcare market size report, 2030*. Artificial Intelligence In Healthcare Market Size Report, 2030. (n.d.). https://www.grandviewresearch.com/industry-analysis/artificial-intelligence-ai-healthcare-market

[45]Banys-Paluchowski, M., Kühn, T., Masannat, Y., Rubio, I., de Boniface, J., Ditsch, N., Karadeniz Cakmak, G., Karakatsanis, A., Dave, R., Hahn, M., Potter, S., Kothari, A., Gentilini, O. D., Gulluoglu, B. M., Lux, M. P., Smidt, M., Weber, W. P., Aktas Sezen, B., Krawczyk, N., … Harvey, J. (2023). Localization techniques for non-palpable breast lesions: Current status, knowledge gaps, and rationale for the Melody Study (EUBREAST-4/ibra-net, NCT 05559411). *Cancers*, *15*(4), 1173. https://doi.org/10.3390/cancers15041173

[46]*Cancer facts & figures 2023*. American Cancer Society. (n.d.). https://www.cancer.org/research/cancer-facts-statistics/all-cancer-facts-figures/2023-cancer-facts-figures.html

[47]Chang, H. R., Cole, B., & Bland, K. I. (1997). Nonpalpable breast cancer in women aged 40-49 years: A surgeon's view of benefits from Screening Mammography. JNCI Monographs, 1997(22), 145–149. https://doi.org/10.1093/jncimono/1997.22.145

[48]*Breast cancer statistics: How common is breast cancer?*. Breast Cancer Statistics | How Common Is Breast Cancer? | American Cancer Society. (n.d.). https://www.cancer.org/cancer/types/breast-cancer/about/how-common-is-breast-cancer.html#:~:text=It%20is%20about%2030%25%20(or,(DCIS)%20will%20be%20diagnosed.

[49]*Breast cancer statistics: World cancer research fund international*. WCRF International. (2022, April 14). https://www.wcrf.org/cancer-trends/breast-cancer-statistics/

[50]Karen. (2022, August 24). *How much does an ultrasound machine cost - 11 factors to consider*. Ultrasound Solutions Corp. https://www.uscultrasound.com/ultrasound-machine-cost/#:~:text=Depending%20on%20the%20level%20of,%2440%2C000%20for%20an%20average%20model.

[51]Imaging of the pubic symphysis: Anatomy and pathologic conditions. (n.d.). https://pubs.rsna.org/doi/10.1148/rg.220058

[52]Mdsave.com. (n.d.). https://www.mdsave.com/procedures/partial-mastectomy-lumpectomy/d78af4c5

[53]Niu, S., & Srivastava, V. (2022). Ultrasound classification of interacting flaws using finite element simulations and convolutional neural network. *Engineering with Computers*, *38*(5), 4653–4662. https://doi.org/10.1007/s00366-022-01681-y

Appendix A: Parameters for Depth Calculation from Signal

*Second peak was chosen, ** third peak was chosen, *** > third peak was chosen.

Table A1. *Parameters for 10 mm tumor signal analysis.*

Simulation	Dip Height	Dip Threshold	Peak Height	Peak Threshold
+12.5	-0.5	10000	0.5	10000
+10	-0.5	10000	0.5	10000
+7.5	-0.5	10000	0.5	10000
+5	-0.5	10000	0.5	10000
+2.5	-0.5	10000	0.5	10000
0	-0.5	10000	0.5	10000
-2.5	-0.5	10000 *	0.5	10000*
-5	-0.5	10000 *	0.5	10000 *
-7.5	-0.5	10000 *	0.5	10000*
-10	-0.5	10000 *	0.5	10000 *
-12.5	-0.5	10000 *	0.5	10000 *

Table A2. *Parameters for 7.5 mm tumor signal analysis.*

Simulation	Dip Height	Dip Threshold	Peak Height	Peak Threshold
+12.5	-0.4	1000	0.4	3000
+10	-0.4	1000	0.4	3000
+7.5	-0.4	10000	0.65	1000
+5	-0.4	1000	0.65	1000
+2.5	-0.4	10000	0.5	10000
0	-0.5	10000	0.5	10000
-2.5	-0.5	1000 *	0.5	10000
-5	-0.53	10000	0.5	10000 *
-7.5	-0.5	10000	0.5	10000
-10	-0.54	10000 *	0.5	10000 *
-12.5	-0.54	10000 *	0.5	10000 *

Table A3. *Parameters for 6 mm tumor signal analysis.*

Simulation	Dip Height	Dip Threshold	Peak Height	Peak Threshold
+12.5	-0.3	1000	0.5	1000
+10	-0.3	1000	0.5	1000
+7.5	-0.4	1000	0.5	1000 *
+5	-0.3	1000	0.5	1000
+2.5	-0.4	10000	0.5	1000
0	-0.515	10000 ***	0.54	1000 **
-2.5	-0.45	25000 *	0.5	10000*
-5	-0.5	10000 *	0.5	10000*
-7.5	-0.5	10000 *	0.55	7500*
-10	-0.5	10000	0.5	10000*
-12.5	-0.51	10000 *	0.51	10000 *

Table A4. *Parameters for 5 mm tumor signal analysis.*

Simulation	Dip Height	Dip Threshold	Peak Height	Peak Threshold
+12.5	-0.4	1000	0.5	1000
+10	-0.35	1000	0.5	1000
+7.5	-0.3	1000	0.46	1000
+5	-0.3	1000	0.46	1000
+2.5	-0.4	1000	0.46	1000
0	-0.42	1000 *	0.476	1000 **
-2.5	-0.4	1000	0.5	1000
-5	-0.38	1000	0.5	1000
-7.5	-0.4	1000	0.5	10000
-10	-0.3	100	0.51	100
-12.5	-0.4	100	0.6	1000

Appendix B: Abaqus Code

This code was adapted from Francesca Denise Abulencia's code from her thesis entitled A Method for Detection and Characterization of Breast Tumors using Ultrasound with CNN. The code was adapted to account for varying tumor radii and depths.

```
import csv
import random
import math
import numpy as np
from part import *
from material import *
from section import *
from assembly import *
from step import *
from interaction import *
from load import *
from mesh import *
from optimization import *
from job import *
from sketch import *
from visualization import *
from connectorBehavior import *



# Set the flag to True if odb is not needed
remove_odb = False
failure_flag = 0
trial_index = 0
# Change this to desired file path
features_filepath = ‘’
# Change based on how many sims you want to run
```

```
num_sims = 5
# Open text files for writing
features_file = open(features_filepath, 'w')
with open(features_filepath, 'w', newline='') as features_file:
    features_writer = csv.writer(features_file)
    # Write headers for the features CSV
    features_writer.writerow([f'Simulation_{i + 1}' for i in range(num_sims)])
    # List to store failed simulation info
    failed_mesh = []
    failed_earlystop = []
    ##### Breast Parameters (FIXED) #####
    breast_radius = 0.040 # in m
    E_breast = 0.02*(10**6)    # Pascal
    v_breast = 0.4999985
    p_breast = 1000   #1032
    ##### Mesh calculations #####
    K = E_breast/(3*(1-2*v_breast))
    c = np.sqrt(K/p_breast)
    f = 1*1000000 # Frequency in Hz
    lambda_ = c/f
    mesh_low = lambda_/10
    mesh_high = lambda_/15
    ##### Transducer Partition Calculation (Edge) for RF-P #####
    # Probe Parameters
    probe_radius = 0.012 # in m
    s = probe_radius/2
    theta = s/breast_radius # in radians
    x_coord_probe = 0.040*math.tan(theta)  # in m
    y_coord_probe = 0.040*math.cos(theta)  # in m
    ##### Specify Range to Vary Tumor Parameters #####
    E_tumor = 2.0*(10**6)
```

```
tumorSize = 0.0075
tumorDensity = 1040
# Change based on desired depth
tumor_positions = [0.0025, 0.005, 0.0075, 0.01, 0.0125]
random.seed(42)
total_time = 0.00007
time_increment = 2e-09   #user-fixed time increment
sampling_number = total_time / time_increment
c_fixed = 1480 m/s # in literature value for breast tissue
current_index = 1
##### Specify Time Parameters #####
while current_index <= num_sims:
    p_tumor = 1040
    E_tumor = 20*(10**6)
    v_tumor = ((-E_tumor/(3*p_tumor*c_fixed*c_fixed))+1)/2
    tumorSize = [0.005, 0.0075, 0.008]
    tumorSize_radius = tumorSize/2
    ##### Creates Breast Part #####
    mdb.models['Model-1'].ConstrainedSketch(name='__profile__', sheetSize=1.0)
    mdb.models['Model-1'].sketches['__profile__'].sketchOptions.setValues(
        viewStyle=AXISYM)
    mdb.models['Model-1'].sketches['__profile__'].ConstructionLine(point1=(0.0,
        -0.5), point2=(0.0, 0.5))
    mdb.models['Model-1'].sketches['__profile__'].FixedConstraint(entity=
        mdb.models['Model-1'].sketches['__profile__'].geometry[2])
    mdb.models['Model-1'].sketches['__profile__'].CircleByCenterPerimeter(center=(
        0.0, 0.0), point1=(0.04, 0.0))
    mdb.models['Model-1'].sketches['__profile__'].Line(point1=(0.0, 0.0), point2=(
        0.0, 0.04))
    mdb.models['Model-1'].sketches['__profile__'].VerticalConstraint(addUndoState=
        False, entity=mdb.models['Model-1'].sketches['__profile__'].geometry[4])
```

```
mdb.models['Model-1'].sketches['__profile__'].Line(point1=(0.0, 0.0), point2=(
    0.04, 0.0))
mdb.models['Model-1'].sketches['__profile__'].HorizontalConstraint(
    addUndoState=False, entity=
    mdb.models['Model-1'].sketches['__profile__'].geometry[5])
mdb.models['Model-1'].sketches['__profile__'].autoTrimCurve(curve1=
    mdb.models['Model-1'].sketches['__profile__'].geometry[3], point1=(
    -0.0369940288364887, 0.0143605135381222))
mdb.models['Model-1'].sketches['__profile__'].autoTrimCurve(curve1=
    mdb.models['Model-1'].sketches['__profile__'].geometry[7], point1=(
    0.0335051640868187, -0.0218111537396908)
mdb.models['Model-1'].Part(dimensionality=AXISYMMETRIC, name='Part-1', type=
    DEFORMABLE_BODY)
mdb.models['Model-1'].parts['Part-1'].BaseShell(sketch=
    mdb.models['Model-1'].sketches['__profile__'])
del mdb.models['Model-1'].sketches['__profile__']
mdb.models['Model-1'].Material(name='Breast')
##### Specify Material Parameters #####
mdb.models['Model-1'].materials['Breast'].Density(table=((p_breast, ), ))
mdb.models['Model-1'].materials['Breast'].Elastic(table=((E_breast, v_breast),
    ))
mdb.models['Model-1'].Material(name='Tumor')
mdb.models['Model-1'].materials['Tumor'].Density(table=((p_tumor, ), ))
mdb.models['Model-1'].materials['Tumor'].Elastic(table=((E_tumor, v_tumor),
    ))
mdb.models['Model-1'].ConstrainedSketch(gridSpacing=0.002, name='__profile__',
sheetSize=0.113, transform=
mdb.models['Model-1'].parts['Part-1'].MakeSketchTransform(
sketchPlane=mdb.models['Model-1'].parts['Part-1'].faces[0],
sketchPlaneSide=SIDE1, sketchOrientation=RIGHT, origin=(0.016977, 0.016977,
0.0)))
```

```
    mdb.models['Model-1'].sketches['__profile__'].sketchOptions.setValues(
        decimalPlaces=3)
    mdb.models['Model-1'].parts['Part-1'].projectReferencesOntoSketch(filter=
        COPLANAR_EDGES, sketch=mdb.models['Model-1'].sketches['__profile__'])
    del mdb.models['Model-1'].sketches['__profile__']
    mdb.models['Model-1'].ConstrainedSketch(gridSpacing=0.002, name='__profile__',
        sheetSize=0.113, transform=
        mdb.models['Model-1'].parts['Part-1'].MakeSketchTransform(
        sketchPlane=mdb.models['Model-1'].parts['Part-1'].faces[0],
        sketchPlaneSide=SIDE1, sketchOrientation=RIGHT, origin=(0.016977, 0.016977,
        0.0)))
    mdb.models['Model-1'].sketches['__profile__'].sketchOptions.setValues(
        decimalPlaces=3)
    ##### Sketch Tumor by Specifying Radius #####geometry
    # Change based on if you want above or below center
    mdb.models['Model-1'].parts['Part-1'].projectReferencesOntoSketch(filter=
        COPLANAR_EDGES, sketch=mdb.models['Model-1'].sketches['__profile__'])
    mdb.models['Model-1'].sketches['__profile__'].CircleByCenterPerimeter(center=(
                        -0.016977,  0.003023+tumor_positions[current_index-1]),  point1=(-0.017,
(0.003023+tumor_positions[current_index-1]+tumorSize_radius[current_index-1])))
    mdb.models['Model-1'].sketches['__profile__'].CoincidentConstraint(
        addUndoState=False, entity1=
        mdb.models['Model-1'].sketches['__profile__'].vertices[3], entity2=
        mdb.models['Model-1'].sketches['__profile__'].geometry[4])
            mdb.models['Model-1'].sketches['__profile__'].autoTrimCurve(curve1=
        mdb.models['Model-1'].sketches['__profile__'].geometry[6], point1=(
        -0.0214893044401407, 0.00461527430820465))
    mdb.models['Model-1'].parts['Part-1'].PartitionFaceBySketch(faces=
        mdb.models['Model-1'].parts['Part-1'].faces.getSequenceFromMask(('[#1 ]',
        ), ), sketch=mdb.models['Model-1'].sketches['__profile__'])
    del mdb.models['Model-1'].sketches['__profile__']
```

```
mdb.models['Model-1'].HomogeneousSolidSection(material='Breast', name=
    'Section-1-Breast', thickness=None)
mdb.models['Model-1'].HomogeneousSolidSection(material='Tumor', name=
    'Section-2-Tumor', thickness=None)
mdb.models['Model-1'].parts['Part-1'].SectionAssignment(offset=0.0,
    offsetField='', offsetType=MIDDLE_SURFACE, region=Region(
    faces=mdb.models['Model-1'].parts['Part-1'].faces.getSequenceFromMask(
    mask=('[#1 ]', ), )), sectionName='Section-1-Breast', thicknessAssignment=
    FROM_SECTION)
mdb.models['Model-1'].parts['Part-1'].SectionAssignment(offset=0,
    offsetField='', offsetType=MIDDLE_SURFACE, region=Region(
    faces=mdb.models['Model-1'].parts['Part-1'].faces.getSequenceFromMask(
    mask=('[#2 ]', ), )), sectionName='Section-2-Tumor', thicknessAssignment=
    FROM_SECTION)
##### Assembly #####
mdb.models['Model-1'].rootAssembly.DatumCsysByThreePoints(coordSysType=
    CYLINDRICAL, origin=(0.0, 0.0, 0.0), point1=(1.0, 0.0, 0.0), point2=(0.0,
    0.0, -1.0))
mdb.models['Model-1'].rootAssembly.Instance(dependent=OFF, name='Part-1-1',
part=mdb.models['Model-1'].parts['Part-1'])
mdb.models['Model-1'].rootAssembly.ReferencePoint(point=(x_coord_probe,
y_coord_probe, 0.0))
mdb.models['Model-1'].rootAssembly.PartitionEdgeByParam(edges=
mdb.models['Model-1'].rootAssembly.instances['Part-1-1'].edges.getSequenceFromMask(
('[#8 ]', ), ), parameter=0.903419530020852)
mdb.models['Model-1'].rootAssembly.Set(edges=
    mdb.models['Model-1'].rootAssembly.instances['Part-1-1'].edges.getSequenceFromMask(
    ('[#10 ]', ), ), name='PROBE')
mdb.models['Model-1'].rootAssembly.Surface(name='PROBE-SURF', side1Edges=
    mdb.models['Model-1'].rootAssembly.instances['Part-1-1'].edges.getSequenceFromMask(
    ('[#10 ]', ), ))
```

```
    mdb.models['Model-1'].rootAssembly.PartitionEdgeByPoint(edge=
        mdb.models['Model-1'].rootAssembly.instances['Part-1-1'].edges[4], point=
        mdb.models['Model-1'].rootAssembly.instances['Part-1-1'].InterestingPoint(
        mdb.models['Model-1'].rootAssembly.instances['Part-1-1'].edges[4], MIDDLE))
    mdb.models['Model-1'].rootAssembly.Set(edges=
        mdb.models['Model-1'].rootAssembly.instances['Part-1-1'].edges.getSequenceFromMask(
        ('[#20 ]', ), ), name='SENSOR')
    ##### Step #####
    mdb.models['Model-1'].ExplicitDynamicsStep(name='Step-1',
    previous='Initial', timeIncrementationMethod=FIXED_USER_DEFINED_INC,
    timePeriod=total_time, userDefinedInc=time_increment)
    ##### History Output Request (U2) #####
    mdb.models['Model-1'].HistoryOutputRequest(createStepName='Step-1', frequency=1
    , name='H-Output-2', rebar=EXCLUDE, region=
    mdb.models['Model-1'].rootAssembly.sets['SENSOR'], sectionPoints=DEFAULT,
    variables=('U2', ))
    ##### Displacement Boundary Condition #####
    mdb.models['Model-1'].DisplacementBC(amplitude=UNSET, createStepName='Step-1',
    distributionType=UNIFORM, fieldName='', fixed=OFF, localCsys=None, name=
    'BC-1', region=Region(

edges=mdb.models['Model-1'].rootAssembly.instances['Part-1-1'].edges.getSequenceFromMask(
    mask=('[#4 ]', ), )), u1=0.0, u2=0.0, ur3=0.0)
    mdb.models['Model-1'].DisplacementBC(amplitude=UNSET, createStepName='Step-1',
    distributionType=UNIFORM, fieldName='', fixed=OFF, localCsys=None, name=
    'BC-2', region=Region(

edges=mdb.models['Model-1'].rootAssembly.instances['Part-1-1'].edges.getSequenceFromMask(
    mask=('[#c2 ]', ), )), u1=0.0, u2=UNSET, ur3=UNSET)
    mdb.models['Model-1'].TabularAmplitude(data=((3e-08, 0.00193832), (6e-08,
    0.007331565), (9e-08, 0.014955369), (1.2e-07, 0.02290189), (1.5e-07,
```

0.028768258), (1.8e-07, 0.029899718), (2.1e-07, 0.02366855), (2.4e-07, 0.007766768), (2.7e-07, -0.019510884), (3e-07, -0.059016994), (3.3e-07, -0.110556088), (3.6e-07, -0.172761899), (3.9e-07, -0.243060632), (4.2e-07, -0.31772778), (4.5e-07, -0.392039522), (4.8e-07, -0.460513061), (5.1e-07, -0.517223685), (5.4e-07, -0.556180509), (5.7e-07, -0.571737999), (6e-07, -0.559016994), (6.3e-07, -0.514307163), (6.6e-07, -0.435422866), (6.9e-07, -0.321986312), (7.2e-07, -0.175615544), (7.5e-07, -1.84e-16), (7.8e-07, 0.199147085), (8.1e-07, 0.414262793), (8.4e-07, 0.636230724), (8.7e-07, 0.854787048), (9e-07, 1.059016994), (9.3e-07, 1.237916106), (9.6e-07, 1.380985813), (9.9e-07, 1.478829772), (1.02e-06, 1.523716342), (1.05e-06, 1.510073511), (1.08e-06, 1.43488558), (1.11e-06, 1.297965853), (1.14e-06, 1.102086081), (1.17e-06, 0.85295126), (1.2e-06, 0.559016994), (1.23e-06, 0.231155583), (1.26e-06, -0.117814271), (1.29e-06, -0.473711225), (1.32e-06, -0.821658865), (1.35e-06, -1.146802247), (1.38e-06, -1.435035365), (1.41e-06, -1.673700482), (1.44e-06, -1.852221406), (1.47e-06, -1.962636182), (1.5e-06, -2.0), (1.53e-06, -1.962636182), (1.56e-06, -1.852221406), (1.59e-06, -1.673700482), (1.62e-06, -1.435035365), (1.65e-06, -1.146802247), (1.68e-06, -0.821658865), (1.71e-06, -0.473711225), (1.74e-06, -0.117814271), (1.77e-06, 0.231155583), (1.8e-06, 0.559016994), (1.83e-06, 0.85295126), (1.86e-06, 1.102086081), (1.89e-06, 1.297965853), (1.92e-06, 1.43488558), (1.95e-06, 1.510073511), (1.98e-06, 1.523716342), (2.01e-06, 1.478829772), (2.04e-06, 1.380985813), (2.07e-06, 1.237916106), (2.1e-06, 1.059016994), (2.13e-06, 0.854787048), (2.16e-06, 0.636230724), (2.19e-06, 0.414262793), (2.22e-06, 0.199147085), (2.25e-06, 5.51e-16), (2.28e-06, -0.175615544), (2.31e-06, -0.321986312), (2.34e-06, -0.435422866), (2.37e-06, -0.514307163), (2.4e-06, -0.559016994), (2.43e-06, -0.571737999), (2.46e-06, -0.556180509), (2.49e-06, -0.517223685), (2.52e-06, -0.460513061), (2.55e-06, -0.392039522), (2.58e-06, -0.31772778), (2.61e-06, -0.243060632), (2.64e-06, -0.172761899), (2.67e-06, -0.110556088), (2.7e-06, -0.059016994), (2.73e-06, -0.019510884), (2.76e-06, 0.007766768), (2.79e-06, 0.02366855), (2.82e-06,

```
    0.029899718), (2.85e-06, 0.028768258), (2.88e-06, 0.02290189), (2.91e-06,
    0.014955369), (2.94e-06, 0.007331565), (2.97e-06, 0.00193832), (3e-06,
    0.0)), name='Amp-1', smooth=SOLVER_DEFAULT, timeSpan=STEP)
    mdb.models['Model-1'].Pressure(amplitude='Amp-1', createStepName='Step-1',
        distributionType=UNIFORM, field='', magnitude=1000000.0, name='OneMHz',
        region=mdb.models['Model-1'].rootAssembly.surfaces['PROBE-SURF'])
    mdb.models['Model-1'].rootAssembly.seedEdgeBySize(constraint=FINER,
        deviationFactor=0.1, edges=
        mdb.models['Model-1'].rootAssembly.instances['Part-1-1'].edges.getSequenceFromMask(
        ('[#ff ]', ), ), size=mesh_low)
    mdb.models['Model-1'].rootAssembly.setMeshControls(regions=
        mdb.models['Model-1'].rootAssembly.instances['Part-1-1'].faces.getSequenceFromMask(
        ('[#1 ]', ), ), technique=STRUCTURED)
    mdb.models['Model-1'].rootAssembly.PartitionFaceByAuto(face=
        mdb.models['Model-1'].rootAssembly.instances['Part-1-1'].faces[1])
    mdb.models['Model-1'].rootAssembly.PartitionFaceByAuto(face=
        mdb.models['Model-1'].rootAssembly.instances['Part-1-1'].faces[1])
    mdb.models['Model-1'].rootAssembly.setMeshControls(elemShape=QUAD, regions=
        mdb.models['Model-1'].rootAssembly.instances['Part-1-1'].faces.getSequenceFromMask(
        ('[#f ]', ), ), technique=STRUCTURED)
    mdb.models['Model-1'].rootAssembly.generateMesh(regions=(
        mdb.models['Model-1'].rootAssembly.instances['Part-1-1'], ))
    mdb.Job(activateLoadBalancing=False, atTime=None, contactPrint=OFF,
        description='', echoPrint=OFF, explicitPrecision=DOUBLE, historyPrint=OFF,
        memory=90, memoryUnits=PERCENTAGE, model='Model-1', modelPrint=OFF,
            multiprocessingMode=DEFAULT,  name='Breast_Simulation_'+str(current_index),
nodalOutputPrecision=FULL,
        numCpus=1, numDomains=1, parallelizationMethodExplicit=DOMAIN, queue=None,
        resultsFormat=ODB, scratch='', type=ANALYSIS, userSubroutine='', waitHours=
        0, waitMinutes=0)
    mdb.jobs['Breast_Simulation_'+str(current_index)].submit(consistencyChecking=OFF)
```

```
    mdb.jobs['Breast_Simulation_'+str(current_index)].waitForCompletion()
    ##### Open ODB file after the job is finished #####
    Odb_path = 'Breast_Simulation_'+str(current_index)+'.odb'
    odb = openOdb(Odb_path)
    step = 'Step-1'
    # Open history steps data
    step1 = odb.steps[step]
    # Use a loop to get the  data of all the sensor nodes
    set_sensor = odb.rootAssembly.nodeSets['SENSOR'].nodes[0]
    try:
       region = step1.historyRegions['Node PART-1-1.' + str(set_sensor[0].label)]
    except KeyError:
       odb.close()
       failure_flag = 1
       failed_mesh.append(current_index)
       pass
    else:
       time, U2_total = zip(
                                                  *step1.historyRegions['Node    PART-1-1.'   +
str(set_sensor[0].label)].historyOutputs['U2'].data)
       for i in range(1, len(set_sensor)):
          time, U2 = zip(
                                                  *step1.historyRegions['Node    PART-1-1.'   +
str(set_sensor[i].label)].historyOutputs['U2'].data)
          U2_total = [a + b for a, b in zip(U2_total, U2)]
       U2_ave = [a / len(set_sensor) for a in U2_total]
       nn = len(U2_ave)
       simulation_data = [f'Simulation {current_index}'] + U2_ave
       features_writer.writerow(simulation_data)
       odb.close()
       failure_flag = 0
```

```
try:
   os.remove('Breast_Simulation_'+str(current_index)+'.abq')
except WindowsError:
   pass
# try:
#    os.remove('Breast_Simulation_'+str(current_index)+'.inp')
except WindowsError:
   pass
try:
   os.remove('Breast_Simulation_'+str(current_index)+'.ipm')
except WindowsError:
   pass
try:
   os.remove('Breast_Simulation_'+str(current_index)+'.pac')
except WindowsError:
   pass
try:
   os.remove('Breast_Simulation_'+str(current_index)+'.prt')
except WindowsError:
   pass
try:
   os.remove('Breast_Simulation_'+str(current_index)+'.res')
except WindowsError:
   pass
try:
   os.remove('Breast_Simulation_'+str(current_index)+'.sel')
except WindowsError:
   pass
try:
   os.remove('Breast_Simulation_'+str(current_index)+'.stt')
except WindowsError:
```

```
    pass
try:
    os.remove('Breast_Simulation_'+str(current_index)+'.sta')
except WindowsError:
    pass
try:
    os.remove('Breast_Simulation_'+str(current_index)+'.mdl')
except WindowsError:
    pass
try:
    os.remove('Breast_Simulation_'+str(current_index)+'.log')
except WindowsError:
    pass
try:
    os.remove('Breast_Simulation_'+str(current_index)+'.msg')
except WindowsError:
    pass
try:
    os.remove('Breast_Simulation_'+str(current_index)+'.dat')
except WindowsError:
    pass
try:
    os.remove('Breast_Simulation_'+str(current_index)+'.com')
except WindowsError:
    pass
if remove_odb:
    try:
        os.remove('Breast_Simulation_' + str(current_index) + '.odb')
    except WindowsError:
        pass
current_index = current_index + 1
```

```
        # Write error message
len_fail_mesh = len(failed_mesh)
features_file.close()
with open('Failed_simulation.txt', 'w') as f:
    for i in range(0, len_fail_mesh):
        f.write('%s, ' % failed_mesh[i])
    f.write('\nOut of '+str(num_sims)+' simulations, '+str(len_fail_mesh)+' have failed due to mesh generation.')
```

Appendix C: Depth Estimation Code

Preprocessing Code

```
def preprocess_signal(file_path, normalize=True, plot=False,
                      total_time=3e-6, time_increment=2e-9, end_sample=27000):
    '''
    Preprocesses ultrasound signal data from a CSV file with truncation and normalization.

    Parameters:
    - file_path (str): Path to the CSV file.
    - normalize (bool): Whether to normalize the signals.
    - plot (bool): Whether to plot the signals for visualization.
    - total_time (float): Total time duration to truncate from the start (default: 3e-6).
    - time_increment (float): Time increment between each sample (default: 2e-9).
    - end_sample (int): Last sample index to include (default: 27000).

    Returns:
    - pd.DataFrame: Preprocessed DataFrame.
    '''
    # Load data and skip initial rows
    df = pd.read_csv(file_path, skiprows=1, header=None, index_col=0)

    # Remove non-numeric columns
    df = df.iloc[:, 1:]
    df = df.T
    df = df[~np.isnan(df).any(axis=1)]
    row, column = df.shape
    print(row, column)

    # Calculate starting sample based on truncation time
    sampling_num = int(total_time / time_increment)
    print(f"Truncating signal from sample {sampling_num} to {end_sample}")
```

```
    # Truncate signal to remove initial pulse and signal tail
    df= df.T.iloc[:, sampling_num:27000]

    # Normalize data
    if normalize and not df.empty:
        scaler = MinMaxScaler()
        df_scaled = (pd.DataFrame(scaler.fit_transform(df.T)))
    else:
        df_scaled = df.copy()

    # Optional visualization
    if plot and not df_scaled.empty:
        plt.figure(figsize=(15, 5))
        for i in range(min(5, len(df_scaled))):
            plt.plot(df_scaled.iloc[i, :], label=f'Signal {i+1}')
        plt.title('Sample Signals After Preprocessing')
        plt.xlabel('Sample Number')
        plt.ylabel('Amplitude (Normalized)' if normalize else 'Amplitude')
        plt.legend()
        plt.show()
    return df_scaled
```

Depth Calculation Code

With Dips

```
def calculate_depth_from_signal_dip(signal, speed_of_sound=1490,
                                    time_increment=2e-9,
                                    truncation_time=3e-6, plot=False,
                                    height_threshold=-0.5, distance_threshold=1000):
    '''
    Calculate depth based on dips (valleys) detected in a preprocessed ultrasound signal.
```

```
Parameters:
- signal (array): The ultrasound signal as a 1D numpy array.
- speed_of_sound (float): Speed of sound in breast tissue (default: 1490 m/s).
- time_increment (float): Time increment between each sample
- truncation_time (float): Time duration removed due to truncation (default: 3e-6 seconds).
- plot (bool): Whether to visualize the signal and detected dips.
- height_threshold (float): Minimum depth of dip for detection.
- distance_threshold (int): Minimum distance between detected dips.

Returns:
- depth_meters (float): Calculated depth in meters.
'''

# Invert the signal to find dips as peaks
inverted_signal = -signal

# Detect dips in the inverted signal
dips, _ = find_peaks(inverted_signal, height=height_threshold, distance=distance_threshold)
print(len(dips))

# Visualization of the signal and detected dips
if plot:
    plt.figure(figsize=(15, 5))
    plt.plot(signal, label='Original Signal')
    plt.scatter(dips, signal[dips], color='red', label='Detected Dips')
    plt.xlabel('Sample Number')
    plt.ylabel('Amplitude')
    plt.title('Signal with Detected Dips')
    plt.legend()
    plt.show()
```

```
    # If no dips are detected, return None
    if len(dips) < 1:
        print("No significant dips detected.")
        return None

    # Select the first significant dip (adjust if needed)
    first_dip = dips[0]

    # Calculate the actual time of this dip (accounting for truncation)
    dip_time = truncation_time + (first_dip * time_increment)

    # Calculate depth (divide by 2 to account for round-trip)
    depth_meters = (speed_of_sound * dip_time) /2

    # Print output
    print(f"First Dip Sample: {first_dip}")
    print(f"Dip Time (including truncation): {dip_time:.9f} seconds")
    print(f"Estimated Depth: {depth_meters:.6f} meters")

    return depth_meters
```

With Peaks

```
def calculate_depth_from_signal_peaks(signal, speed_of_sound=1490,
                                      time_increment=2e-9,
                                      truncation_time=3e-6, plot=False,
                                      height_threshold=0.5, distance_threshold=10000):
    '''
    Calculate depth based on peaks detected in a preprocessed ultrasound signal.

    Parameters:
```

```
- signal (array): The ultrasound signal as a 1D numpy array.
- speed_of_sound (float): Speed of sound in breast tissue (default: 1490 m/s).
- time_increment (float): Time increment between each sample
- truncation_time (float): Time duration removed due to truncation (default: 3e-6 seconds).
- plot (bool): Whether to visualize the signal and detected dips.
- height_threshold (float): Minimum depth of dip for detection.
- distance_threshold (int): Minimum distance between detected dips.

Returns:
- depth_meters (float): Calculated depth in meters.
'''

# Detect dips in the inverted signal
peaks, _ = find_peaks(signal, height=height_threshold, distance=distance_threshold)

# Visualization of the signal and detected dips
if plot:
    plt.figure(figsize=(15, 5))
    plt.plot(signal, label='Original Signal')
    plt.scatter(peaks, signal[peaks], color='red', label='Detected Peaks')
    plt.xlabel('Sample Number')
    plt.ylabel('Amplitude')
    plt.title('Signal with Detected Peaks')
    plt.legend()
    plt.show()

# If no dips are detected, return None
if len(peaks) < 1:
    print("No significant dips detected.")
    return None
```

```
# Select the first significant dip (adjust if needed)
first_peak = peaks[0]

# Calculate the actual time of this dip (accounting for truncation)
peak_time = truncation_time + (first_peak * time_increment)

# Calculate depth (divide by 2 to account for round-trip)
depth_meters = (speed_of_sound * peak_time) / 2

# Print output
print(f"First Peak Sample: {first_peak}")
print(f"Peak Time (including truncation): {peak_time:.9f} seconds")
print(f"Estimated Depth: {depth_meters:.6f} meters")

return depth_meters
```

Appendix D: Abaqus Model

Example Simulated Abaqus Model Scenarios

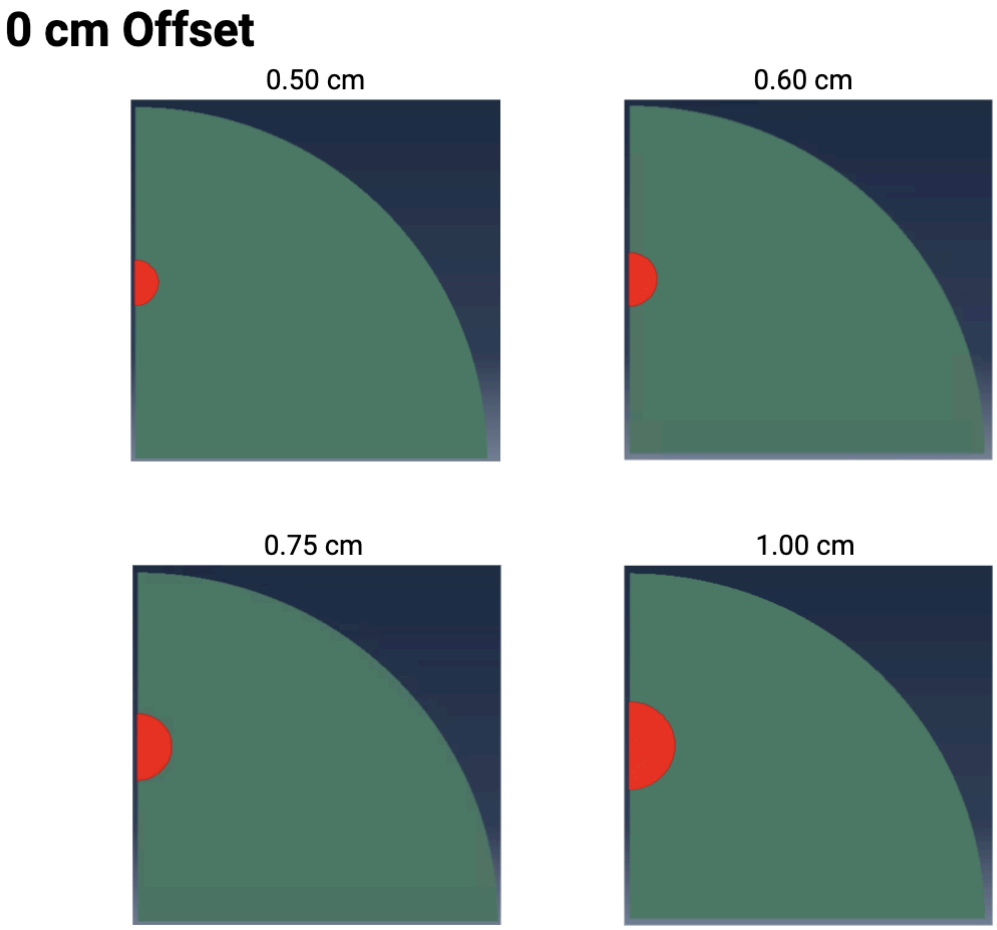

Figure D1. *Example Abaqus Model images where tumor sizes were varied as indicated above each image. Tumors were kept at center of the breast.*

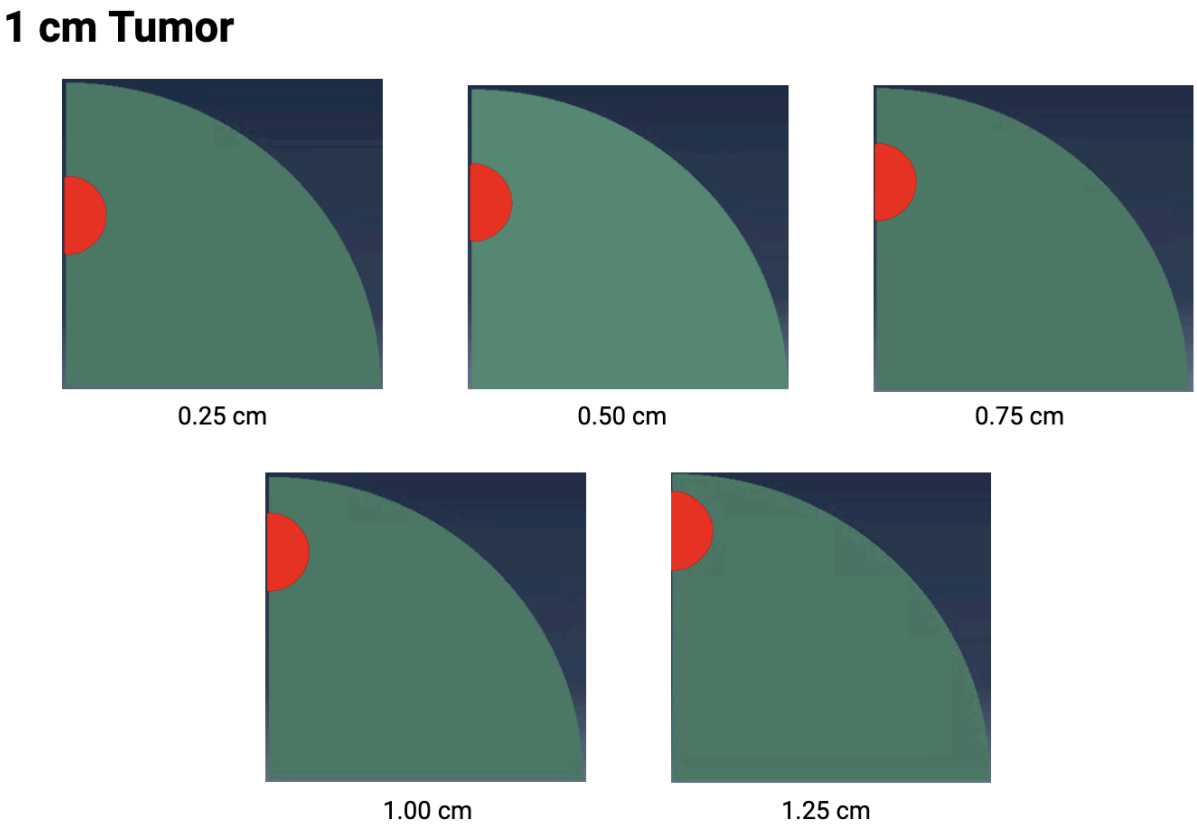

Figure D2. *Example Abaqus Model images where offsets were varied as indicated below each image. Tumor diameter was kept constant at 1 cm.*

Example Abaqus Wave Propagation Simulation

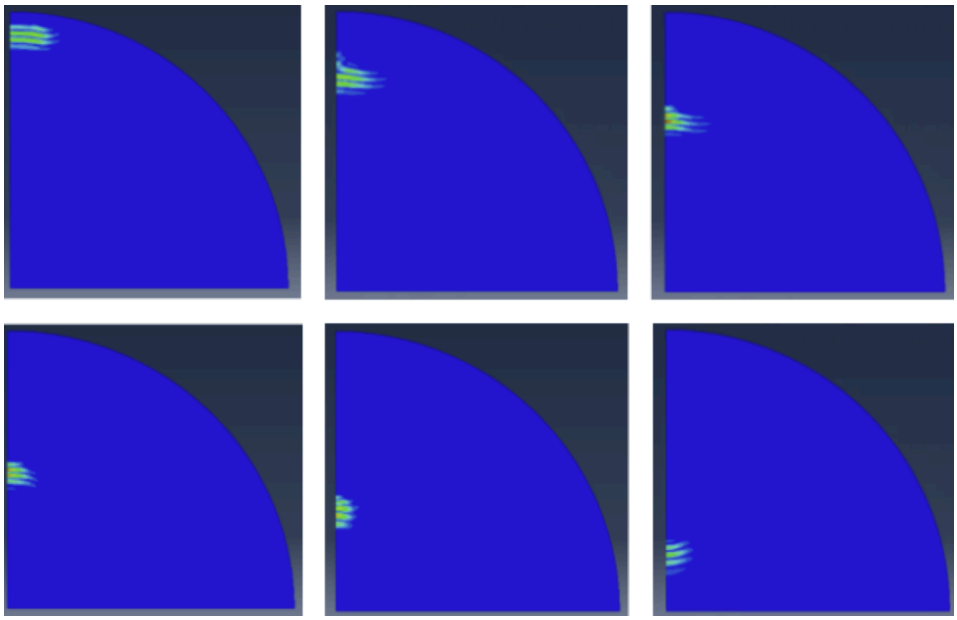

Figure D3. *Abaqus sound wave simulation moving down through breast-tumor system with 10 mm tumor at 0 mm offset.*

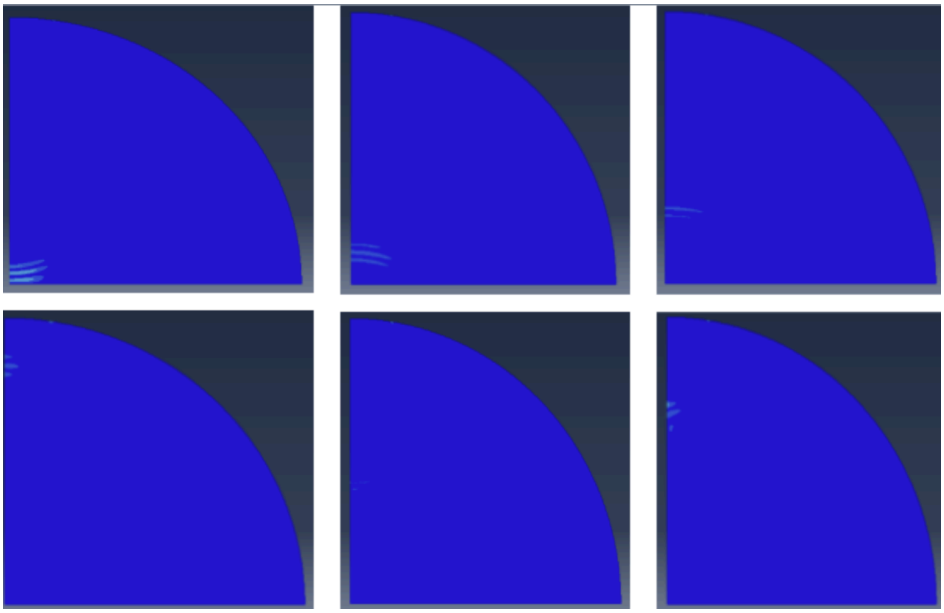

Figure D4. *Abaqus sound wave simulation reflecting up through breast-tumor system with 10 mm tumor at 0 mm offset.*

Appendix E: Processed Signals

Signal Preprocessing Example

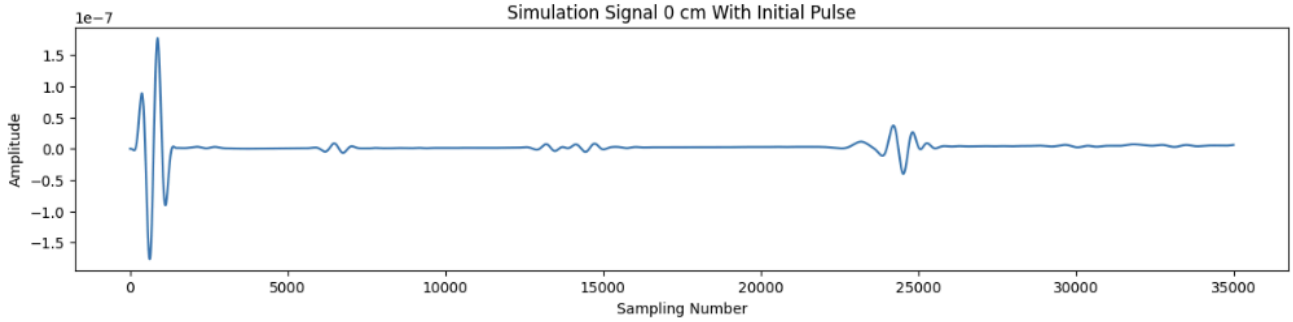

Figure E1. *Non-processed signal for 10 mm tumor at center.*

.

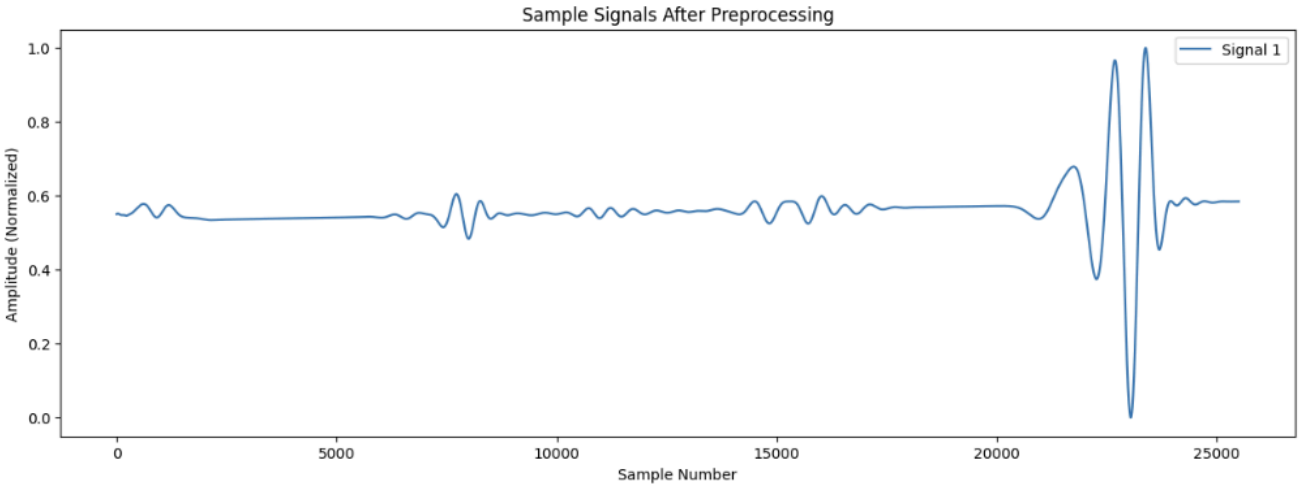

Figure E2. *Example of processed signal for 10 mm tumor at center*

Dip and Peak Identification for Baseline Simulations

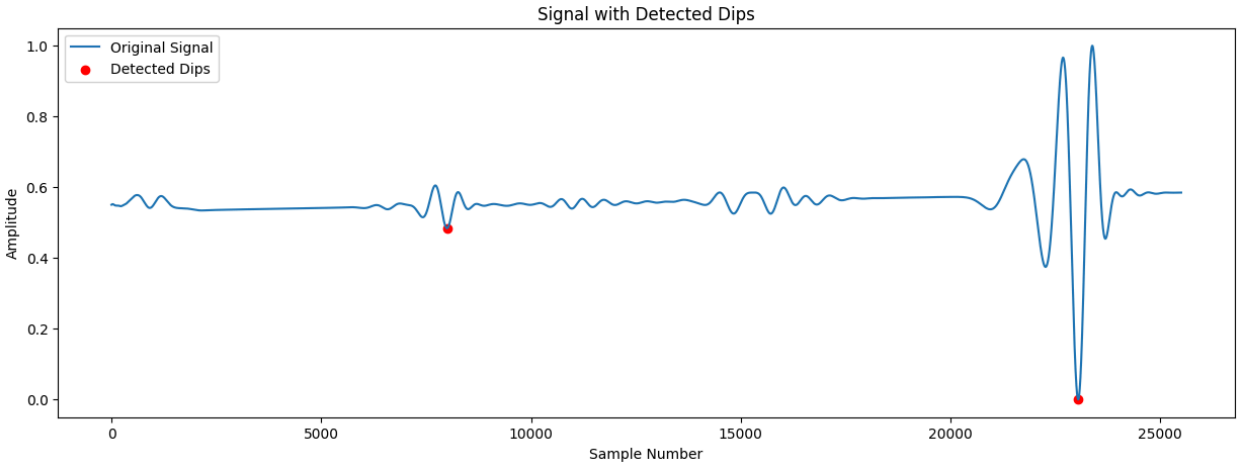

Figure E3. *Dip identification for 10 mm tumor 0 offset.*

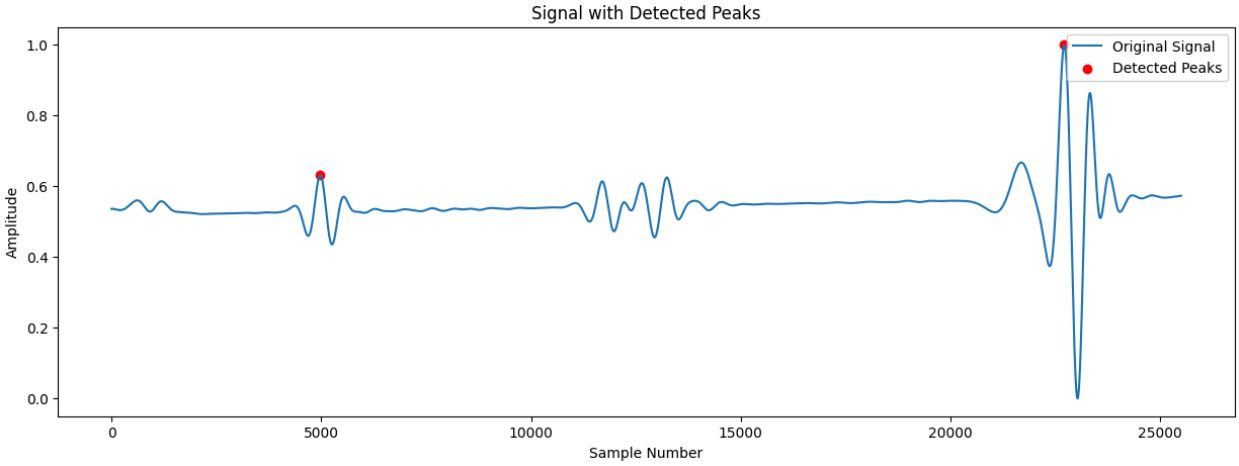

Figure E4. *Peak identification for 10 mm tumor at center.*

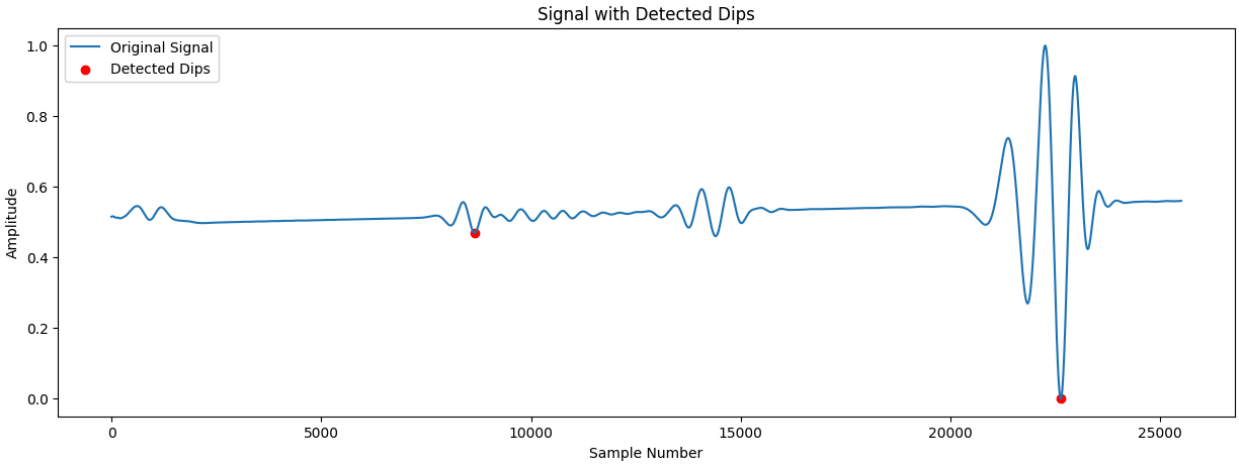

***Figure E5**. Dip identification for 7.5 mm tumor at center.*

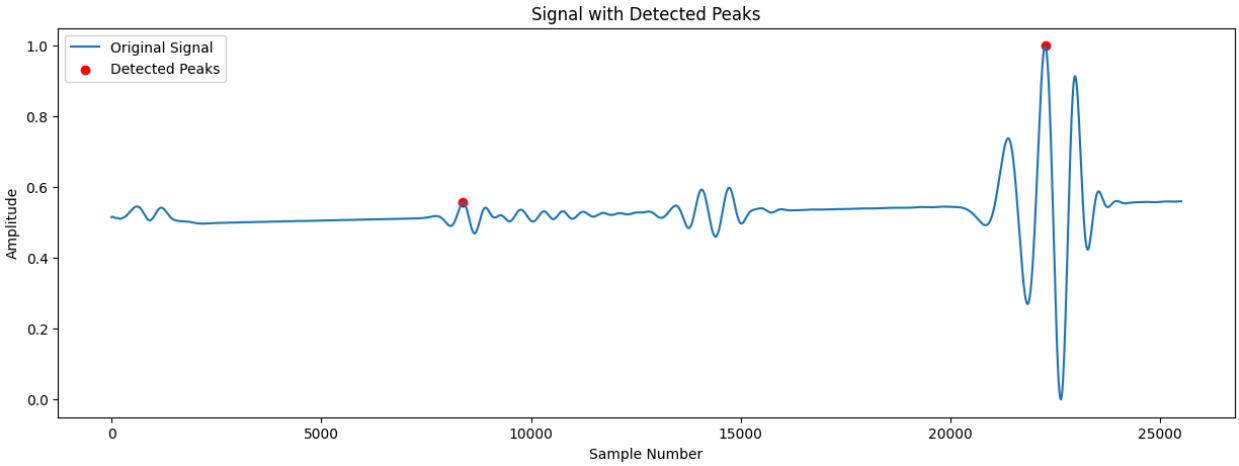

***Figure E6**. Peak identification for 7.5 mm tumor at center.*

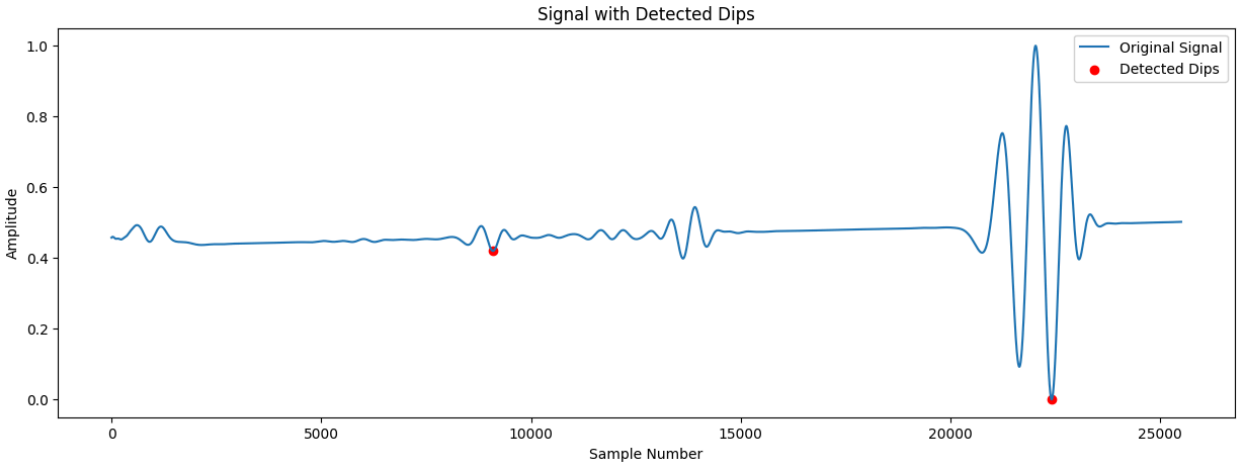

***Figure E7.** Dip identification for 6 mm tumor at center.*

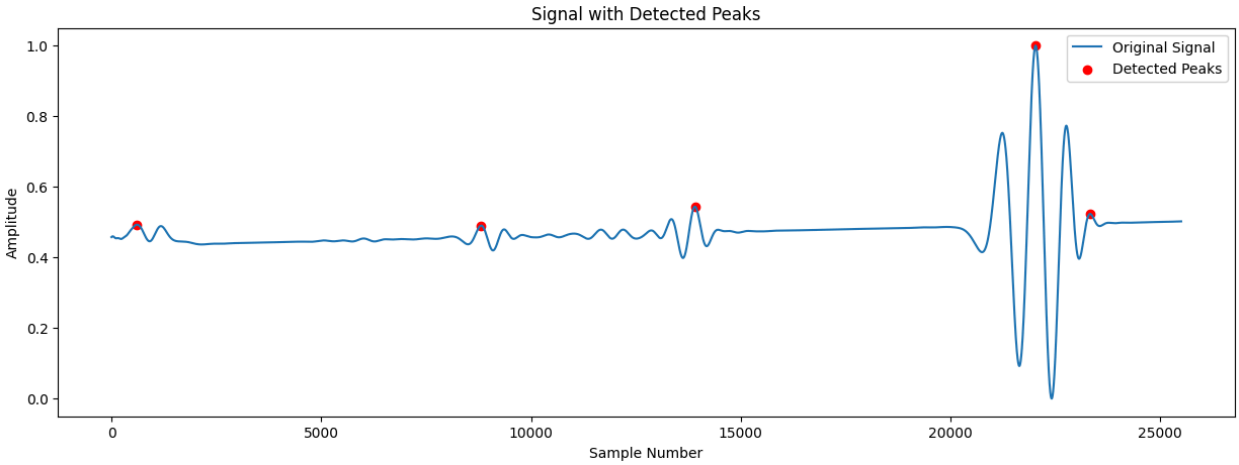

Figure E8. *Peak identification for 6 mm tumor at center.*

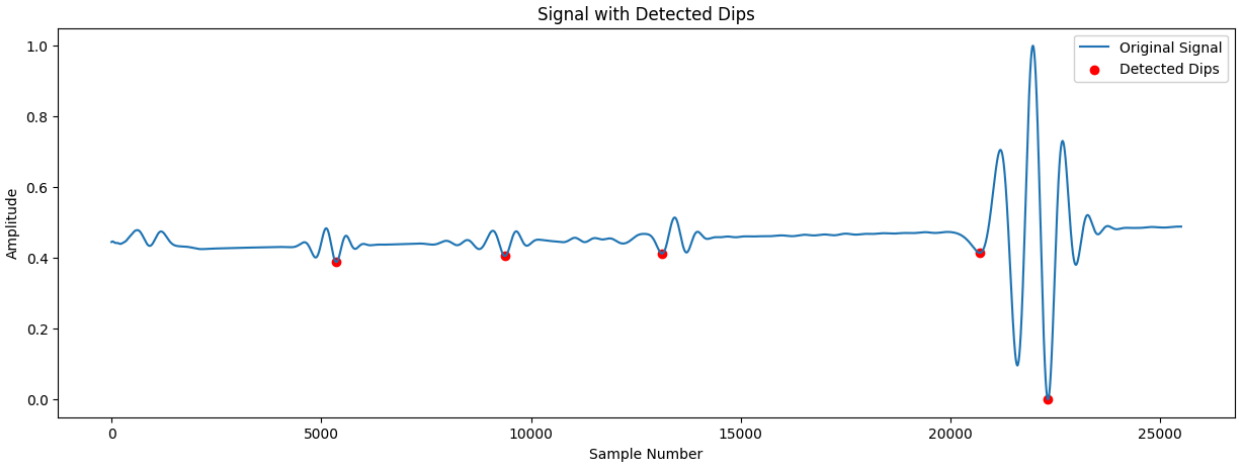

Figure E9. *Dip identification for 5 mm tumor at center.*

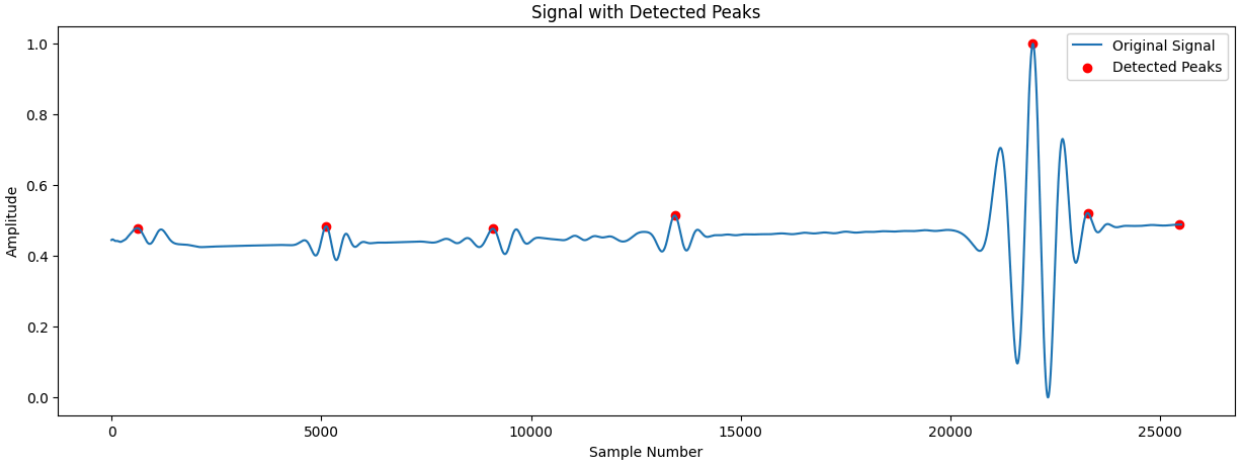

Figure E10. *Peak identification for 5 mm tumor at center.*

Miscellaneous Dip and Peak Identification

This study analyzed simulations with 4 tumor sizes at 11 vertical offsets, comprising 44 simulations. Each signal result was analyzed with two methods, yielding 88 total analyzed signals. The following signals were selected as a representative subset of the total data.

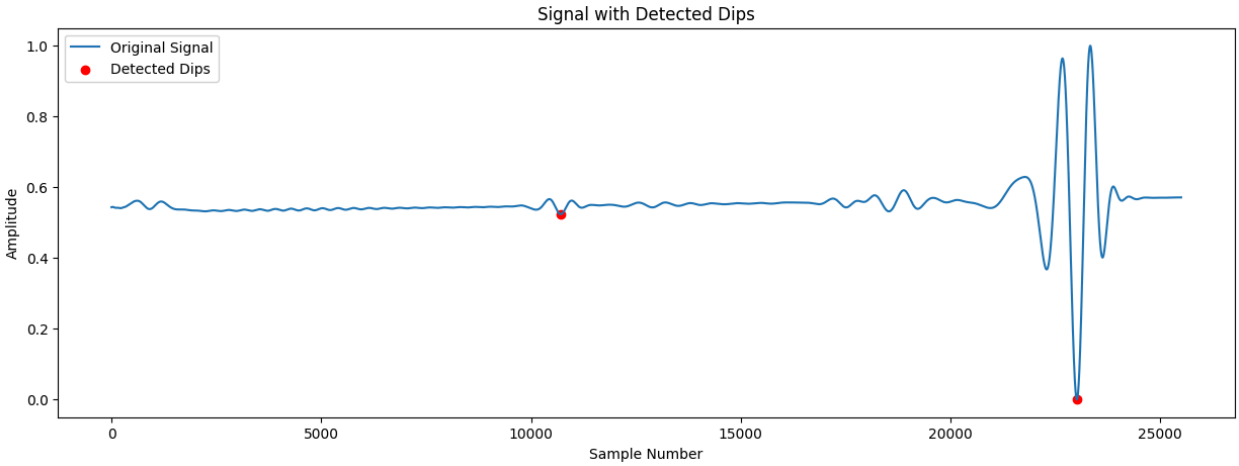

Figure E11. *Dip identification for 7.5 mm tumor -5 mm offset.*

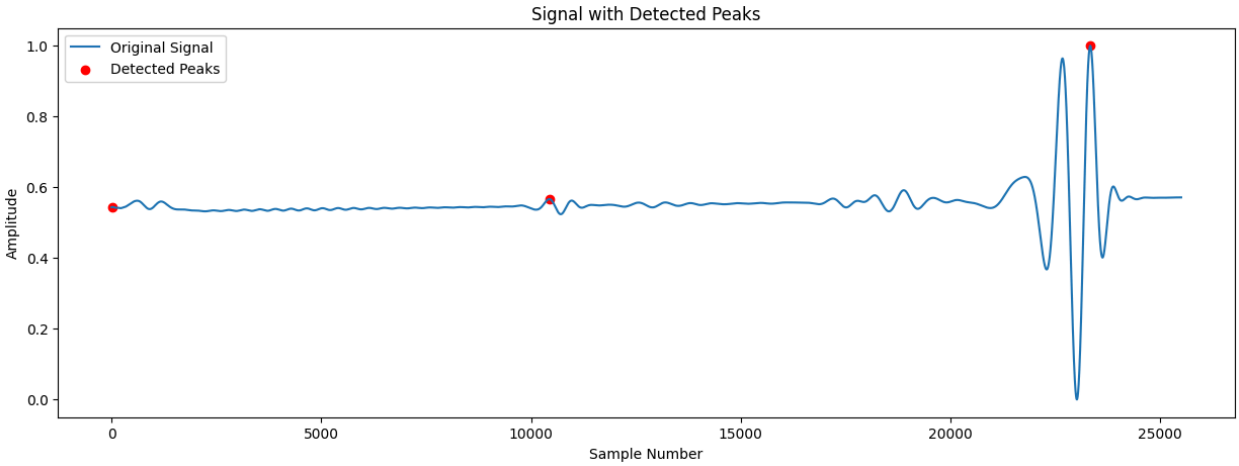

Figure E12. *Peak identification for 7.5 mm tumor -5 mm offset.*

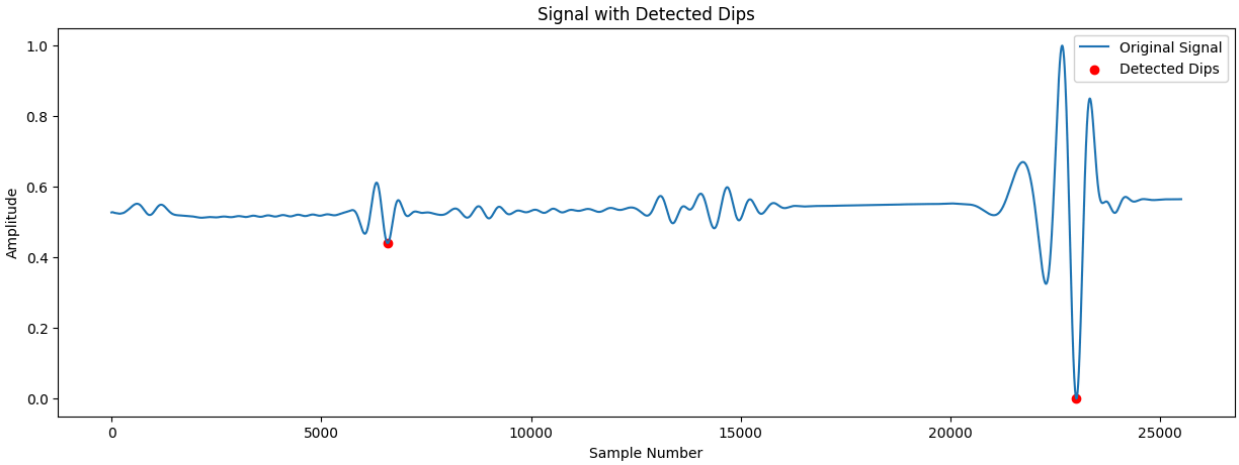

Figure E13. *Dip identification for 10 mm tumor +2.5 mm offset.*

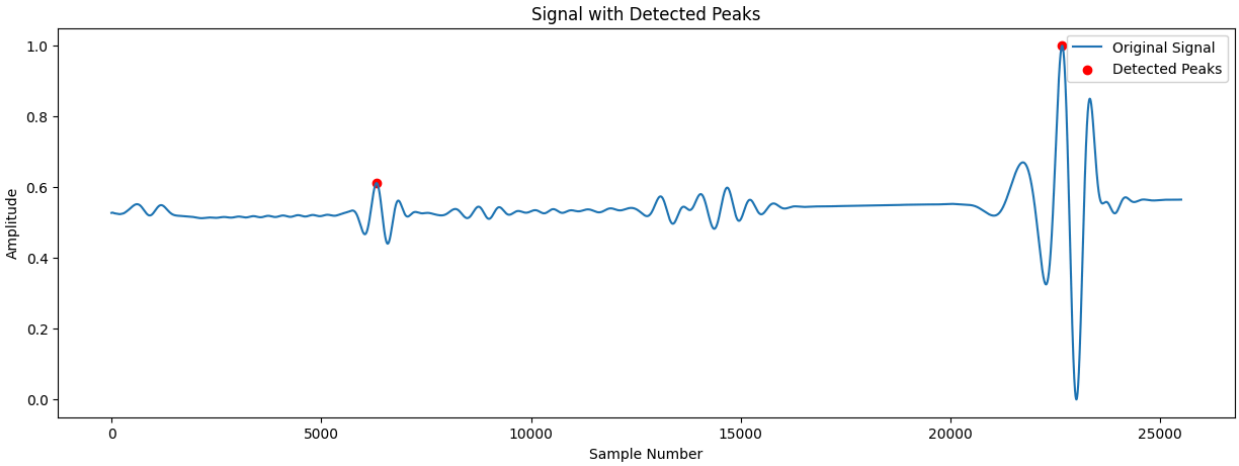

Figure E14. *Peak identification for 10 mm tumor +2.5 mm offset.*

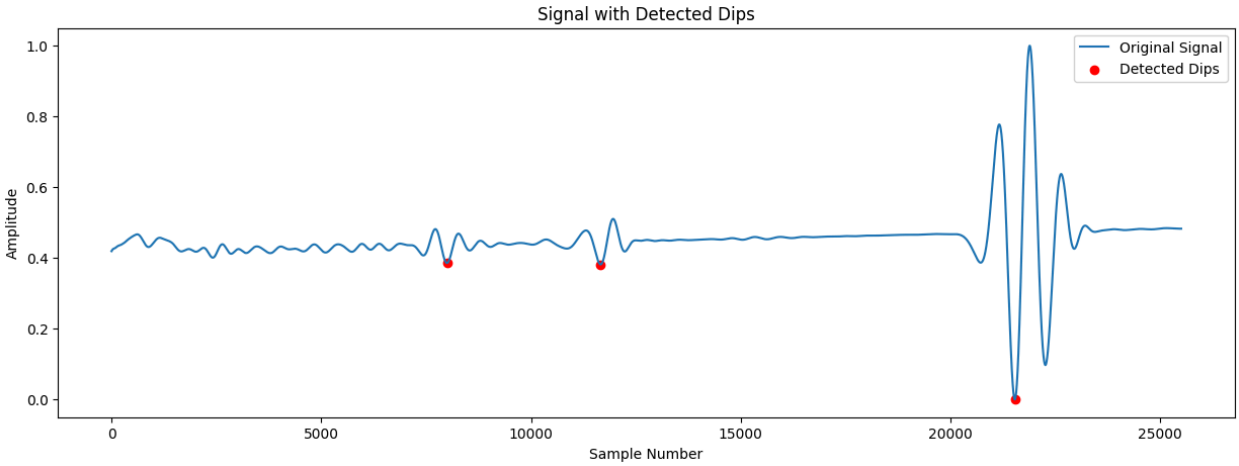

Figure E15. *Dip identification for 5 mm tumor +5 mm offset.*

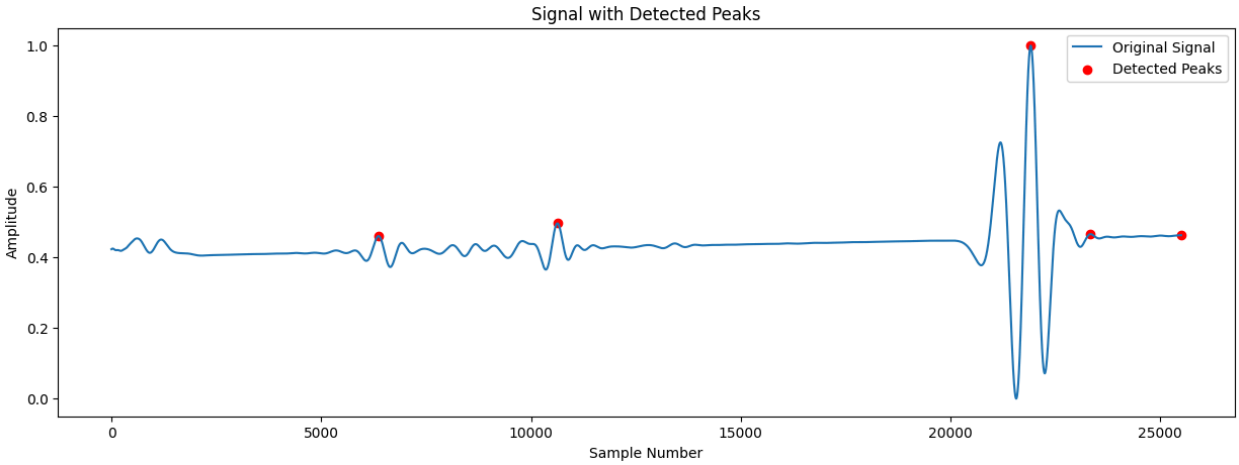

Figure E16*. Peak identification for 5 mm tumor +5 mm offset.*

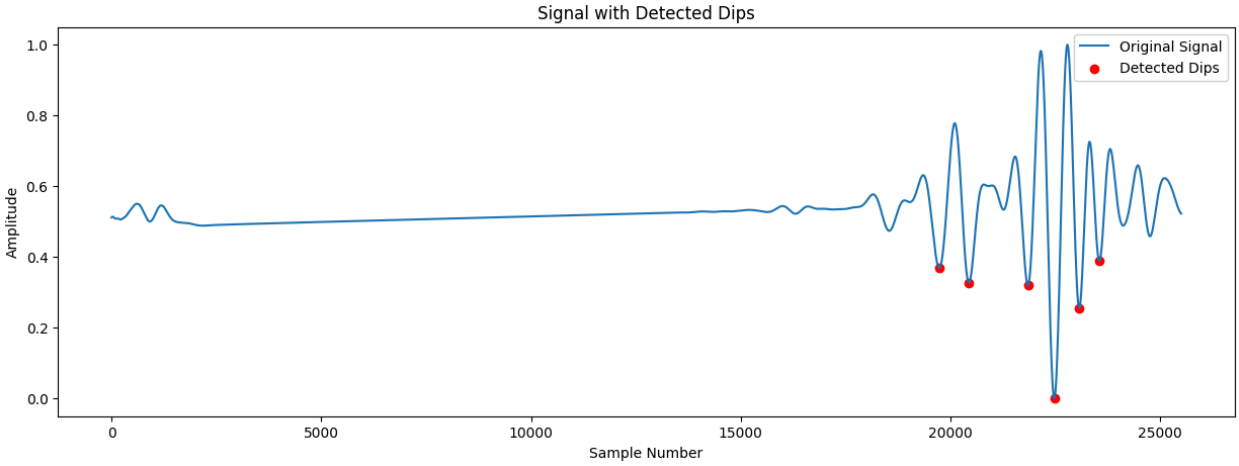

Figure E17*. Dip identification for 5 mm tumor -12.5 mm offset.*

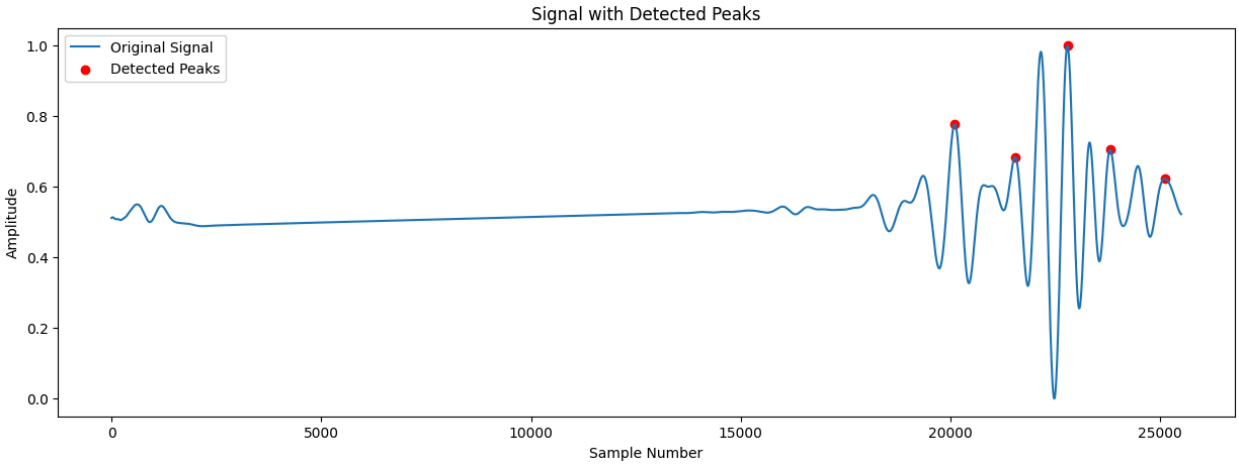

Figure E18. *Peak identification for 5 mm tumor -12.5 mm offset.*

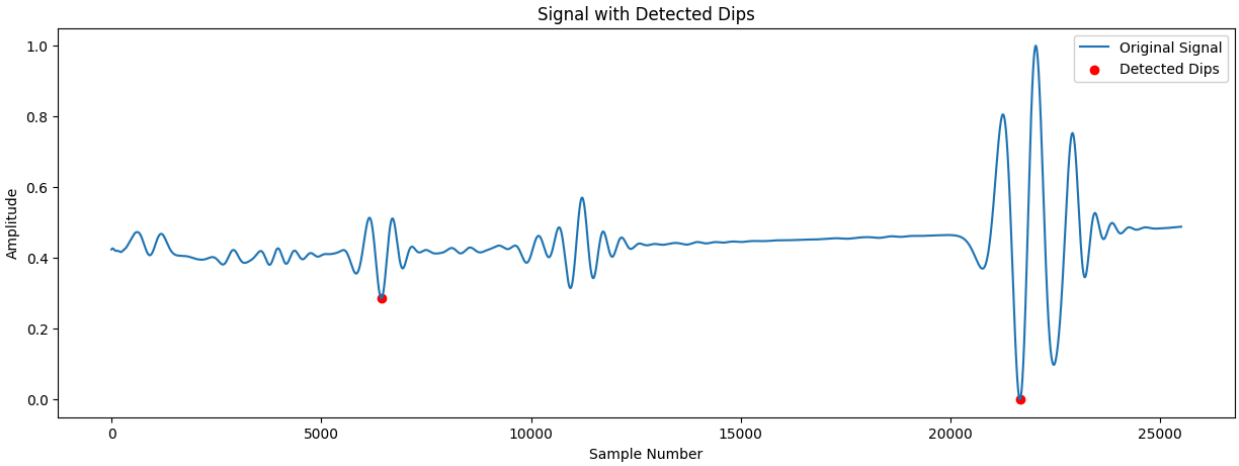

Figure E19. *Dip identification for 6 mm tumor +5 mm offset.*

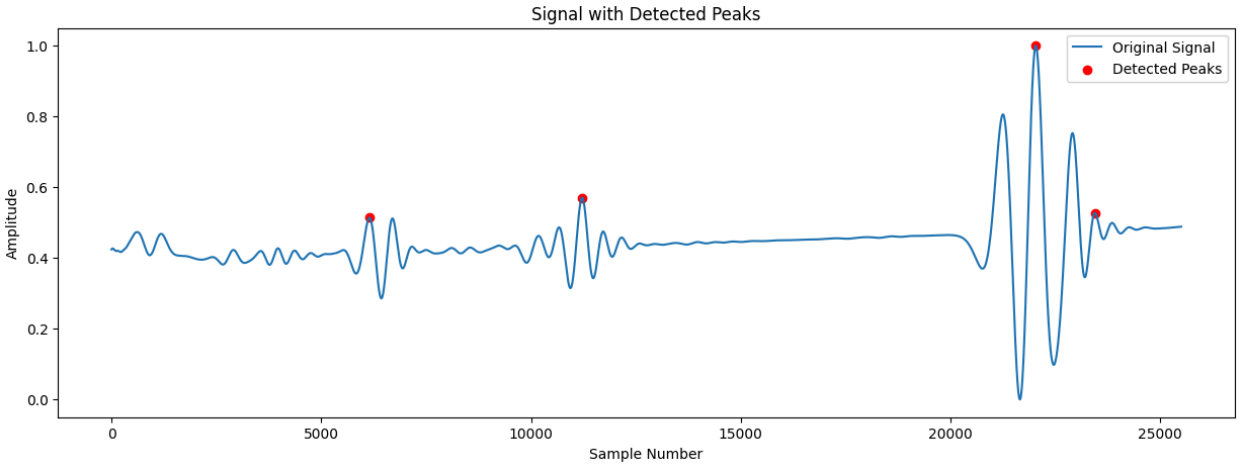

Figure E20. *Peak identification for 6 mm tumor +5 mm offset.*

Miscellaneous Overlaid Processed Signals

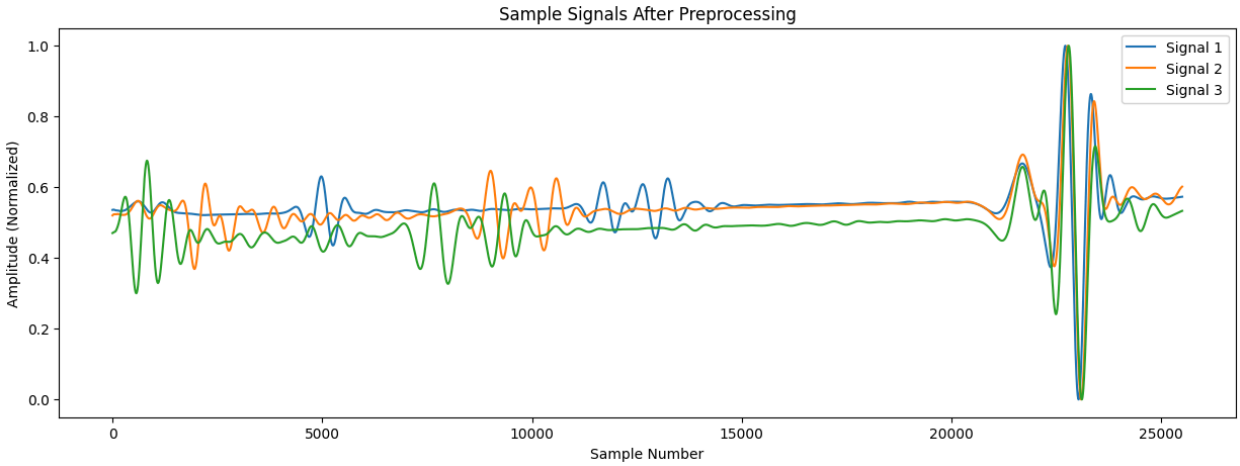

Figure E21. *Processed signals overlaid for 10 mm tumor moving up at intervals. (Blue=2.5 mm, Orange = 7.5 mm, Green = 12.5 mm)*

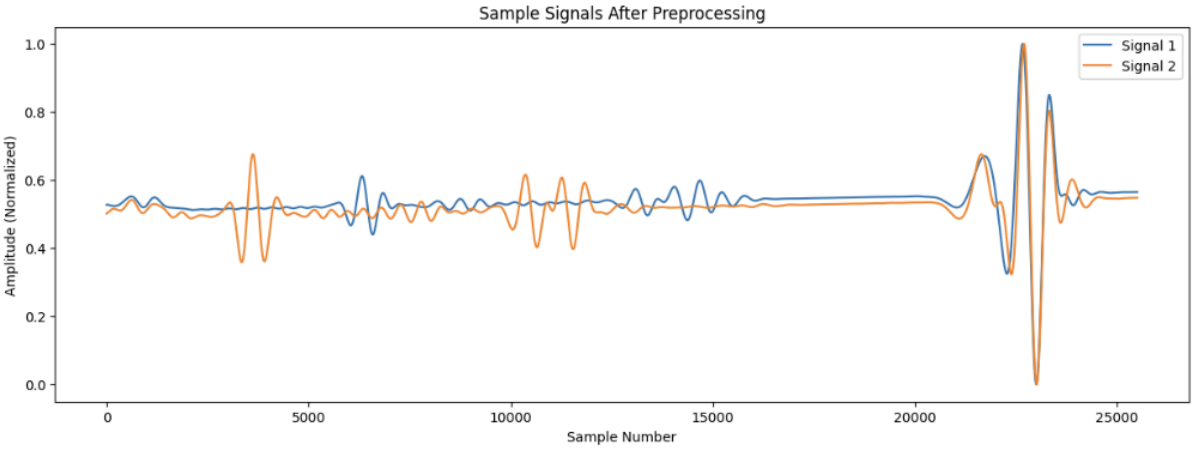

Figure E22. *Processed signals overlaid for 10 mm tumor moving up at intervals. (Blue=5 mm, Orange = 10 mm)*

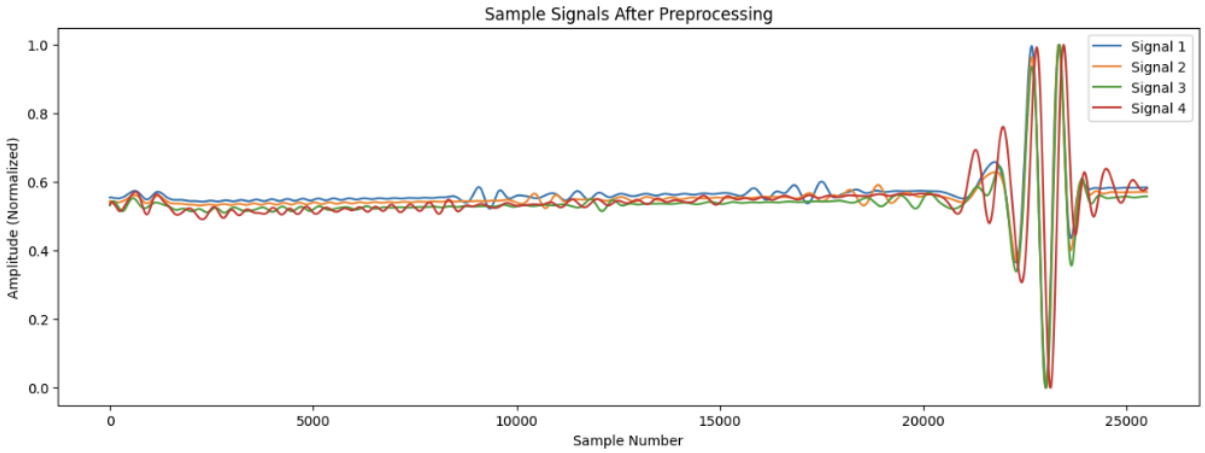

Figure E23. *Processed signals overlaid for 10 mm tumor moving down at intervals. (Blue=2.5 mm, Orange = 5 mm, Green = 7.5 mm, Red = 12.5 mm)*

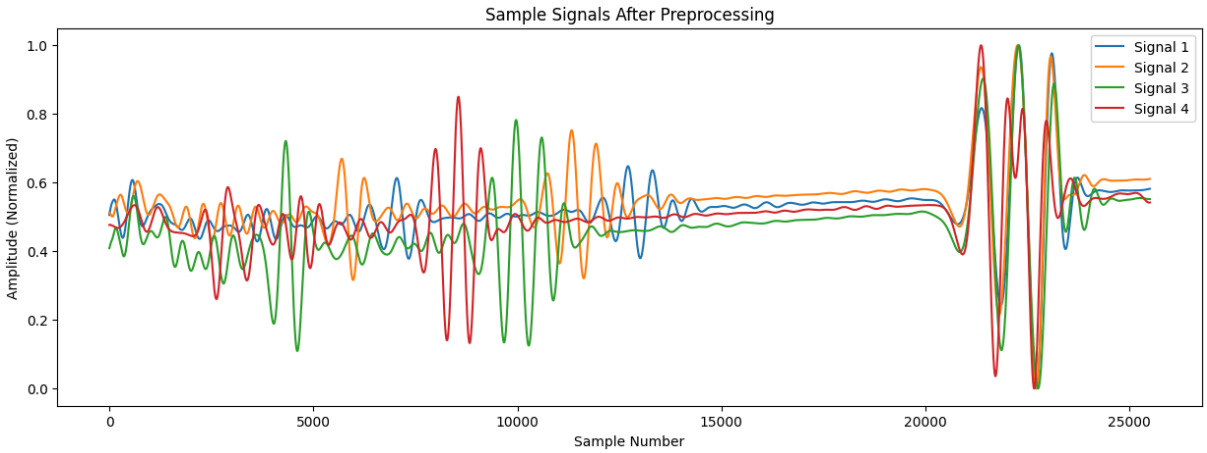

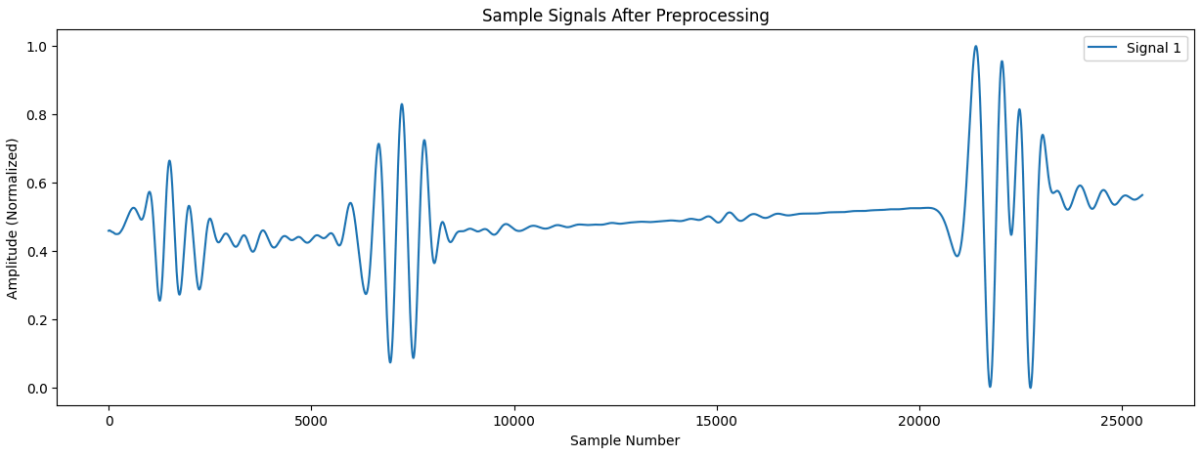

Figure E24. *Processed signals overlaid for 7.5 mm tumor moving up at intervals. (Blue=2.5 mm, Orange = 5 mm, Green = 7.5 mm, Red = 10 mm, Blue (in X.B) = 12.5 mm)*

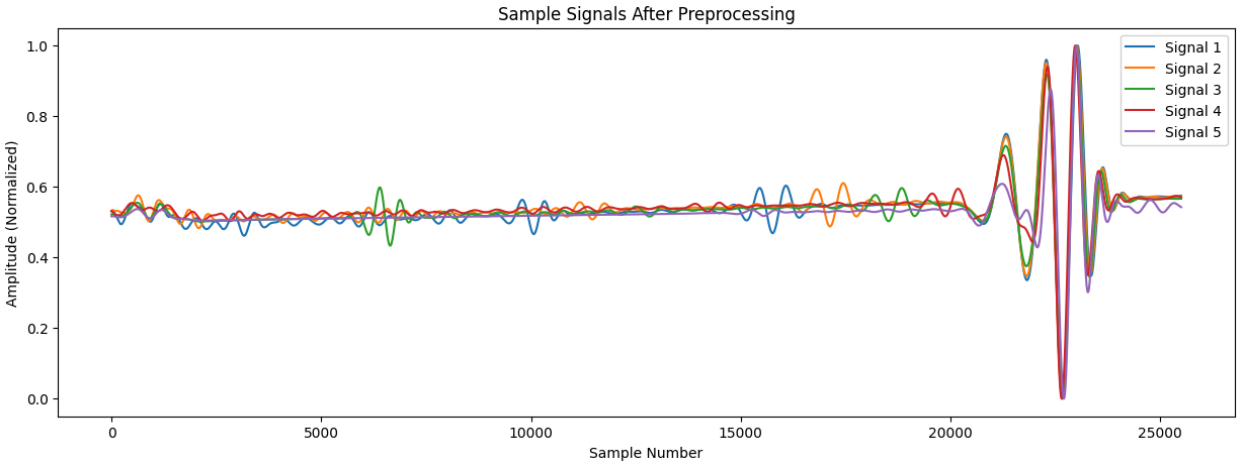

Figure E25. *Processed signals overlaid for 7.5 mm tumor moving down at intervals. (Blue=2.5 mm, Orange = 5 mm, Green = 7.5 mm, Red = 10 mm, Purple = 12.5 mm)*

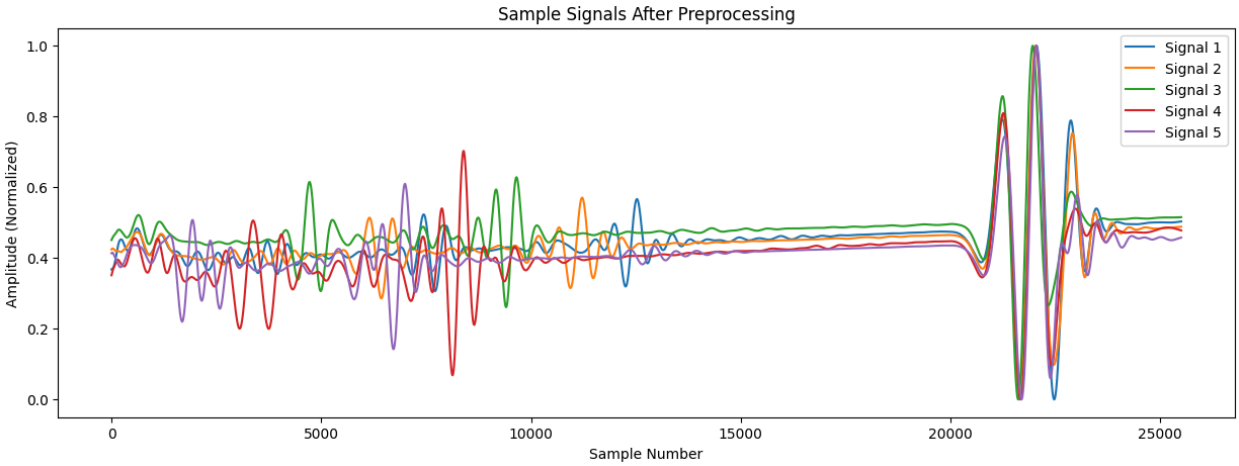

Figure E26. *Processed signals overlaid for 6 mm tumor moving up at intervals. (Blue=2.5 mm, Orange = 5 mm, Green = 7.5 mm, Red = 10 mm, Purple = 12.5 mm)*

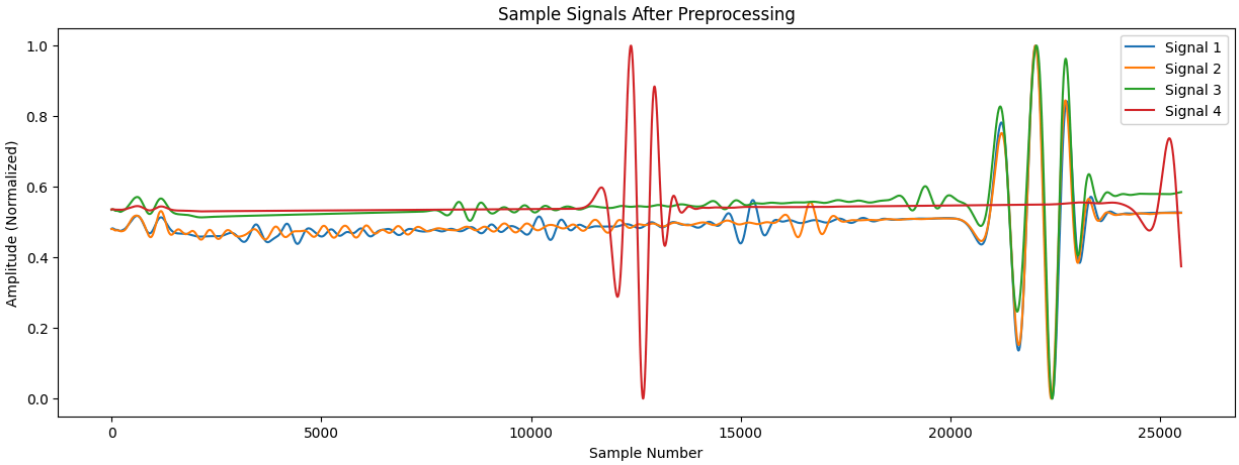

Figure E27. *Processed signals overlaid for 6 mm tumor moving down at discussed intervals. (Blue=2.5 mm, Orange = 5 mm, Green = 7.5 mm, Red = 10 mm)*

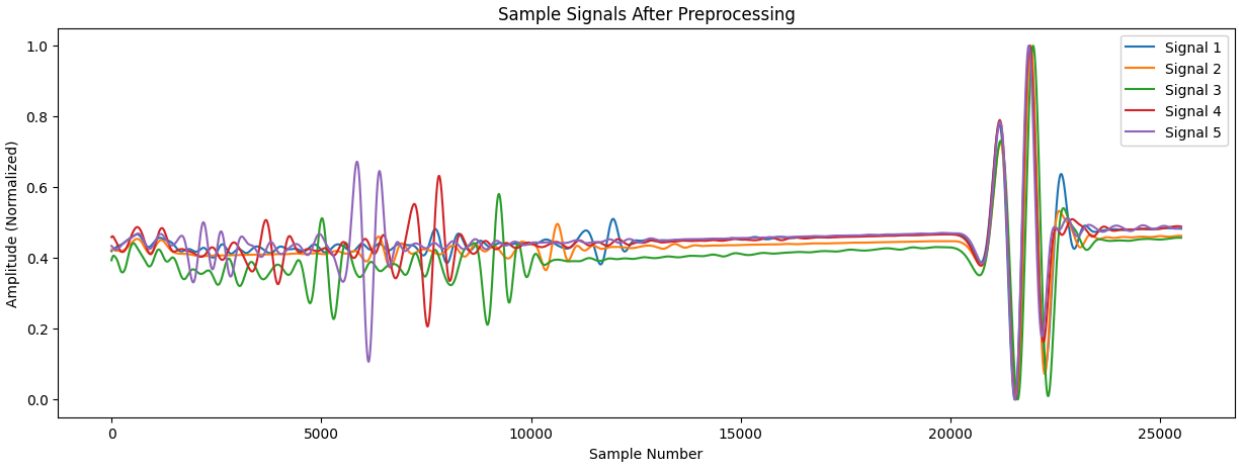

Figure E28. *Processed signals overlaid for 5 mm tumor moving up at intervals. (Blue=2.5 mm, Orange = 5 mm, Green = 7.5 mm, Red = 10 mm, Purple = 12.5 mm)*

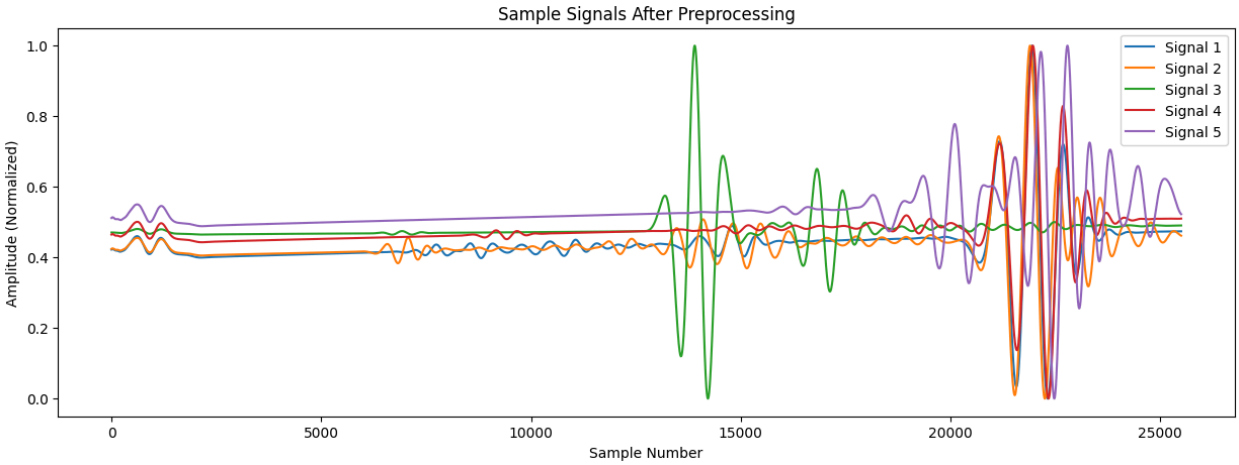

Figure E29. *Processed signals overlaid for 5 mm tumor moving down at intervals. (Blue=2.5 mm, Orange = 5 mm, Green = 7.5 mm, Red = 10 mm, Purple = 12.5 mm)*

Appendix F: Method Comparison Data

Table F1. *Average percent error of both dip and peak based estimation methods for each offset across all tumor size cases.*

Offset	Dip Average % Error	Peak Average % Error
+0.0125	10.25	20.32445
+0.0100	6.23125	5.57675
+0.0075	1.918625	1.977575
+0.0050	1.525625	4.8666
+0.0025	4.7254	7.683975
0.0000	6.76675	9.3104
-0.0025	11.893825	10.9017
-0.0050	7.813175	8.0403
-0.0075	5.195325	6.0515
-0.0100	18.45745	17.6031
-0.0125	21.086675	23.173525

Table F2. *Average percent error of dip-based estimation method for positive, negative and no offset scenarios for each tumor size.*

	5 mm tumor	6 mm tumor	7.5 mm tumor	10 mm tumor	Average
Positive Offset	4.2464	5.15354	3.48878	6.832	4.93018
Baseline	7.3714	7.1471	6.8985	5.65	6.76675
Negative Offset	11.27008	13.36752	15.33156	11.588	12.88929

Table F3. *Average percent error of peak-based estimation method for positive, negative and no offset scenarios for each tumor size.*

	5 mm tumor	6 mm tumor	7.5 mm tumor	10 mm tumor	Average
Positive Offset	6.09944	6.5924	7.45164	12.2	8.08587
Baseline	9.8229	9.6118	9.3969	8.41	9.3104
Negative Offset	10.94094	14.75896	17.8278	9.0884	13.154025

Appendix G: Sample Calculations

Calculating Ultrasound Wavelength and Mesh Size

For a case where the speed of sound of the tissue is 1490 m/s, which is the speed of sound of the breast tissue in all simulations run:

Wavelength:

$$\lambda = \frac{c}{f} = \frac{1490\ m/s}{1\times10^{6} Hz} = \ 0.00149\ m\ =\ 1.49\ mm$$

Mesh size:

$$Element\ size\ =\ \frac{\lambda}{10} = \frac{1.49}{10} = 0.149\ mm$$

Estimating Tumor Depth from Time-of-Flight

In the case of the 10 mm tumor embedded in the breast phantom at the center, the time of flight was found to be 0.000018996 including the time of truncation (3e-6s). Speed of sound of the tissue was calculated to be 1490 m/s.

$$Depth\ =\ \frac{c\cdot t}{2} = \ \frac{1490\cdot1.8996\times10^{-5}}{2} = \ \frac{0.02830404}{2} = 0.01415202$$

Calculating True Tumor Depth

In the case of a 10 mm tumor embedded in the breast phantom at the center, the true depth would be determined as follows:

$$True\ Depth\ =\ r_{breast} \pm offset\ - r_{tumor} = \ 20\ mm\ +\ 0\ mm\ -\ 5\ mm\ =\ 15\ mm$$

In the case of a 10 mm tumor embedded in the breast phantom 5 mm upward from center, the true depth would be determined as follows:

$$True\ Depth\ =\ 20\ mm\ -\ 5\ mm\ -\ 5\ mm\ =\ 10\ mm$$

In the case of a 10 mm tumor embedded in the breast phantom 5 mm downward from center, the true depth would be determined as follows:

$$True\ Depth\ =\ 20\ mm\ +\ 5\ mm\ -\ 5\ mm\ =\ 20\ mm$$

Calculating Percent Error in Estimated Depth

In the case of the 10 mm tumor embedded in the center of the breast phantom, the percent error was calculated as follows:

$$Abs\ error\ =\ |Estimated\ Depth\ -\ True\ Depth| = |0.01415202\ -\ 0.015| = 0.00084798$$

Calculating Percent Error in Estimated Depth

In the case of the 10 mm tumor embedded in the center of the breast phantom, the percent error was calculated as follows:

$$\%\ error\ =\ \frac{|Estimated\ Depth - True\ Depth|}{True\ Depth} = \frac{|0.01415202 - 0.015|}{0.015} =\ 0.056532$$

$$\rightarrow 0.056532 \cdot 100\ =\ 5.632\%$$

Appendix H: Depth Estimation Error

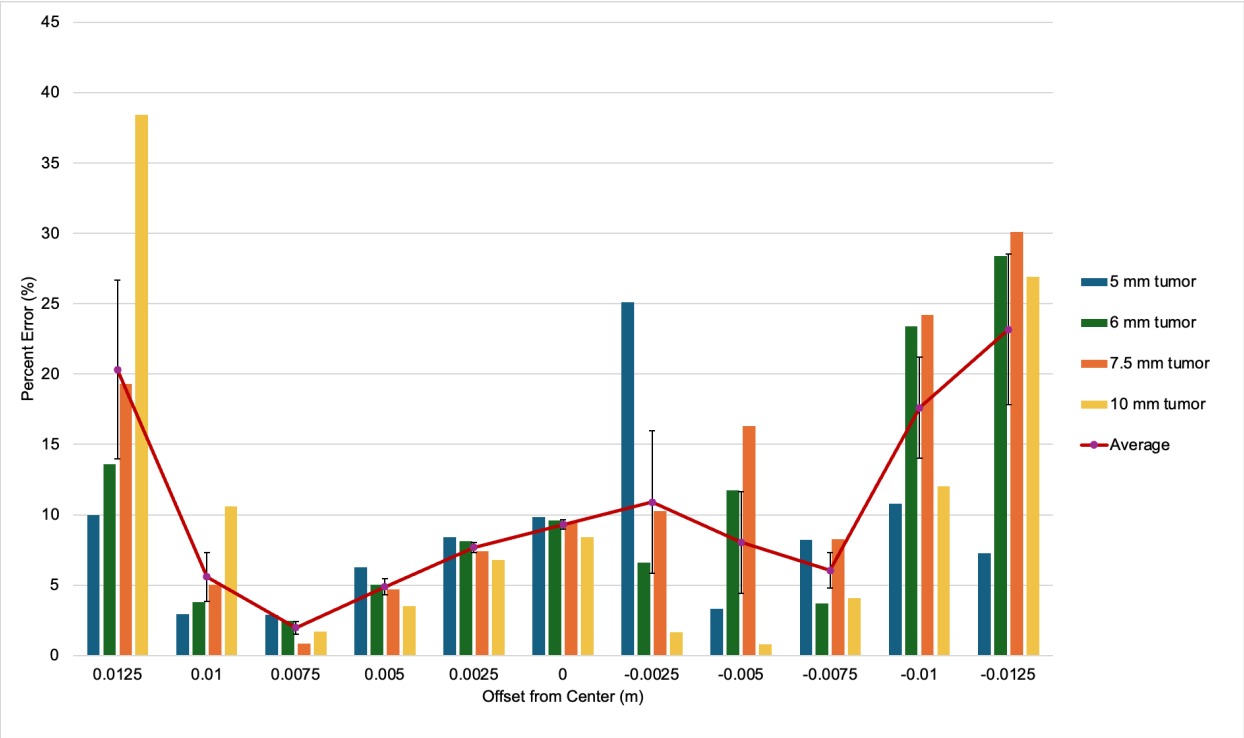

Figure H1*. Percent error as a function of offset from the center for each tumor radius based on the results from the peak-based method. Average percent error for each case shown. Error bars represent the standard error of the mean (n=4).*

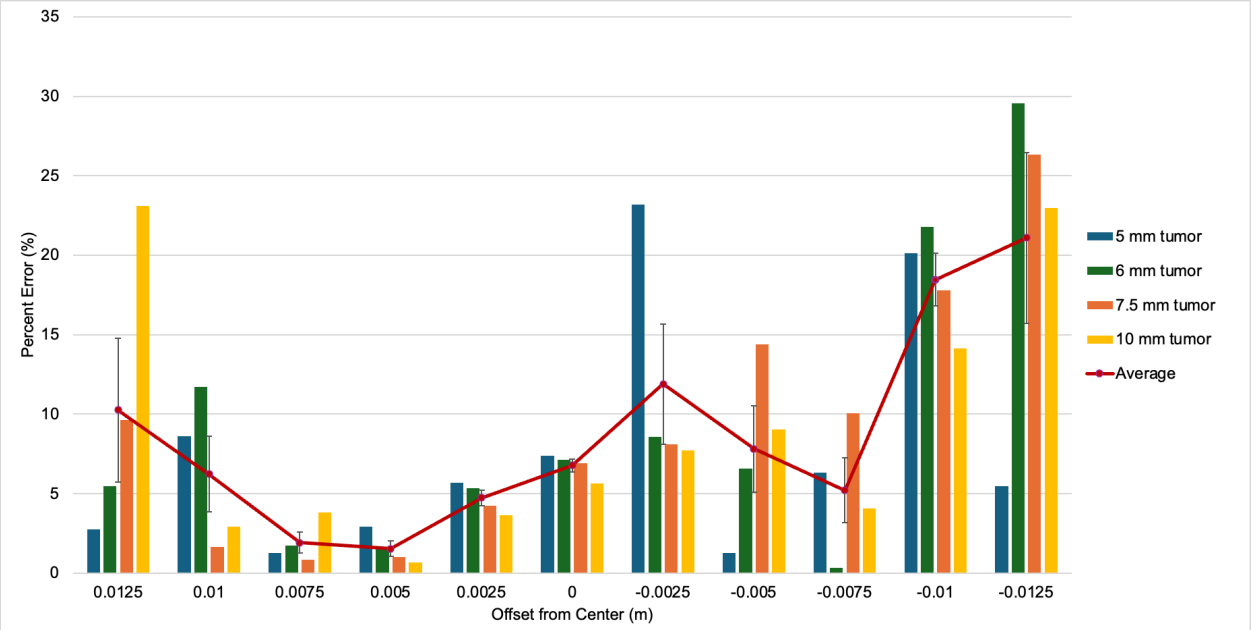

Figure H2. *Percent error as a function of offset from the center for each tumor radius based on the results from the dip-based method. Average percent error for each case shown. Error bars represent standard error of the mean (n=4).*

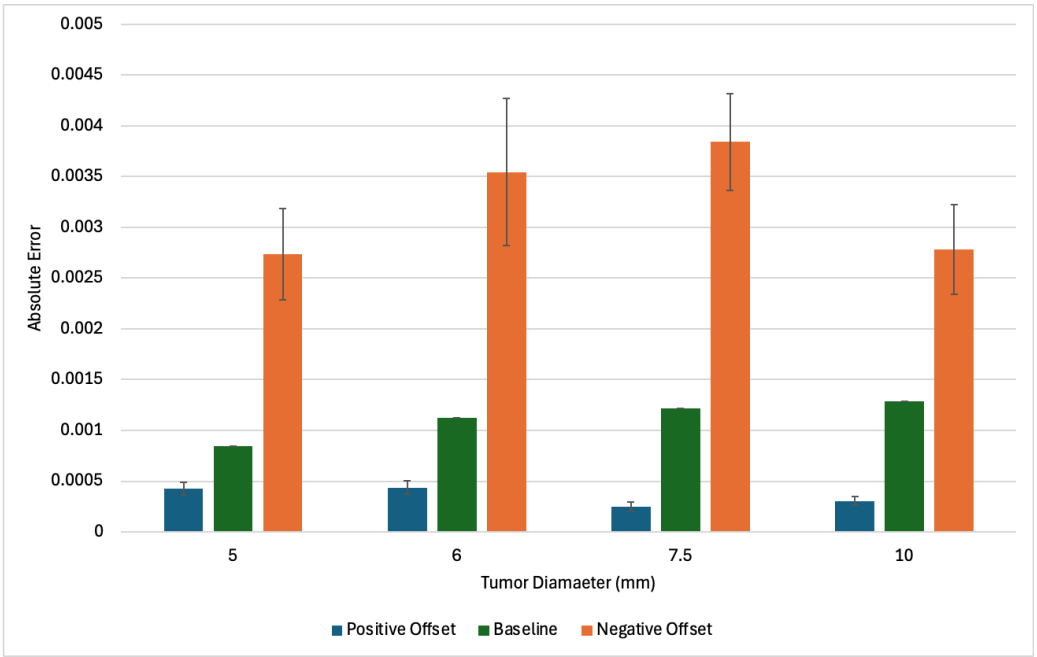

Figure H3. *Dip-based method absolute error averages for positive (blue), negative (orange), and no (green) offsets across tumor sizes. Error bars represent the standard error of the mean (n=5).*

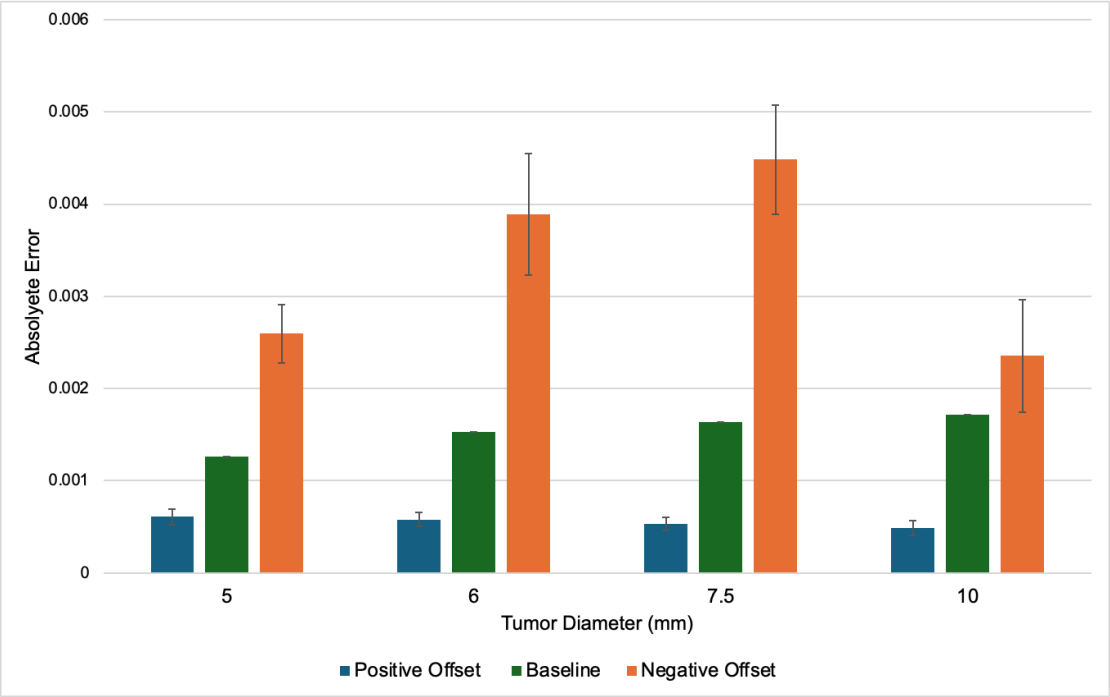

Figure H4. *Peak-based absolute error averages for positive (blue), negative (orange), and no (green) offsets across tumor sizes. Error bars represent the standard error of the mean (n=5).*